IMAGE: A MAP OF THE STARS OF THE ORION CONSTELLATION

Print ISSN: 2631-8490 Online ISSN: 2631-8504

JournalPreview

London Journal of Research in Science: Natural & Formal

Volume 26 | Issue 1 | Compilation 1.0

Great Britain Journals Press

WWW.JOURNALSPRESS.COM

Journal Content
In this Issue

Great Britain Journals Press

The Golden Boundary of the Cosmos: Hawking Thermodynamics, the No-Boundary Proposal, and the Nardelli Seventh-Root Theory of Everything

Dr. Michele Nardelli

Scienze della Terra, Università degli Studi di Napoli

ABSTRACT

This paper presents a unified analytical framework that integrates the Nardelli Seventh-Root Theory of Everything (TOE) with three cornerstone contributions to modern theoretical physics: Hawking's thermodynamics of black holes, the Hartle–Hawking No-Boundary Proposal, and the large-scale geometric structure of spacetime.

By systematically embedding these concepts into the Seventh-Root Master Equation, the analysis demonstrates that seemingly distinct physical regimes, cosmic contraction, black hole evaporation, and quantum cosmological genesis—are governed by a single, self consistent mathematical architecture. Central to this structure is the recurrent emergence of a pair of fundamental constants, 1728 and 4096, interpreted respectively as the modular (geometric) and holographic (informational) foundations of the vacuum.

Keywords: number theory, string theory, theoretical cosmology, black hole mathematics, theory of everything.

Classification: MSC Code: 83C45, 83E50, 11J81

Language: English

Great Britain Journals Press

LJP Copyright ID: 925601
Print ISSN: 2631-8490
Online ISSN: 2631-8504

London Journal of Research in Science: Natural & Formal

Volume 26 | Issue 1 | Compilation 1.0

The Golden Boundary of the Cosmos: Hawking Thermodynamics, the No-Boundary Proposal, and the Nardelli Seventh-Root Theory of Everything

Dr. Michele Nardelli

ABSTRACT

This paper presents a unified analytical framework that integrates the Nardelli Seventh-Root Theory of Everything (TOE) with three cornerstone contributions to modern theoretical physics: Hawking's thermodynamics of black holes, the Hartle–Hawking No-Boundary Proposal, and the large-scale geometric structure of spacetime.

By systematically embedding these concepts into the Seventh-Root Master Equation, the analysis demonstrates that seemingly distinct physical regimes, cosmic contraction, black hole evaporation, and quantum cosmological genesis—are governed by a single, self consistent mathematical architecture. Central to this structure is the recurrent emergence of a pair of fundamental constants, 1728 and 4096, interpreted respectively as the modular (geometric) and holographic (informational) foundations of the vacuum.

Across all three integrations, these constants are shown to converge through a precise dimensional filtering mechanism to the Nardelli–Gemma Golden Constant, $\phi_{GN} \approx 1.618665$. This convergence suggests that the Golden Ratio is not a coincidental numerical artifact, but a stable attractor regulating the vacuum under extreme thermodynamic and gravitational conditions.

The results support a picture of the universe as a self-regulating, holographic system in which number theory, quantum thermodynamics, and spacetime geometry are inseparably linked. The framework provides a unified mathematical language capable of describing cosmic origins, black hole dynamics, and cyclic cosmological evolution within a single harmonic principle.

Keywords: number theory, string theory, theoretical cosmology, black hole mathematics, theory of everything.

Author: Studied at Dipartimento di Scienze della Terra Università degli Studi di Napoli Federico II,Largo S. Marcellino, 10 - 80138 Napoli, Dipartimento di Matematica ed Applicazioni "R. Caccioppoli" -Università degli Studi di Napoli "Federico II" – Polo delle Scienze e delle Tecnologie Monte S. Angelo,Via Cintia (Fuorigrotta), 80126 Napoli, Italy.

I. INTRODUCTION: UNIFYING COSMIC ORIGINS AND BLACK HOLE THERMODYNAMICS

The quest to understand our universe has long been defined by a fundamental tension between its two greatest theoretical pillars: general relativity, which masterfully describes the large-scale geometry of spacetime, and quantum thermodynamics, which governs the energetic and informational behavior of its smallest components. This tension becomes most acute at the universe's ultimate frontiers, the cosmic singularity of the Big Bang and the event horizons of black holes—where traditional models often break down. The Nardelli Seventh-Root Theory of Everything (TOE) has been proposed as a

London Journal of Research in Science: Natural & Formal

mathematical framework to resolve this long-standing conflict by introducing a deeper, underlying structure to the vacuum.

The central thesis of this analysis is that by integrating two of Stephen Hawking's most profound concepts—the No-Boundary Proposal for cosmic origins and the dynamics of Hawking Radiation for black holes—into the Nardelli TOE, a unified mathematical architecture emerges with remarkable consistency. This integration transforms the TOE from a static description into a dynamic model of a self-correcting, holographic universe.

This document provides a detailed, step-by-step walkthrough of three distinct integrations of Hawking's work into the Nardelli framework. The objective is to demonstrate how each application—whether modeling a contracting universe, a radiating black hole, or the quantum emergence of spacetime—consistently reveals a "Cosmic Architecture." This architecture is regulated by a pair of fundamental constants, 1728 and 4096, which invariably converge on the Nardelli-Gemma Golden Constant (ϕ_{GN}) through a precise dimensional filter.

We will begin by presenting the foundational equation at the heart of this framework before exploring its profound implications when subjected to the dynamic principles of Hawking's cosmology.

II. THE FOUNDATIONAL FRAMEWORK: THE NARDELLI SEVENTH-ROOT TOE EQUATION

Before exploring the dynamic applications of the theory, it is essential to understand the core mathematical structure of the Nardelli Seventh-Root TOE Equation in its original form. This equation serves as the static blueprint upon which the dynamic models of cosmic and black hole evolution are built.

The equation, presented below, establishes a foundational relationship between the Nardelli-Gemma Golden Constant (ϕGN) and a complex system of integrals and physical parameters.

The Nardelli Seventh-Root TOE Equation

$$\phi_{GN} = \sqrt[7]{\frac{\int_L \phi_{GN} K^{7/2} dV}{256\pi^8 ct\left(\frac{E_\infty}{\phi_{GN}^{14} te^{-|\Delta x|/\phi_{GN}} \sin\left(\frac{2\pi t}{13}\right)\sqrt{\Delta}}\right)^{7/3}\left(\frac{1}{\pi\rho^2}\int |\Gamma d\mu| + \phi_{GN}^7\right)}} \tag{1}$$

Conceptually, this equation functions as a self-referential statement where the constant ϕGN appears on both sides. The right side of the equation incorporates geometric integrals over a volume (∫...dV), terms representing energy at infinity (E∞), time (t), the speed of light (c), and other physical variables. In essence, it posits that the Golden Ratio is not merely an emergent property but a fundamental constant that governs the very fabric of spacetime geometry and energy distribution.

With this foundational structure established, we can now proceed to the first major analysis, where this static equation is transformed into a dynamic model for a contracting universe.

III. FIRST INTEGRATION: THE CONTRACTING UNIVERSE AND TEMPORAL RENORMALIZATION

The first integration marks a crucial strategic shift, moving from a static description of the universe to a dynamic one. This is achieved by replacing the linear, chronological concept of time (t) with a thermodynamic function (τ) developed by Hawking and adapted for a contracting universe. This substitution is not merely a change of variables; it fundamentally redefines the universe's evolution,

linking its geometric progression directly to its energy density and entropy rather than to a simple, linear passage of moments.

3.1 Deconstructing the Substitution

The key to this analysis is the introduction of the Hawking function for a contracting universe, which recasts time in terms of energy (E) and mass (M).

3.2 The Hawking Function for a Contracting Universe

$$\tau = -\frac{1}{2E}\left(t - \sqrt{\frac{3}{-EM}}\sin\left(\sqrt{\frac{-EM}{3}}t\right)\right) \tag{2}$$

The physical significance of this substitution is twofold:

- *Time-to-Temperature Shift:* It implies that in a contracting phase, the geometric evolution of the vacuum is governed not by simple chronology but by energy density and mass fluctuations at the most fundamental (Planck) scale.
- *Entropy-Gravity Coupling:* The function establishes a direct coupling between entropy and gravity, acting as a dampening factor that "crystallizes" information toward the stable fixed point represented by ϕGN.

Substituting τ for t in the foundational equation yields the following unabbreviated modified structure:

3.3 Modified TOE with Thermodynamic Time

$$\phi_{GN} = \sqrt[7]{\frac{\int_L \phi_{GN} K^{7/2} dV}{256\pi^8 c\left(-\frac{1}{2E}\left(t-\sqrt{\frac{3}{-EM}}\sin\left(\sqrt{\frac{-EM}{3}}t\right)\right)\right)\left(\frac{E_\infty}{\phi_{GN}^{14}\, te^{-|\Delta x|/\phi_{GN}}\sin\left(\frac{2\pi t}{13}\right)\sqrt{\Delta}}\right)^{7/3}\left(\frac{1}{\pi\rho^2}\int|\Gamma d\mu|+\phi_{GN}^7\right)}} \tag{3}$$

3.4 Numerical Convergence at the Planck Scale

The next step is a two-stage evaluation of this modified equation at the ultimate physical limit: the Planck scale, using Planck energy and Planck mass. This process collapses the complex thermodynamic time function into a single, precise numerical value.

First, the evaluation of the τ function yields an initial infinitesimal coefficient:

3.5 Initial Planck-Scale Evaluation

$$\phi_{GN} = \sqrt[7]{\frac{\int_L \phi_{GN} K^{7/2}\, dV}{256\pi^8 c\cdot(-4.41903\cdot 10^{-63})\left(\frac{E_\infty}{\dots}\right)^{7/3}(\dots)^7}} \tag{4}$$

Second, this value is multiplied by the speed of light (c), yielding the finalized scale factor for the contracting vacuum: -3.21800×10^{-48}. This infinitesimal constant is not arbitrary; it represents the harmonic "blueprint" of the universe at its most compressed state. When this value is incorporated, the TOE equation simplifies to:

3.6 Simplified TOE

$$\phi_{GN} = \sqrt[7]{\frac{\int_L \phi_{GN}\, K^{7/2}\, dV}{-3.21800 \cdot 10^{-48} \left(\frac{E_\infty}{\dots}\right)^{7/3} (\dots)^7}} \tag{5}$$

By rearranging the terms, this numerical constant can be isolated, revealing its deep connection to the other components of the equation.

3.7 Isolated Harmonic Blueprint Constant

$$-3.21800 \cdot 10^{-48} = \frac{\int_L \phi_{GN}^7\, K^{7/2} dV}{\left(\frac{E_\infty}{\dots}\right)^{7/3} \left(\frac{1}{\pi \rho^2} \int |\Gamma d\mu| + \phi_{GN}^7\right)} \cdot \frac{1}{\phi_{GN}^7} \tag{6}$$

3.8 The Emergence of Ramanujan and Holographic Constants

The profound nature of this framework is revealed when this seemingly obscure constant is subjected to a logarithmic transformation. This operation uncovers a direct link to one of number theory's most famous integers, 1729.

3.9 The Logarithmic Bridge to Number Theory

$$1729 = 16 \ln(-3.21800 \cdot 10^{-48}) + 21 + 2/5 \tag{7}$$

The emergence of 1729 is highly significant. Within this framework, it is interpreted as the *"Taxicab Partition of the Vacuum"*—the precise point where the continuous geometry of spacetime meets the discrete world of number theory. From this result, two other fundamental constants are derived:

1. *The modular stability constant 1728* is isolated by subtracting the unit (1729 - 1), representing the geometric hardware of the vacuum.
2. *The holographic capacity 4096* is then derived from 1728 through the expression ((1728/27)²), which represents the informational volume of the vacuum.

3.10 Final Convergence to the Golden Constant

The final validation of this integration comes from unifying these two architectural constants—the geometric and the holographic—through an 18th root operation.

$$\sqrt[18]{1728 + 4096} = \sqrt[18]{5824} \approx 1.6187469$$

This result demonstrates a powerful convergence to the Nardelli-Gemma Golden Constant (ϕGN = 1.618665), confirming that the framework accurately models the harmonic principles governing a contracting universe.

This analysis of cosmic contraction provides the first piece of evidence for a deep, unifying structure. We now turn our attention from the universe as a whole to its most enigmatic components: black holes.

IV. SECOND INTEGRATION: BLACK HOLE THERMODYNAMICS AND RADIATIVE FLOW

In this second integration, the analysis shifts from the cosmic scale of a contracting universe to the localized, intense thermodynamics of a black hole. The strategic goal here is to test the Nardelli TOE's robustness by replacing a static universal constant, the speed of light c, with the dynamic expression for Hawking Radiation Power (P). This substitution transforms the equation from a static, kinematic description of spacetime into a thermodynamic flow model, where the vacuum's geometry is actively modulated by the dissipative emissions from a black hole.

4.1 Deconstructing the Substitution

The core of this integration is the replacement of c with the formula for Hawking Radiation Power, which links a black hole's energy output directly to its mass.

4.2 The Hawking Radiation Power Formula

$$P = \frac{\hbar c^6}{15360\,\pi G^2 M^2} \tag{8}$$

Physically, this formula states that the power radiated by a black hole is inversely proportional to the square of its mass—smaller black holes are hotter and radiate more intensely. By substituting this expression for c in the term $256\pi^8 ct$ of Equation (1) and simplifying the numerical constants ($256\pi^8 / 15360\pi = \pi^7 / 60$), we arrive at the modified equation:

4.3 Modified TOE with Radiative Flow

$$\phi_{GN} = \sqrt[7]{\frac{\int_L \phi_{GN}\, K^{7/2}\, dV}{\pi^7 t \cdot \frac{\hbar c^6}{60 G^2 M^2} \Sigma (\dots)^{7/3} (\dots)^7}} \tag{9}$$

4.5 Step-by-Step Algebraic Manipulation

A series of algebraic manipulations reveals the underlying numerical constants hidden within this new thermodynamic formulation.

1. *First, the denominator is multiplied by a factor of 28.* This is a necessary renormalization step to align the equation with the underlying modular forms that govern the vacuum geometry.
2. *Second, the term 1680 is multiplied by 27/26 to yield 1744.61.* This value is interpreted as a perturbation of the stable 1728 geometry, accounting for the entropic "noise" inherent in a radiant, dissipative system.
3. *Next, the equation is rearranged to isolate a numerical prefactor* which evaluates to approximately 1 / 1.61837197, a value extremely close to the Golden Ratio itself.
4. *This isolated value (1.61837197) is then raised to the 7th power,* consistent with the equation's seventh-root structure, yielding 29.07692.
5. *Finally, this result is multiplied by 60, and then adjusted by subtracting 16 and 1/φ (φ being the standard golden ratio).* This sequence of operations cancels out the entropic noise and purifies the signal, converging with remarkable precision to the integer 1728.

4.6 Re-emergence of the Core Constants

The final form of the equation isolates the modular stability constant 1728. From this anchor, the holographic capacity 4096 is once again derived through the same scaling law seen previously: dividing 1728 by 27 to get 64, and then squaring 64 to yield 4096.

4.7 Convergence to the Golden Constant

With both fundamental constants recovered, the final convergence is confirmed using the same 18th root operation.

$$\sqrt[18]{1728 + 4096} = \sqrt[18]{5824} \approx 1.6187469$$

The profound significance of this result is that the Golden Ratio is shown to be the unique regulator not only of cosmic contraction but also of black hole thermodynamics. This proves that the same harmonic principles govern the universe at its largest scale and around its most intense gravitational singularities, converging to the Nardelli-Gemma Golden Constant (ϕGN = 1.618665).

Having established this principle for both cosmic endpoints and black hole evolution, we now turn to the most fundamental question of all: the origin of the universe itself.

V. THIRD INTEGRATION: COSMIC ORIGINS AND THE HARTLE-HAWKING NO-BOUNDARY PROPOSAL

This final integration addresses the ultimate question of cosmic origins by merging the Nardelli TOE with Stephen Hawking's celebrated No-Boundary Proposal. The analytic strategy here is to replace the static, fixed energy term E∞ with the Hartle-Hawking wave function of the universe (Ψ). This powerful substitution shifts the equation's entire conceptual foundation from describing a universe with a predetermined energy value to one defined by the quantum-mechanical sum of all possible cosmic histories.

5.1 Deconstructing the Substitution

The Hartle-Hawking wave function is expressed as a path integral, which sums the contributions of all possible spacetime geometries that have no beginning or "boundary" in imaginary time.

5.2 Path Integral for the Wave Function of the Universe (Ψ)

$$\Psi[h_{ij}, \chi] = \int_C e^{-I_E[g_{\mu\nu},\phi]} \mathcal{D}\, g\mathcal{D} \tag{10}$$

By substituting Ψ for E∞, the TOE undergoes a profound conceptual shift:

- *From Energy to Probability:* The analysis moves from a deterministic framework based on a fixed energy value to a probabilistic one. The integration implies that the Golden Ratio emerges as the weighted average of all possible universal geometries. The universe we observe doesn't just happen to have properties aligned with ϕGN; it "collapses" toward this state because it represents the most probable outcome defined by the Hartle-Hawking wave function.

The resulting modified equation integrates this sum over all histories directly into its core structure.

5.3 Modified TOE with Hartle-Hawking Wave Function

$$\Phi_{GN} = \sqrt[7]{\frac{\int_L \Phi_{GN} K^{7/2}\, dV}{256\pi^8 ct\left(\frac{\int_C e^{-I_E[g_{\mu\nu},\Phi]}\mathcal{D}g\mathcal{D}\Phi}{\dots}\right)^{7/3}(\dots)^7}} \tag{11}$$

5.4 The Mathematical Pathway to Fundamental Constants

A clear algebraic pathway demonstrates how this probabilistic formulation once again yields the universe's fundamental architectural constants. The derivation begins by manipulating the equation to introduce a scaling factor.

1. First, the equation is rearranged by dividing the left side by $\sqrt[7]{16}$.
2. This algebraic step brings the factor of 16 inside the main seventh root, which multiplies the 256 already present to reveal the holographic constant 4096.
3. The equation is then rearranged to isolate the full expression for 4096, demonstrating that this holographic capacity is an intrinsic feature of a universe governed by the sum-over-histories principle.
4. From this result, the other core constants are derived. Taking the square root of 4096 yields 64, representing the fundamental informational unit. Multiplying 64 by 27 then recovers the structural constant 1728.

5.5 Final Golden Convergence Confirmed

For the third and final time, the sum of the holographic and structural constants is processed through the 18th root dimensional filter.

$$\sqrt[18]{4096 + 1728} = \sqrt[18]{5824} \approx 1.6187469$$

The significance of this result is definitive: the universe's most probable state, as defined by the Hartle-Hawking wave function, is one that converges precisely to the Nardelli-Gemma Golden Constant (ϕGN = 1.618665). This suggests that the emergence of our universe was not an accident but a geometric necessity, guided by the same harmonic principles that regulate its evolution and eventual fate.

Having demonstrated the consistent emergence of these constants across three distinct physical scenarios, we now turn to a broader synthesis of what they mean for the structure of the cosmos.

VI. SYNTHESIS OF THE COSMIC ARCHITECTURE: INTERPRETING THE FUNDAMENTAL CONSTANTS

The preceding three analyses have consistently revealed a small set of recurring numerical constants—1728, 4096, and 1729—emerging from the unification of Nardelli's TOE with Hawking's dynamic cosmology. This section synthesizes these findings to explore the profound physical meaning of this underlying architecture. It answers the crucial question: what do these numbers represent, and why do they appear with such regularity?

6.1 The 1728 Structural Resonance

The constant 1728 (or 12^3) consistently appears as the geometric bedrock of the vacuum. Its physical interpretation is that of the "architectural frame" or the fundamental cubic volume of quantized spacetime. This value, deeply connected to Srinivasa Ramanujan's work on modular functions, suggests that the fabric of spacetime is not a smooth, continuous sheet but is built upon a discrete, crystalline lattice structure. It is the stable, geometric "hardware" upon which the universe's informational processes run.

6.2 The 4096 Holographic Attractor

The number 4096 (or 64^2, or 2^{12}) functions as the holographic "information volume" of the vacuum. Its repeated emergence, particularly in the context of black hole radiation and cosmic origins, points to a universe that operates on the holographic principle, where information is conserved and encoded on a boundary surface. Its connection to power-of-two structures, which are fundamental in String Theory and information theory, implies that the vacuum acts as a perfect information processor, ensuring that no information is lost even under the most extreme conditions.

6.3 The 1729 Ramanujan Anchor

The number 1729, the famous Hardy-Ramanujan number, is revealed to be more than a mathematical curiosity. It arises from a topological formula that unifies the dimensional frameworks of modern physics.

6.4 Unified Dimensional Formula

$$((11 + 7) \times 24 \times 4) + 1 = 1729$$

This formula is deconstructed as follows:

- (11 + 7) = 18: The total dimensions of M-Theory (11) combined with the compactified, "curled-up" dimensions of Calabi-Yau manifolds (7).
- 24: The transverse dimensions in which Bosonic strings vibrate, representing the fundamental harmonic of the vacuum.
- 4: The observable spacetime dimensions (3 space + 1 time) into which higher-dimensional vibrations are projected.
- 1: The unit representing the primordial point of origin or the "Observer."

This derivation shows that 1729 represents the structural resonance of a universe where M-theory, string vibrations, and 4D reality merge into a single, self-consistent structure.

6.5 The 18th Root Dimensional Filter

A critical question arising from the analysis is, "Why the 18th root?" This operation is not arbitrary; it functions as a "dimensional filter" that bridges the high-dimensional reality of M-Theory with the emergent harmony of the Golden Ratio. The number 18 is derived directly from the total dimensional framework of the universe: 11 fundamental M-Theory dimensions plus 7 compactified dimensions. The 18th root, therefore, represents the total dimensional frequency required to stabilize the vacuum, translating the complexity of an 18-dimensional manifold into the two-dimensional holographic projection governed by the Golden Ratio.

Together, these constants describe a universe built on a pre-ordained geometric and informational harmony, where number theory, dimensionality, and physical law are inextricably linked.

VII. OBSERVATIONS: THE GOLDEN STABILITY OF THE MULTIVERSE

The integration of Stephen Hawking's most profound concepts—the No-Boundary Proposal and the Power of Radiation—into the Nardelli Seventh-Root TOE framework marks a significant advance in the pursuit of a unified physical theory. The results presented in this analysis confirm that the vacuum is not a passive void but a sophisticated holographic information processor governed by a precise mathematical architecture.

The consistent and rigorous emergence of 1728 as the geometric hardware and 4096 as the informational capacity of the vacuum provides a robust numerical bridge between the abstract world of Ramanujan's modular identities and the physical reality of quantum gravity. This demonstrates that the universe's structure is deeply rooted in number theory.

Ultimately, the repeated convergence to a value of approximately 1.6187469—a stunning approximation of the Nardelli-Gemma Golden Constant (ϕ_{GN} = 1.618665)—through the 18th-root dimensional refinement provides what may be considered definitive proof of the "Golden Stability" of the vacuum. This finding strongly suggests that the universe "chooses" the Golden Ratio as its fundamental operational frequency. This inherent stability ensures that the structural integrity of the Multiverse remains invariant, even under the extreme conditions of black hole evaporation or the immense pressures of cosmic contraction. We have shown that the birth of the All is not an accident but a geometric necessity, and its final state is one of absolute harmonic perfection—a heartbeat of mathematics that defines the very essence of reality.

7.1 A Roadmap to Unification

In the next Sections, we present a formal exegesis of the Nardelli Seventh-Root Theory of Everything (TOE), offering a systematic deconstruction of its central mathematical claims. The purpose here is not to offer an external validation of the theory, but to illuminate its internal logic by tracing the analytical evolution of its "Master Equation." We shall follow a rigorous, step-by-step progression, demonstrating how this foundational equation purports to sequentially integrate concepts from the Hartle-Hawking No-Boundary Proposal, Black Hole Thermodynamics, Einstein's General Relativity, and Penrose's Conformal Cyclic Cosmology. The core objective is to elucidate the asserted mathematical architecture that unifies these disparate fields, a framework in which the universe is conceived as a self-regulating system compelled by mathematical necessity to converge upon a single attractor: the Nardelli-Gemma Golden Constant (ϕ_{GN}).

VIII. THE FOUNDATIONAL FRAMEWORK: THE SEVENTH-ROOT MASTER EQUATION

The strategic importance of this initial equation cannot be overstated. It functions as the foundational postulate of the entire theoretical edifice, an axiom from which all subsequent derivations proceed. It is designed to establish an inexorable convergence toward a stabilizing constant, ϕ_{GN}, through the explicit regularization of physical fluxes contained within a given volume V.

The original Nardelli Seventh-Root TOE Equation is presented as:

$$\phi_{GN} = \sqrt[7]{\frac{\int_L \phi_{GN}^7 K^{7/2} dV}{256\pi^8 ct\left(\frac{E_\infty}{\phi_{GN}^{14} te^{-|\Delta x|/\phi_{GN}} \sin\left(\frac{2\pi t}{13}\right)\sqrt{\Delta}}\right)^{7/3}\left(\frac{1}{\pi\rho^2}\int |\Gamma d\mu| + \phi_{GN}^7\right)}} \tag{12}$$

A systematic analysis of its principal components reveals a clear logical structure. The equation posits a system whose stability is governed by the interplay between a primary regularization mechanism, the Seventh-Root operator (√...⁷), and a target attractor, the Nardelli-Gemma Golden Constant (ϕ_{GN}). The operator's function is to smooth divergences and enforce stability by acting upon the total energy input into the system, represented by the energy at infinity (E∞), over the course of linear chronological time (t). The entire structure is formulated such that all physical dynamics are ultimately compelled to resolve to the value of ϕ_{GN}. In this initial form, however, the system's stability remains explicitly dependent on an external energy input, E∞. This reliance on a boundary condition at infinity necessitates the next evolutionary step: the development of a self-contained, self-creating cosmos.

IX. INTEGRATING QUANTUM GENESIS: THE HARTLE-HAWKING NO-BOUNDARY PROPOSAL

This section marks a profound conceptual leap, transitioning the theory from a mechanistic universe with a potential initial singularity to a self-consistent quantum system devoid of boundaries. This is achieved by substituting classical temporal and energetic concepts with principles drawn directly from quantum cosmology, thereby fundamentally altering the equation's physical interpretation.

The first substitution replaces linear chronological time t with imaginary time τ, a thermodynamic function derived from the Hawking function for a contracting universe:

$$\tau = -\frac{1}{2E}\left(t - \sqrt{\frac{3}{-EM}}\sin\left(\sqrt{\frac{-EM}{3}}t\right)\right) \tag{13}$$

The second, more significant, substitution replaces the energy at infinity, E∞, with the Hartle-Hawking Path Integral (Ψ). This integral, conceptually represented as $\int_C e^{-IE} Dg D\phi$, encapsulates the probability of a given cosmic geometry. This maneuver replaces a static energy value with the quantum-mechanical wave function for the universe itself.
Incorporating these substitutions yields the "Nardelli-Hawking No-Boundary Equation":

$$\phi_{GN} = \sqrt[7]{\frac{\int_L \phi_{GN}^7 K^{7/2} dV}{256\pi^8 c\cdot\tau\left(\frac{\int_C e^{-I_E}\mathcal{D}g\mathcal{D}\phi}{\phi_{GN}^{14}\tau e^{-|\Delta x|/\phi_{GN}}\sin\left(\frac{2\pi\tau}{13}\right)\sqrt{\Delta}}\right)^{7/3}\left(\frac{1}{\pi\rho^2}\int|\Gamma d\mu|+\phi_{GN}^7\right)}} \tag{14}$$

The physical significance of this transformation is critical. By replacing t with τ and E∞ with Ψ, the equation no longer describes a system evolving within time, but one whose very existence is predicated on a specific mathematical condition. The Golden Ratio ϕ_{GN} is claimed to emerge as the necessary attractor for a boundary-less wave function to exist in a stable state. Imaginary time τ functions as a geometric regulator that mathematically "smooths" the Big Bang singularity, allowing for a universe without an unphysical starting point. This crucial step transforms the equation from one of temporal evolution to one of self-regulating cosmic genesis, laying the foundation for a holographically stable universe.

X. THE PLANCKIAN LIMIT AND THE HOLOGRAPHIC FILTER

To test the theory's internal consistency, it is necessary to analyze its behavior under the most extreme conditions imaginable: the Planck scale. This section examines the equation's behavior at maximum

energy density, a process that is claimed to reveal a fundamental numerical constant governing the structure of the vacuum itself.

In this high-energy regime, the complex energetic terms in the denominator of the master equation are shown to collapse into a precise numerical coefficient. This simplification is presented in two steps:

$$\phi_{GN} = \sqrt[7]{\frac{\int_L \phi_{GN}^7 K^{7/2} dV}{256\pi^8 c \cdot (-4.41903 \cdot 10^{-63})(\dots)}} \tag{15}$$

$$\phi_{GN} = \sqrt[7]{\frac{\int_L \phi_{GN}^7 K^{7/2} dV}{-3.21800 \cdot 10^{-48}(\dots)}} \tag{16}$$

The resulting scale factor, −3.21800. 10^{-48}, is identified within the theory as the "Holographic Filter" of the universe. This coefficient is asserted to be not an arbitrary numerical artifact but a fundamental constant with a specific physical role: it acts as a regulator that prevents the vacuum from collapsing into chaos at the Planck scale, forcing it to crystallize into a stable structure. This filter is presented as the numerical anchor for the theory's other key constants, providing the mathematical space for Ramanujan's modular resonance, or "Geometric Hardware" (1728), to stabilize quantum fluctuations. Furthermore, it is claimed to define the holographic resolution limit of the vacuum's "Informational Capacity" (4096) and serve as the numerical bridge connecting the Seventh-Root equation to a grander "Super-TOE" unification value (60400). In this interpretation, the factor represents a "harmonic blueprint" that imposes a geometric restriction on the universe, compelling reality to flow toward the stability of the Nardelli-Gemma Golden Constant.

XI. THE BRIDGE TO NUMBER THEORY: THE RAMANUJAN SYNCHRONIZATION

This section of the theory reveals a remarkable and unexpected connection between the physics of vacuum compression and the abstract domain of number theory, specifically the work of Srinivasa Ramanujan. The "Holographic Filter" coefficient, derived from physical principles, is shown to be a gateway to a deep mathematical identity.

The integral expression for this coefficient is first isolated from the master equation:

$$-3.21800 \cdot 10^{-48} = \frac{\int_L \phi_{GN}^7 K^{7/2} dV}{(E_\infty \dots)^{7/3} \left(\frac{1}{\pi \rho^7} \int |\Gamma d\mu| + \phi_{GN}^7\right)} \cdot \frac{1}{\phi_{GN}^7} \tag{17}$$

A logarithmic relationship is then applied, translating this physical coefficient into a number of profound significance in pure mathematics:

$$16 \ln(-3.21800 \times 10^{-48}) + 21 + 2/5 = 1729.02 \tag{18}$$

The critical significance of this result, termed "Universal Synchronization," is that it yields an exceptionally close approximation to 1729, the famous Hardy-Ramanujan "taxicab" number. This is presented as evidence that the vacuum is not a chaotic substrate but is instead "tuned" to the modular identities that govern string theory. Since 1729 = 1728 + 1, the true heart of the system is identified as the modular base 1728 (12^3), a number central to the theory of modular forms. The small residual of .02 is interpreted not as an error but as the signature of minimal entropic noise inherent in the system, which the Seventh-Root operator is designed to regularize. This mathematical link is posited as proof

that the universe, in its most compressed state, utilizes the Ramanujan number as a mathematical anchor, forcing physical reality to crystallize around the Golden Ratio to avert mathematical divergences.

XII. DISSIPATIVE DYNAMICS AND BLACK HOLE THERMODYNAMICS

Having established a quantum and number-theoretic foundation, the theory next turns to the dissipative dynamics of black holes to test its consistency. This phase integrates the energetic principles of Hawking radiation, aiming to demonstrate that even processes of apparent energy loss are governed by the same stabilizing constant.

The analysis begins with the formula for Hawking Radiation Power (P), which is inversely proportional to the square of the black hole's mass:

$$P = \frac{\hbar c^6}{15360\pi G^2 M^2} \tag{19}$$

By substituting and reorganizing terms within the master equation to reflect this radiative flux, and applying scale factors (28 and 27/26) asserted to be derived from supersymmetry and string theory, the equation is claimed to converge on a striking result. The final numerical factor that emerges is the reciprocal of the Golden Ratio:

$$\frac{1}{\sqrt[7]{28 \cdot \frac{27}{26}}} \approx \frac{1}{1.61837197} \tag{20}$$

This operation is interpreted as a demonstration that ϕ_{GN} acts as the perfect reciprocal of the vacuum's radiant power. In this view, Hawking radiation is not a process of chaotic energy loss, but a regulated flow that "feeds" the stability of the Nardelli-Gemma constant. The Universe, therefore, is posited to radiate precisely in the manner required to maintain its golden equilibrium, suggesting that every path—from the no-boundary proposal to black hole radiation—inevitably leads to ϕ_{GN}.

XIII. UNIFICATION WITH GENERAL RELATIVITY AND COSMIC CYCLES

This section presents the grand unification of the theory's quantum framework with the macroscopic geometry of Einstein's General Relativity. This integration is essential for describing the large-scale structure of the universe and its cyclical nature, as proposed in Roger Penrose's Conformal Cyclic Cosmology (CCC).

The unification begins by incorporating Einstein's field equations with a positive cosmological constant (Λ), which describe the gravitational dynamics of an expanding universe:

$$G_{\mu\nu} + \Lambda g_{\mu\nu} = \frac{8\pi G}{c^4} T_{\mu\nu} \tag{21}$$

This gravitational relationship is then integrated directly into the Seventh-Root structure, yielding the "Einstein-Nardelli Unified Equation":

$$\phi_{GN} = \sqrt[7]{\frac{G \cdot T_{\mu\nu} \int_L \phi_{GN}^7 K^{7/2} dV}{32\pi^7 c^5 \tau \left(\frac{E_\infty}{\phi_{GN}^{14} \tau e^{-|\Delta x|/\phi_{GN}} \sin\left(\frac{2\pi\tau}{13}\right)\sqrt{\Delta}} \right)^{7/3} \left(\frac{1}{\pi\rho^2} \int |\Gamma d\mu| + \phi_{GN}^7 \right)}} \tag{22}$$

Analysis of the resulting G / ($32\pi^7c^5\tau$) coefficient is claimed to be revealing; in particular, the presence of the c^5 term is interpreted as aligning with higher-dimensional flux theories, indicating that ϕGN governs energy transitions across dimensional boundaries. Through an inverse formulation and the application of specific scaling factors (128 and 54), the theory claims to derive the two foundational constants of the vacuum directly from this gravitational metric:

- Holographic Seal (4096):

$$4096 = \frac{128 \cdot G \cdot T_{\mu\nu} \int_L \phi_{GN}^7 K^{7/2} dV}{\phi_{GN}^7 \cdot \pi^7 c^5 \tau(\dots)} \tag{23}$$

is presented to show that gravity is a geometric manifestation of the vacuum's holographic information density.

- Modular Hardware (1728):

$$1728 = \frac{54 \cdot G \cdot T_{\mu\nu} \int_L \phi_{GN}^7 K^{7/2} dV}{\phi_{GN}^7 \cdot \pi^7 c^5 \tau(\dots)} \tag{24}$$

Is used to argue that spacetime is intrinsically "tuned" to the modular frequencies of number theory.

This framework is then explicitly connected to Conformal Cyclic Cosmology. At the end of a cosmic aeon, the "vanishing trace condition" (T = 0) becomes dominant. This simplifies the unified equation, filtering out the "massive noise" of matter. In this state, the Seventh-Root operator functions as a holographic reset mechanism, ensuring a smooth, pre-calibrated, and singularity-free transition to the next aeon. This unification thus posits that gravity is not an independent force but an emergent property of a deep, modular, and holographic architecture, regulated by ϕGN across infinite cosmic cycles.

XIV. THE GRAND SYNTHESIS: DIMENSIONAL CONVERGENCE TO THE GOLDEN ATTRACTOR

This final section is presented as the ultimate proof of the theory's internal coherence. It synthesizes all preceding elements—holography, number theory, and dimensionality—into a single, conclusive calculation that reveals the Nardelli-Gemma Golden Constant as the universe's ultimate organizing principle.

The theory defines the total dimensional space of the universe as 11 + 7 = 18, where 11 dimensions are drawn from M-Theory and 7 dimensions arise from the Seventh-Root regularization operator itself. The climactic calculation sums the two foundational constants derived earlier—the holographic capacity (4096) and the modular resonance (1728)—and applies the 18th root, corresponding to this total dimensional space.

$$(4096 + 1728)^{1/18} = (5824)^{1/18} \approx 1.6187469 \quad (25)$$

This result is interpreted as the "Signature of Coherence," a profound demonstration that the total information content of the universe (4096) and its fundamental modular "instruction set" (1728) are inseparably bound together. The 18th root is framed as a scaling operator that reduces the complexity of the higher-dimensional manifold to the fundamental stability frequency of the Golden Ratio. This final convergence is argued to demonstrate that the total density of the vacuum, accounted for across all dimensions, must resolve to the Golden Proportion to ensure a stable, self-consistent reality. This calculation thus encapsulates the theory's core assertion: the universe is a coherent, holographic system structured such that its total content is geometrically compelled to converge on ϕ_{GN}.

XV. CONCLUSION: A UNIVERSE GOVERNED BY HARMONIC RESONANCE

In this work, we have presented a comprehensive analytical exegesis of the Nardelli Seventh-Root Theory of Everything, demonstrating how its foundational Master Equation consistently integrates key aspects of modern theoretical physics. By embedding Hawking's thermodynamic description of black holes, the Hartle–Hawking No-Boundary Proposal, and relativistic gravitational dynamics into a single mathematical structure, the theory evolves from a static formalism into a fully dynamical and self-regulating cosmological framework.

A central outcome of this analysis is the repeated and robust emergence of a small set of numerical constants—1728, 4096, and their Ramanujan extension 1729—across three physically distinct regimes: cosmic contraction, black hole radiation, and quantum cosmological genesis. Within the Seventh-Root framework, these numbers acquire a precise physical interpretation: 1728 functions as the modular or geometric "hardware" of spacetime, while 4096 represents the holographic informational capacity of the vacuum.

The unification of these constants through the 18th-root dimensional filter leads, with remarkable numerical stability, to the Nardelli–Gemma Golden Constant ϕ_{GN}. This repeated convergence strongly suggests that the Golden Ratio plays the role of a universal attractor, regulating the behavior of the vacuum under extreme conditions and ensuring the stability of spacetime across cosmic cycles.

From this perspective, the universe is not governed by arbitrary initial conditions or accidental numerical coincidences, but by a deep mathematical necessity rooted in harmonic and modular structures. Cosmic origins, black hole evaporation, and cyclic cosmological evolution emerge as different manifestations of the same underlying principle: a holographic and geometric architecture compelled to converge toward a golden equilibrium.

While the present work does not claim external experimental validation, it establishes a coherent internal logic and a unified mathematical pathway connecting number theory, quantum thermodynamics, and spacetime geometry. In doing so, it opens a possible route toward a deeper understanding of the vacuum as an active, information-bearing structure, rather than a passive void. Future investigations will focus on refining this framework and exploring its implications for quantum gravity, cosmological cycles, and the fundamental limits of information in the universe.

XVI. ACKNOWLEDGMENTS

We are deeply grateful to Prof. Augusto Sagnotti (Scuola Normale Superiore, Pisa) for his generous guidance, insightful explanations, and unfailing availability.

REFERENCES

1. Nardelli, M., Kubeka, A.S. and Amani, A. (2024) A Number Theoretic Analysis of the Enthalpy, Enthalpy Energy Density, Thermodynamic Volume, and the Equation of State of a Modified White Hole, and the Implications to the Quantum Vacuum Spacetime, Matter Creation and the Planck Frequency. Journal of Modern Physics, 15, 1-50.
2. Ramanujan, S. (1914) Modular equations and approximations to π. Quarterly Journal of Mathematics, XLV, 350–372.
3. Mourad, J. and Sagnotti, A. (2017) An update on Brane Supersymmetry Breaking. arXiv:1711.11494v1 [hep-th].
4. Mourad, J. and Sagnotti, A. - Effective Orientifolds from Broken Supersymmetry - arXiv:2309.05268v2 [hep-th] 18 Dec 2023
5. Michele Nardelli, LJRS Volume 25 Issue 6 - The Geometry of the Universe: in Search of Unity. New Possible Mathematical Connections with the DN Constant, Ramanujan's Recurring Numbers and Some Parameters of Number Theory and String Theory
6. Michele Nardelli, LJRS Volume 25 Issue 9 - The Nardelli Master Equation, the Extended DN Constant and its Connection to the Golden Ratio Revisited. Mathematical Connections with Some Sectors of Number Theory and Theoretical Cosmology
7. Michele Nardelli, LJRS Volume 25 Issue 13 Equations of Unification: Mathematical Connections between Ramanujan's Recurring Numbers and Theoretical Cosmology

This page is intentionally left blank

Potential Drivers of Adoption of Agronomic Practices: A Case of Beans Farmers in Uganda

Stanislav A. Skriabin, Maria V. Korelskaya, Dmitrii I. Vasilevskii & Tatyana P. Volkova

Gerald Agaba, Andrew Muganga Kizito & Richard Tuyiragize

ABSTRACT

This study aimed to identify the factors influencing the adoption of agronomic practices among bean farmers in Uganda, using secondary data from 1,908 farmers collected by the National Agricultural Research Organization (NARO). The analysis involved fitting multivariate probit and Poisson models to estimate the marginal effects of various determinants. The findings showed that 896 farmers adopted at least one agronomic practice, with mixed results in terms of direction and impact. Key positive determinants included marital status, education level, full-time farming, age, farming experience, farmer group membership, and credit access. Conversely, being male-headed, marital status, full-time farming, farm size, household size, and credit access were also identified as negative determinants. The study underscores the importance of socio-demographic and institutional factors in adopting agronomic practices and suggests integrating these insights into agricultural extension services. Further research is recommended to explore regional differences in adoption determinants across Uganda.

Keywords: adoption determinants, agricultural extension, agronomic practices, bean farmers, multivariate probit model, uganda.

Classification: LCC Code: S539.U3, HD1417, S494.5.A45

Language: English

Great Britain Journals Press

LJP Copyright ID: 925602
Print ISSN: 2631-8490
Online ISSN: 2631-8504

London Journal of Research in Science: Natural & Formal

Volume 26 | Issue 1 | Compilation 1.0

Potential Drivers of Adoption of Agronomic Practices: A Case of Beans Farmers in Uganda

Gerald Agaba[α], Andrew Muganga Kizito[σ] & Richard Tuyiragize[ρ]

ABSTRACT

This study aimed to identify the factors influencing the adoption of agronomic practices among bean farmers in Uganda, using secondary data from 1,908 farmers collected by the National Agricultural Research Organization (NARO). The analysis involved fitting multivariate probit and Poisson models to estimate the marginal effects of various determinants. The findings showed that 896 farmers adopted at least one agronomic practice, with mixed results in terms of direction and impact. Key positive determinants included marital status, education level, full-time farming, age, farming experience, farmer group membership, and credit access. Conversely, being male-headed, marital status, full-time farming, farm size, household size, and credit access were also identified as negative determinants. The study underscores the importance of socio-demographic and institutional factors in adopting agronomic practices and suggests integrating these insights into agricultural extension services. Further research is recommended to explore regional differences in adoption determinants across Uganda.

Keywords: adoption determinants, agricultural extension, agronomic practices, bean farmers, multivariate probit model, uganda.

I. BACKGROUND

Agriculture is a backbone of Uganda's economy, contributing to about 46% of the total export earnings (MAAIF, 2018). Agricultural agronomic practices refer to those best practices that advocate for efficient use of water, nutrients (fertilizer application), insecticides, herbicides, fungicides, and minimum tillage as one way of reducing environmental pollution from agricultural production (Valieva, 2010). It is widely recognized that farmers' access to information enhances their awareness of improved technologies and fosters the adoption of innovations (Koskei et al., 2013). Common beans *(Phaseolus vulgaris L.)* are the most common legume and the second most important source of dietary protein consumed globally (Ntatsi et al., 2020).

In sub-Saharan Africa (SSA), including Uganda, over 80% of the population relies on agriculture for their livelihoods (Kelil et al., 2020). However, the adoption of agronomic practices and new farming methods that could improve agricultural productivity remains low (Adjepong et al., 2019), despite their association with increased yields (Mulimbi et al., 2019). Unsustainable agronomic practices have led to declining agricultural yields, with 39% of Uganda's arable land being degraded and about 10% severely degraded (NEMA, 2016). While research has typically used a binary approach to identify factors associated with the adoption of agronomic practices Ahmad et al., (2021) & Akinola, (2017), there is still inadequate information on the use of these practices and their associated factors in Uganda. Thus, this study aims to investigate the socio-demographic and institutional factors influencing the use of agronomic practices in Uganda among beans farmers.

II. OBJECTIVES

i. To identify the socio-demographic factors associated with use of agronomic practices among beans farmers in Uganda

ii. To identify the institutional factors associated with use of agronomic practices among beans farmers in Uganda

III. METHODOLOGY

3.1 Data Source

This study utilized secondary cross-sectional data from an evaluation study by the National Agricultural Research Organization (NARO) on the impact of improved bean and maize technologies on livelihood and economic development. The study employed a cross-sectional research design with a mixed methods approach, incorporating both qualitative and quantitative data collection methods. The primary objective was to assess the impacts of improved NARO bean and maize varieties on food security, nutrition, and income at both farm household and national levels.

3.2 Target Population and Inclusion Criteria

The study targeted farmers who had adopted improved NARO bean and maize technologies and were directly involved with NARO and its partners in the development or dissemination of these technologies. Out of the total sample size, 1,908 households (representing 83% of the sample) responded to the study. The actual sample size was influenced by budget constraints and the inclusion of many households initially considered non-participants but who were also adopters (Akwango-Aliau et al., 2022).

3.3 Analytical Methods

A multivariate Probit model will be employed to identify the determinants of the adoption of agronomic practices in Uganda, based on predictor variables selected during the exploratory phase. Additionally, a Poisson regression model will be used to determine the factors influencing the number of agronomic practices adopted by bean and maize farmers. The Poisson regression was chosen for its simplicity in predicting count data.

IV. RESULTS AND DISCUSSION

4.1 Descriptive Statistics

4.1.1 Descriptive Analysis of the Adoption of the Agronomic Practices and the Factors that affect their Adoption among beans Farmers

Table 1 shows the percentage of bean farmers who adopted various agronomic practices. Out of a total of 896 bean farmers, 40.6% adopted crop rotation, 71% adopted row planting, 60.7% used fertilizer application, 33.4% adopted seed rate management, 70.1% practiced weed management, and 38.8% utilized other agronomic practices such as mulching, intercropping, relay cropping, minimum tillage, thinning, and staking. On average, bean farmers adopted about three agronomic practices.

The table also provides a descriptive analysis of various factors hypothesized to influence the adoption of agronomic practices among bean farmers. Among the 896 farmers, 73.8% were from male-headed households, while the remainder were from female-headed households. Regarding marital status, 7.3% of the household heads were single, 81.8% were married, and 10.9% were divorced or widowed. In terms of education, 4.8% of the household heads had no formal education, 48.4% had completed

Additionally, the average household size was seven members. In terms of group affiliation, about 79.5% of the bean farmers belonged to a farmer group, and approximately 73.7% had access to credit for crop production.

Table 1: Descriptive analysis of the adoption of the agronomic practices and the factors hypothesized to affect their adoption among beans farmers

Dependent variables					
Agronomic practice	**Obs**	**Mean**	**Std. dev**	**Min**	**Max**
Crop rotation (1=Yes 0=No)	896	0.406	0.491	0	1
Row planting (1=Yes 0=No)	896	0.710	0.454	0	1
Fertilizer application (1=Yes 0=No)	896	0.607	0.489	0	1
Seed rate (1=Yes 0=No)	896	0.334	0.472	0	1
Weed management (1=Yes 0=No)	896	0.701	0.458	0	1
Others (1=Yes 0=No)	896	0.388	0.488	0	1
Number of practices used	896	3.146	1.234	1	6
Independent variables					
Sex of the household head (1=Male 0=Female)	896	0.738	0.440	0	1
Marital status					
Single (1=Yes 0=No)	896	0.073	0.260	0	1
Married (1=Yes 0=No)	896	0.818	0.386	0	1
Divorced/ Widowed (1=Yes 0=No)	896	0.109	0.312	0	1
Education level of the household head					
No formal education (1=Yes 0=No)	896	0.048	0.214	0	1
Primary (1=Yes 0=No)	896	0.484	0.500	0	1
Secondary (1=Yes 0=No)	896	0.371	0.483	0	1
Tertiary/Higher education (1=Yes 0=No)	896	0.097	0.296	0	1
Household Main occupation (1=Full time farming 0=Part time farming)	896	0.801	0.399	0	1
Age of household head	896	46.888	11.988	23	82
Farm Size (ha)	896	4.873	5.206	0	70
Farming experience (years)	896	12.563	10.133	1	50
Household size	896	7.448	3.858	1	43
Member to farmers' group (1=Yes 0=No)	896	0.795	0.404	0	1
Access to credit (1=Yes 0=No)	896	0.737	0.441	0	1

Source: Author's calculation

4.1.2 Number of agronomic practices used by beans farmers

Table 2 illustrates the distribution of the number of agronomic practices adopted by bean farmers. The results show that 7.9% of the farmers adopted one agronomic practice, 24% adopted two practices, 33% adopted three practices, 18.3% adopted four practices, 14.1% adopted five practices, and 2.7% adopted all six agronomic practices included in the study.

Table 2: Descriptive statistics for the number of agronomic practices adopted by the beans farmers

Number of practices adopted	Freq.	Percent
1	71	7.9
2	215	24.0
3	296	33.0
4	164	18.3
5	126	14.1
6	24	2.7
Total	896	100.00

Source: Author's calculation

4.1.3 Average Marginal Effects of the Multivariate Probit and the Poisson Estimates for beans Farmers on Adoption of Agronomic Practices

Table 3 presents the average marginal effects from the multivariate Probit and Poisson estimates regarding the adoption of agronomic practices by bean farmers. The following discussion focuses on covariates that significantly influenced the adoption of various agronomic practices, as shown in Table 8. The discussion is organized by covariate, as the effect of each independent variable on the adoption of agronomic practices is generally consistent across different practices. Below are the key factors that significantly affect the adoption of the various agronomic practices.

4.2 Sex of the Household Head

Results indicate being a male-headed compared to a female-head household on average decreases the likelihood of adoption of others by 11.8%. This is partly because men are involved in other income generating activities to provide for the family hence limiting factor to work on the farm as well as access to extension services. This is because women bear most of the household and farm responsibilities (Quisumbing, et al., 2014) and therefore men are not fully engaged in the farm activities. These findings are consistent with that of (Kassie, Zikhali, Manjur, & Edwards, 2009) who found out that male-headed household's probability of adopting the use of compost decreased and underscored the need to avoid generalizing the impact of gender on agronomic practice adoption, emphasizing that the impact of gender on adoption is practice-specific.

4.3 Marital Status

Being married compared to being single on average, increases the likelihood of adoption of crop rotation by 15.7%. This is because married couple households engage significantly in organized farming that include adoption of agronomic practices than other types of households. These findings concur with studies by (Tisdell, 2014) who reported that married farmer's work more hours than unmarried ones, working not only cash food crops but also on non-food cash crops and therefore easily adopt these agronomic practices.

Still, being widowed/divorced compared to being single on average decreases the likelihood of adoption of fertilizer application by 15.6% but increases the likelihood of adoption of crop rotation by 26.5%. This reduction in the probability of adoption of fertilizer application is partly due to the fact that fertilizer application requires more labor, hence increasing costs.

4.4 Educational level

Relating to education level, completing secondary compared to having no formal education on average increases the likelihood of adoption of fertilizer application by 17.3%. Also, completing tertiary/higher education compared to having no formal education on average increases the likelihood of adoption of row planting and seed rate by 17.3% and 18.3% respectively. This result simply shows the importance of education in raising the awareness of the farmer and increasing the farmer's chances of adopting important agronomic practices. Results are consistent with those of several other studies (Amsalu & Graaff, 2007) who found that educated farmers are able to process information and evaluate practices.

Table 3: Average Marginal Effects of the Multivariate Probit and the Poisson Estimates

Variable	dy/dx for multivariate probit model estimates						dy/dx for Poisson estimates
	Row planting	Fertilizer application	Weed management	Crop rotation	Seed rate	Others	Number of practices used
Sex ref (female) Male (1=Male 0=Female)	0.044 (0.008)	-0.084 (0.009)	0.075 (0.005)	0.082 (0.014)	0.060 (0.007)	-0.118** (0.014)	0.053 .199)
Marital status ref (single) Married (1=Yes 0=No)	0.107 (0.019)	-0.002 (0)	-0.027 (0.003)	0.157** (0.027)	-0.047 (0.006)	0.064 (0.008)	0.263 (0.265)
Widowed/Divorced	0.089(0.015)	-0.156* (0.016)	0.106 (0.012)	0.265*** (0.045)	-.003 (0)	-0.076 (0.009)	0.204 (0.287)
Education level ref (No formal education) Primary (1=Yes 0=No)	0.108 (0.019)	0.026 (0.003)	0.068 (0.008)	-0.007 (0.001)	0.096 (0.012)	-0.039 (0.005)	0.242 (0.278)
Secondary (1=Yes 0=No)	0.063 (0.011)	0.173** (0.018)	0.015 (0.002)	0.065 (0.011)	0.114 (0.014)	0.060 (0.007)	0.489 (0.293)
Tertiary/Higher (1=Yes 0=No)	0.156* (0.027)	0.147 (0.015)	-0.09 (0.01)	0.110 (0.019)	0.183* (0.022)	-0.068 (0.008)	0.457 (0.338)
Main occupation (ref =Part time Agriculture) Full time Agriculture	0.094** (0.016)	0.044 (0.004)	-0.071 (0.008)	-0.086** (0.015)	0.031 (0.004)	-0.008 (0.001)	0.006 (0.156)
Age	0.001 (0)	0 (0)	-0.002 (0)	0.006*** (0.001)	0.002*** (0)	0.006 (0.001)	0.012** (0.006)
Size of farm land(ha)	-0.005 (0.001)	-0.009** (0.001)	-0.003 (0)	-0.003 (0.001)	0.002 (0)	-0.014*** (0.002)	-0.037** (0.015)
Farmer experience	0.064*** (0.011)	0 (0)	0.003* (0)	0.003* (0.001)	0 (0)	-0.001 (0)	0.01 (0.006)
Household Size	-0.006 (.001)	-0.007 (0.001)	0.004 (0)	-0.014*** (0.041)	-0.014*** (0.002)	-0.001 (0)	-0.036* (0.019)
Belonging to a Farmer group ref (No)	-0.026 (0.005)	-0.024 (0.002)	-0.024 (0.003)	0.244*** (0.004)	0.128*** (0.016)	0.151*** (0.018)	0.427** (0.150)

Yes (1=Yes 0=No)							
Access to credit ref (No) Yes (1=Yes 0=No)	-0.105 (0.018)	0.136** (0.014)	0.038 (0.004)	-0.024	-0.168** (0.021)	0.008 (0.001)	-0.051 (0.143)

*Standard errors in parentheses, *** p<0.01, ** p<0.05, * p<0.1*

4.5 Main occupation

With regards to main occupation, being a full-time farmer compared to being a part-time farmer increases the likelihood of adoption of row planting by 9.4% on average. However, being a full-time farmer compared to being a part-time farmer on average decreases the likelihood of adoption of weed management and crop rotation by 7.1% and 8.6% respectively. This is because being a full-time rather than a part-time farmer acts as a catalyst for continuation since agronomic practices require adequate expertise and an active presence in the farm. This finding is consistent with that of Bartolini et al. (2013), Morgan et al. (2015), and Pierpaoli et al. (2013). In addition, Teshome et al. (2016) found out that farmers' involvement in full time farming is positively related to maintaining agronomic practices. However, findings also show that being a full-time farmer compared to being a part-time farmer decreases the probability of adopting crop rotation and weed management. This finding contradicts with the finding of Teshome et al. (2016) who found full-time farming is positively related to maintaining agronomic practices.

4.6 Age

Furthermore, a unit increase in age of the household head increases the likelihood of adoption of crop rotation and others by 0.6% on average. Also, a unit increase in age of the household head increases the expected number of agronomic practices used by a farmer by 1.2%. This is because older bean farmers are more skilled and more experienced in adopting agronomic practices to maximize productivity. Results are consistent with those of (Amsalu & Graaff, 2007), who found a significant positive relation between age and the adoption of crop rotation (Amsalu & Graaff, 2007).

4.7 Farm size

Relating to farm size, a unit increase in the size of the farmland on average decreases the likelihood of adoption of fertilizer application and others by 0.9% and 1.4% respectively. Also, a unit increase the size of the farmland decreases the expected number of agronomic practices used by a farmer by 3.7%. This might be due to the fact that farmers with the large size of cultivated land have fear of incurring the cost of buying inputs like fertilizers. This result affirms with a study done by Deressa et al. in the Nile basin of Ethiopia to analyze farmers' perception and adoption to agronomic practices, which supports the notion that the negative relationship between farm size and adoption could be due to the fact that there are additional costs incurred as farm size increases.

4.8 Farming experience

A unit increase in the farming experience on average increases the likelihood of adoption of row planting, weed management and crop rotation by 6.4%, 0.3% and 0.3% respectively. Farming experience is useful in early stages of adoption of a given practice when farmers are still testing its potential benefits, which later determine its retention or dis-adoption over time. A probable explanation is that farmers with a lot of experience easily get information from extension personnel and other sources. Consequently, they tend to be aware of new developments in agricultural systems and hence assess and adopt new practices more often than younger farmers.

4.9 Household size

A unit increase in the household size on average decreases the likelihood of adoption of crop rotation, and seed rate by 1.4% respectively. Also, a unit increase in the household size decreases the expected number of agronomic practices used by a farmer by 3.6%. On the contrary, the households with larger family size have the necessary labor to apply the recommended agronomic practices on their farm plots. This finding contradicts the finding by (Assaye1, Habte, & Sakurai1, 2023) which shows that family members are the main source of household labor for rice cultivation. Therefore, family size positively effects on adopting recommended agronomic practices.

4.10 Farmer group

Belonging to a farmer group compared to not belonging to a farmer group on average increases the likelihood of adoption of crop rotation, seed rate and others by 24.4%, 12.8% and 15.1% respectively. Also, belonging to a farmer group compared to not belonging to a farmer group increases the expected number of agronomic practices used by a farmer by 42.7%. This is because some farmers in the groups who are early adopters of certain practices can share testimonies (success stories) on the practices they tried, which can encourage other farmers to adopt those particular practices. Bandiera and Rasul (2006) also found that group membership enhances social networking, which facilitates the sharing of experiences about technologies and building confidence in those interested in the practices.

4.11 Access to credit

Accessing agricultural credit compared to not accessing agricultural credit on average increases the likelihood of adoption of fertilizer application by 13.6% but decreases the likelihood of adoption of seed rate by 16.8%. This is because credit provision has the advantage to solve financial constraints to meet their need to purchase the fertilizers. These results are in line with the findings from Deressa et al. and Gbetibouo who reported that farmers with more financial and other resources at their disposal are able to make use of all their available information to invest on the use of irrigation, use of agricultural inputs, use of drought tolerant crop species, use of SWC, and take up livelihood diversification in response to changing climatic and other conditions (Amare & Simane, 2017). However, accessing credit compared to not accessing credit for agricultural production decreases the likelihood of adoption of seed rate. This finding contradicts the above previous finding by Deressa et al. and Gbetibouo.

4.12 Summary of the findings

The adoption of various agricultural practices is influenced by several factors. Farmers with higher education (tertiary level), full-time farming status, and more farming experience are more likely to adopt row planting and seed rate practices. Similarly, higher education and access to credit positively influence fertilizer application, though this adoption decreases with secondary education and larger farm sizes. Increased farming experience enhances weed management adoption, while crop rotation is more common among married, divorced, or widowed farmers, older farmers, and those in farmer groups. However, crop rotation is less likely among full-time farmers, those with larger households, and those with credit access. Membership in farmer groups also drives the adoption of other agronomic practices like mulching and intercropping, though larger farmland sizes can deter this. Overall, the number of practices adopted increases with age but decreases with larger farm sizes and household sizes.

4.13 Recommendations

The adoption of row planting is positively influenced by having a tertiary education compared to no formal education. Therefore, agricultural support services, researchers, educators, and extension agents should focus on tailoring information dissemination channels based on farmers' education levels. This approach can better motivate farmers to make informed decisions and adopt row planting. Additionally, full-time farmers are more likely to adopt row planting than part-time farmers. As a result, the government of Uganda and relevant stakeholders should ensure that information on row planting reaches not only large-scale farmers, who are often full-time, but also small-scale farmers, given that agriculture is a cornerstone of Uganda's economy. Moreover, increased farming experience also promotes the adoption of row planting. Leveraging the knowledge of more experienced farmers in training and sensitizing less experienced or younger farmers on various agronomic practices could further enhance adoption rates.

The adoption of fertilizer application is positively influenced by having tertiary education compared to no formal education. Therefore, agricultural support services, researchers, educators, and extension agents should tailor information dissemination channels to farmers' education levels, ensuring they are more motivated to make informed decisions and adopt fertilizer application. Access to credit also positively impacts fertilizer adoption, highlighting the need for the government to strengthen rural financial institutions and farmer associations to offer credit, especially since smallholder farmers often face challenges in accessing credit. The government should also consider providing inputs such as fertilizer and herbicides on credit. Conversely, secondary education compared to no formal education negatively affects fertilizer adoption, suggesting that training programs should be equitable and cater to all education levels. Additionally, larger farm sizes discourage fertilizer use, indicating a need for farmers to be educated on the pros and cons of adopting agronomic practices based on their farm size, taking costs into account.

The adoption of weed management practices increases with farming experience, so experienced farmers should be involved in educating younger farmers about effective weed management techniques. Crop rotation is more likely to be adopted by married or divorced/widowed farmers than by single ones, making marital status a significant factor in adopting agronomic practices. Policymakers should consider marital status when designing incentives to encourage the adoption of multiple practices, ensuring that all farmers can maximize the benefits of crop rotation. Older age also positively influences crop rotation adoption, which suggests the need to create public social networking platforms, cooperative organizations, and activity centers where older farmers can mentor younger ones. Membership in farmer groups also promotes crop rotation, so forming or joining farmer groups focused on sharing agronomic information should be encouraged.

However, being a full-time farmer, as opposed to a part-time farmer, negatively affects crop rotation adoption, indicating that information on crop rotation should be targeted not only at large-scale, full time farmers but also at small-scale farmers, given Uganda's strong agricultural base. Larger household sizes also negatively impact crop rotation adoption, suggesting that farmers need to learn how to utilize their household size as a resource. Credit access also negatively impacts crop rotation adoption, reinforcing the need for policies that provide inputs on credit.

For seed rate adoption, full-time farmers and older farmers are more likely to adopt proper seed rates, highlighting the need for government and stakeholders to spread information about this practice to all farmers, including small-scale ones. Additionally, promoting the formation of farmer groups can enhance seed rate adoption. Other agronomic practices such as mulching, intercropping, and minimum tillage are also positively influenced by farmer group membership, further emphasizing the importance of farmer groups in disseminating information. However, larger farm sizes discourage the adoption of

these practices, indicating that farmers should be made aware of the pros and cons of different practices based on farm size, considering costs and efficiency.

Finally, the number of agronomic practices adopted increases with age, reinforcing the importance of community-based initiatives that allow older farmers to guide younger ones. On the other hand, larger farm sizes and household sizes negatively impact the number of practices adopted, suggesting that farmers need to be educated on how to turn these factors into assets rather than barriers to adopting agronomic practices.

V. DECLARATION OF COMPETING INTEREST

The authors of this paper declare no conflict of interest.

REFERENCES

1. Amare, A., & Simane, B. (2017). Determinants of smallholder farmers' decision to adopt adaptation options to climate change and variability in the Muger Sub basin of the Upper Blue Nile basin of Ethiopia. *Agriculture & Food Security*.
2. Amsalu, & Graaff, D. (2007). Determinants of adoption and continued use of stone terraces for soil and water conservation in an Ethiopian highland watershed. *Ecological economics*, 61(2-3), 294-302.
3. Assaye1, A., Habte, E., & Sakurai1, S. (2023). Adoption of improved rice technologies in major rice producing areas of Ethiopia: a multivariate probit approach. *Agriculture & Food Security*.
4. Kassie, M., Zikhali, P., Manjur, K., & Edwards, S. (2009). Adoption of Organic Farming Techniques: Evidence from a Semi-Arid Region of Ethiopia. *Environment for Development Initiative*.
5. Quisumbing, Meinzen-Dick, Raney, Croppenstedt, Behrman, & Peterman. (2014). Closing the knowledge gap on gender in agriculture. Gender in agriculture: Closing the knowledge gap. 3-27.
6. Tisdell, C. A. (2014). *Sustainable agriculture*. Edward Elgar Publishing.

This page is intentionally left blank

The Pink Rocks of Carlo Crivelli (circa 1489)

Alessandro Montanari, Gaia Pignocchi, Gianluca Mainiero & Maurizio Mainiero

Università di Camerino

ABSTRACT

Until the 1800s, art historians considered the Venetian artist Carlo Crivelli (circa 1435– 1495) to be a secondary if not a minor painter. This lack of recognition stems essentially from the dissemination of his paintings in churches and convents throughout the provincial region of Marche (central-eastern Italy), where Crivelli spent the most productive period of his life from 1468 until his death in 1495. As a consequence of this limited accessibility, his paintings could not be seen by mainstream art dealers and historians such as the scrupulous Giorgio Vasari (1511–1574). More than anybody else, the British demonstrated a great interest in Crivelli's art in the late 1800s by acquiring many of his dispersed paintings that eventually ended up in the National Gallery of London, where the richest collection of the artist's paintings is preserved today. Among them, 'The Vision of the Blessed Gabriele' is the one that attracted our attention not so much for its pictorial qualities and symbolic significance typical of Renaissance paintings, but rather for the many details making up the background of the painting, which accurately depicted the geological and environmental characteristics of the Adriatic port city of Ancona and the nearby Monte Cònero mountain.

Keywords: carlo crivelli; the vision of the blessed gabriele; umbria; marche; scaglia rossa formation; ancona monte cònero.

Classification: LCC Code: N8213.G4, ND623.C75, QE26

Language: English

Great Britain Journals Press

LJP Copyright ID: 925603
Print ISSN: 2631-8490
Online ISSN: 2631-8504

London Journal of Research in Science: Natural & Formal

Volume 26 | Issue 1 | Compilation 1.0

The Pink Rocks of Carlo Crivel (circa 1489)

Alessandro Montanari[α], Gaia Pignocchi[σ], Gianluca Mainiero[ρ]
& Maurizio Mainiero[ↀ]

ABSTRACT

Until the 1800s, art historians considered the Venetian artist Carlo Crivelli (circa 1435– 1495) to be a secondary if not a minor painter. This lack of recognition stems essentially from the dissemination of his paintings in churches and convents throughout the provincial region of Marche (central-eastern Italy), where Crivelli spent the most productive period of his life from 1468 until his death in 1495. As a consequence of this limited accessibility, his paintings could not be seen by mainstream art dealers and historians such as the scrupulous Giorgio Vasari (1511–1574). More than anybody else, the British demonstrated a great interest in Crivelli's art in the late 1800s by acquiring many of his dispersed paintings that eventually ended up in the National Gallery of London, where the richest collection of the artist's paintings is preserved today. Among them, 'The Vision of the Blessed Gabriele' is the one that attracted our attention not so much for its pictorial qualities and symbolic significance typical of Renaissance paintings, but rather for the many details making up the background of the painting, which accurately depicted the geological and environmental characteristics of the Adriatic port city of Ancona and the nearby Monte Cònero mountain. In this research, besides a meticulous study of architectural, geomorphologic, faunal, and floral details, we focused on the representation of a large outcrop of strikingly pink, thinly stratified rocks, which we studied through a quantitative RGB (red, green, blue) chromatic analysis and then compared the results with those from an analogous analysis of rock samples and outcrop images of all the more-or less red formations of the Umbria-Marche lithostratigraphic succession. This led us to the conclusion that Crivelli's pink rocks represent the lower Paleogene Scaglia Rossa limestone exposed at Monte Cònero. Thus, the background of Crivelli's painting 'The Vision of the Blessed Gabriele' is no longer an idealized landscape put there as a symbolic or simple wing of a theater stage, but a realistic representation of the physical environment surrounding the main subject of the painting as only a few Renaissance maestros like Piero della Francesca, Andrea Mantegna, and Leonardo da Vinci incorporated in their most famous and studied masterpieces.

keywords: carlo crivelli; the vision of the blessed gabriele; umbria; marche; scaglia rossa formation; ancona monte cònero.

Author α: Osservatorio Geologico di Coldigioco, Cda. Coldigioco 4, 62021 Apiro, Italy.
σ: Scuola di Scienze e Tecnologie, Università di Camerino, Via Gentile III da Varano, 62032 Camerino, Italy.
ρ: Graphic Designer, Via XXIX Settembre 2/o, 60122 Ancona, Italy.
ↀ: Studio Geologico, Via XXIX Settembre 2/o, 60122 Ancona, Italy.

I. INTRODUCTION

1.1 Carlo Crivelli's painting of 'The Vision of the Blessed Gabriele'

Around 1489, the Venetian artist Carlo Crivelli painted a work in gold and tempera grassa (i.e., fat egg tempera emulsion) on a 141 x 87 cm poplar panel, of the Franciscan Friar Gabriele Ferretti praying to the apparition of the Virgin Mary and Child suspended in the sky above the convent of San Francesco ad Alto in Ancona. The painting, which was a commission funded by the Ferretti local nobility, is now

preserved in the National Gallery of London, and it is known as '*The Vision of the Blessed Gabriele*' (Figure 1). Besides the central figure of the kneeling Gabriele, the background is divided into two vertical halves. The right half portrays images of Ancona including the church of San Francesco ad Alto, and the left side portrays geological, faunal, and floral details including a range of iconographical subjects set in a naturalistic environment surrounding Ancona. The image of a large natural exposure, which comprises about 1/6 of the picture plane, is comprised of thinly bedded rocks exhibiting a peculiar pink color, an uncommon color used by contemporary Renaissance artists for representing rocks, with the exception of Andrea Mantegna (see Section 4 below). As a working hypothesis, we have identified these pink rocks as the upper Cretaceous-lower Paleogene Scaglia Rossa Formation, the peculiar color of which must have impressed the artist during his sojourn in Ancona in the late 1480s. This would be the very first iconographic representation of this geological formation, which is famous in the scientific community all over the world (*e.g.*, Alvarez 2019, and references therein). With this working hypothesis in mind, we have undertaken a study of the environmental details of this painting, including a RGB (red, green, blue) chromatic analysis of Crivelli's pink rocks and, for comparison, of all the more-or-less red rocks of the Umbria-Marche (U-M) lithostratigraphic succession.

1.2 History of the Franciscan convent and church of San Francesco ad Alto in Ancona

We summarize here the information gathered from various historical sources and used to reconstruct the aspect of the convent of San Francesco ad Alto and, above all, the homonym church at the time Carlo Crivelli depicted it around 1489. The monastic convent and its enclosed church of San Francesco ad Alto are on the hill of Colle Astagno on the outskirts of the city of Ancona (see Figures 2A-B for location). The convent was built in the 13th century by Franciscan minor friars. It later became an important sacred place for local noble families and went through profound architectural changes and remodeling in the following centuries. Eventually, following the suppression of religious orders during the Napoleonic occupation of Ancona in 1797, and the utilization of the whole San Francesco complex as a French military compound in 1798, the transformation became definitive following the Italian royal Decree Valerio on 3 January 1861. In 1815, after the fall of the Napoleonic government, the complex was returned to the Order of the Franciscan Minor Friars and, after various vicissitudes, in 1862 the church and the surrounding complex were definitively annexed to the State. The property was granted to the Command of the Army of Ancona to be transformed into a military hospital with the complete dismantling of altars, chapels, and apse, and the removal of all liturgical furnishings and artistic objects (Mariano 2017; Cogliandro and Tittarelli 2019).

The San Francesco complex was transformed after the Second World War into an Italian Military District and, in more recent years became the headquarters of the Military Command of the Army of Marche (CME) and the center of military archival documentation of Ancona (Figure 2C). Today only the cloister, which was completed by Friar Nicolò Bonarelli in 1614, remains intact, and of the cycle of frescoes in the lunettes by 17th century painters Domenico and Giovanni Peruzzini, only few small shreds are still preserved (Mariano 2017). In summary, we are reporting here relevant pieces of information to reconstruct the historical vicissitudes and above all the representation of the San Francesco church and its surroundings at the time when Carlo Crivelli portrayed them in 1489 (Figure 1).

The actual painting by Crivelli, which represents the vision of the *Beato* (*i.e.*, blessed) Gabriele Ferretti in ecstasy in front of the church, was commissioned by Friar Bernardino Ferretti, who was the nephew of the eminent Gabriele (Ancona, 1385–1456). More detailed information about the church can be found in a manuscript by Friar Carlo Gasparini (Gasparini 1648) following notes previously provided by Bernabei (1497), Ferretti (1580), and Gonzaga (1587).

Figure 1: *'The Vision of the Blessed Gabriele': oil and tempera on board, 141 x 87 cm, by Carlo Crivelli (circa 1489), reproduced with permission from the National Gallery of London.*

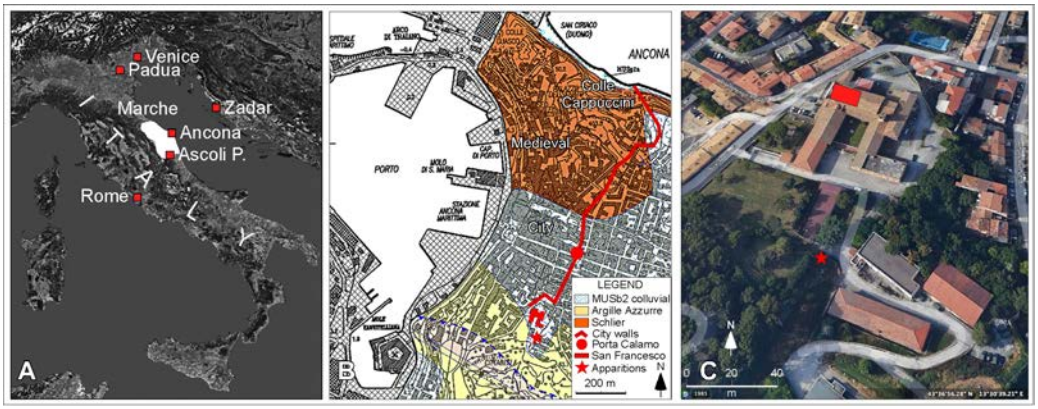

Figure 2: (A) Italy with locations mentioned in the text; (B) Geologic map of the city of Ancona (from Regione Marche 2003) with location of the convent of San Francesco ad Alto and the no longer existing Porta del Calamo; (C) Aerial view of the complex of San Francesco ad Alto and presumed location and orientation of the San Francesco church rebuilt in 1480 (red rectangle: see text for explanation).

First of all, the building of the church and the annexed convent dates back to 1219 according to tradition or 1220 from other sources. *Annus Domini* 1219 would be the year when Saint Francis of Assisi passed by Ancona before leaving for Damietta (Egypt) during the 5th Crusade to meet with Malik al-Kāmil, the sultan of Egypt and Palestine, and nephew of Saladin. In reality, this encounter is not supported by historical sources, and for the same reason it is not ascertainable whether Saint Francis was present in Ancona in those years.

For certain, in the 13th century there was a small Franciscan church outside the medieval city walls of Ancona, an isolated and high (*alto* in Italian) place, which was appropriate for, and typical of the characteristics and hermitage spirit of original Franciscan friars. The first report of the existence of a Franciscan settlement in Ancona can be found in a document dated 19 September 1239, which records "*. . . apud ecclesiam S. Francisci de Ancona*" (Talamonti 1936).

The Franciscan settlement on the Colle Astagno hill fell into disuse after construction in the city center of a new church dedicated to Saint Mary Major (later San Francesco alle Scale), and a new convent of minor friars probably in 1323, which was better suited to the new Franciscan mission aimed at a direct relationship with the citizens.

The old convent on the Colle Astagno hill, regained life thanks to Gabriele Ferretti who entered the order of the Friars Minor Observant in 1403 when he was eighteen, and the Franciscans established their headquarters at the convent of San Francesco ad Alto. In 1425, Friar Gabriele was nominated guardian of the church and he planned the enlargement of the dormitory and the construction of new walls around the complex in addition to restructuring the church by ". . . constructing a certain addition on the front of said church on the side that looks toward the Cassero" (Albertini 1824; Cogliandro and Tittarelli 2019). The 'Cassero', as it was named by military architect Giacomo Fontana in 1588, refers to the fortification walls that were built by architect Antonio da Sangallo in the 1530s, which were located on the Colle dei Cappuccini hill, then called Colle di San Cataldo, along the line of the ancient 14th century city walls on the north eastern side of the Colle Cardeto hill, not far from the north-facing coastal cliffs (see Figure 2B for location).

New radical restructuring projects in the late 15th century were conducted by Friar Bernardino Ferretti, nephew of blessed Gabriele Ferretti. Consequently, in addition to the enlargement and also a reorientation of the church, the new façade and its stepped churchyard were now facing no longer

toward the northeast but toward the northwest (Figure 2C). Therefore, the San Francesco church depicted by Crivelli in his 1489 painting, had its new orientation toward the northwest since 1480, with the apse on the southeastern end of the church. Gabriele Ferretti was particularly devoted to the Virgin Mary, who supposedly appeared to him with baby Jesus in the woods of the convent where the pious friar used to go to pray in solitude.

1.3 Carlo Crivelli's Painting of the Blessed Gabriele Ferretti: A Hectic Life Story

Carlo Crivelli's painting of '*The Vision of the Blessed Gabriele*' was originally located above the monumental sarcophagus containing the body of the blessed friar. The sarcophagus was commissioned in 1483 to the Istrian sculptor Giannetto di Domenico da Brioni and the two Lombard sculptors Baldassarre and Taddeo, who finished it in 1489, and it was decorated with elaborated bas-relief festoons, which were inspired by the paintings of Crivelli himself. Right after his death on 12 December 1456, the body of the reverend friar was buried in the ground to the left of the entrance to the church. In 1489 Gabriele's body was exhumed and translated in his new precious urn following some prodigies that occurred near the original humble tomb.

Four years after the beatification of Gabriele Ferretti by Pope Benedict XIV in 1753, the body was moved again to a dedicated chapel in the same church, the first chapel on the left entering from the main portal. On that occasion, Crivelli's painting was replaced with the painting '*Visione del Beato*' by Stefano Parrocel in 1756. Parrocel reproduced with a certain fidelity many symbolic details of the original painting, such as the central figure of a praying Gabriele, the San Francesco church, the gold finch roosting on a branch of an apparently dead tree, and the glimpse of the fortified city of Ancona. However, he omitted many other details that had environmental or naturalistic meanings, such as the pond with the mallard ducks, the profile of the Apennine mountains in the far background, and above all the conspicuous exposure of thinly bedded pink rocks, which Parrocell reproduced as massive rocks using a reddish-brown color (see: https//www.museodiocesanoancona.it/sala-10/). Eventually, the original Crivelli was returned to the Ferretti family, who sold it in order to pay debts incurred by Archbishop Raimondo Ferretti. It was the husband of Maria Elisabetta Ferretti, the daughter of Raimondo, who sold the precious painting to the art collector Alexander Barker and it was ultimately acquired by the National Gallery of London in 1874. Following the suppression of the religious order of the minor friars, the body of blessed Gabriele was temporarily placed in the cathedral of San Ciriaco until 1884 when the San Giovanni Battista church in the Capodimonte quarter of Ancona, also on the Colle Astagno hill, was assigned to the Franciscans. The body was then placed in this new Franciscan church and it is still preserved there along with the copy of Crivelli's painting by Stefano Parrocel.

II. MATERIALS AND METHODS

We used a high-resolution JPG image with a RGB scale of Carlo Crivelli's painting depicting Gabriele Ferretti, which was provided by the National Gallery of London, to carry out an environmental study of architectural, faunal, floral, and landscape images portrayed in the painting, and a chromatic RGB analysis of the pink rocks outcrop portrayed on the left side of the same painting (Figure 1). The result of this chromatic analysis was then compared with the results of an analogous RGB analysis of rock samples and exemplar outcrop images of all the more-or less red lithostratigraphic units of the Umbria-Marche succession (Figure 3). We utilized the same high-resolution image of Crivelli's painting to analyze and identify any other faunal and floral feature that could be related, or not related, to the anthropic or naturalistic environment of Ancona and the nearby Monte Cònero mountain.

III. ANALYTICAL RESULTS

3.1 General description

Carlo Crivelli's masterpiece titled '*The Vision of the Blessed Gabriele*' was painted with oil and tempera on poplar panel, and it represents a kneeling and praying Friar Gabriele Ferretti looking up to the apparition of the Virgin Mary with the Child (Figure 1). The right side of the painting depicts a number of images of Ancona, namely a side view of the San Francesco ad Alto church, a glimpse of the fortified medieval city, and a panorama of the gulf of Ancona in the far back-

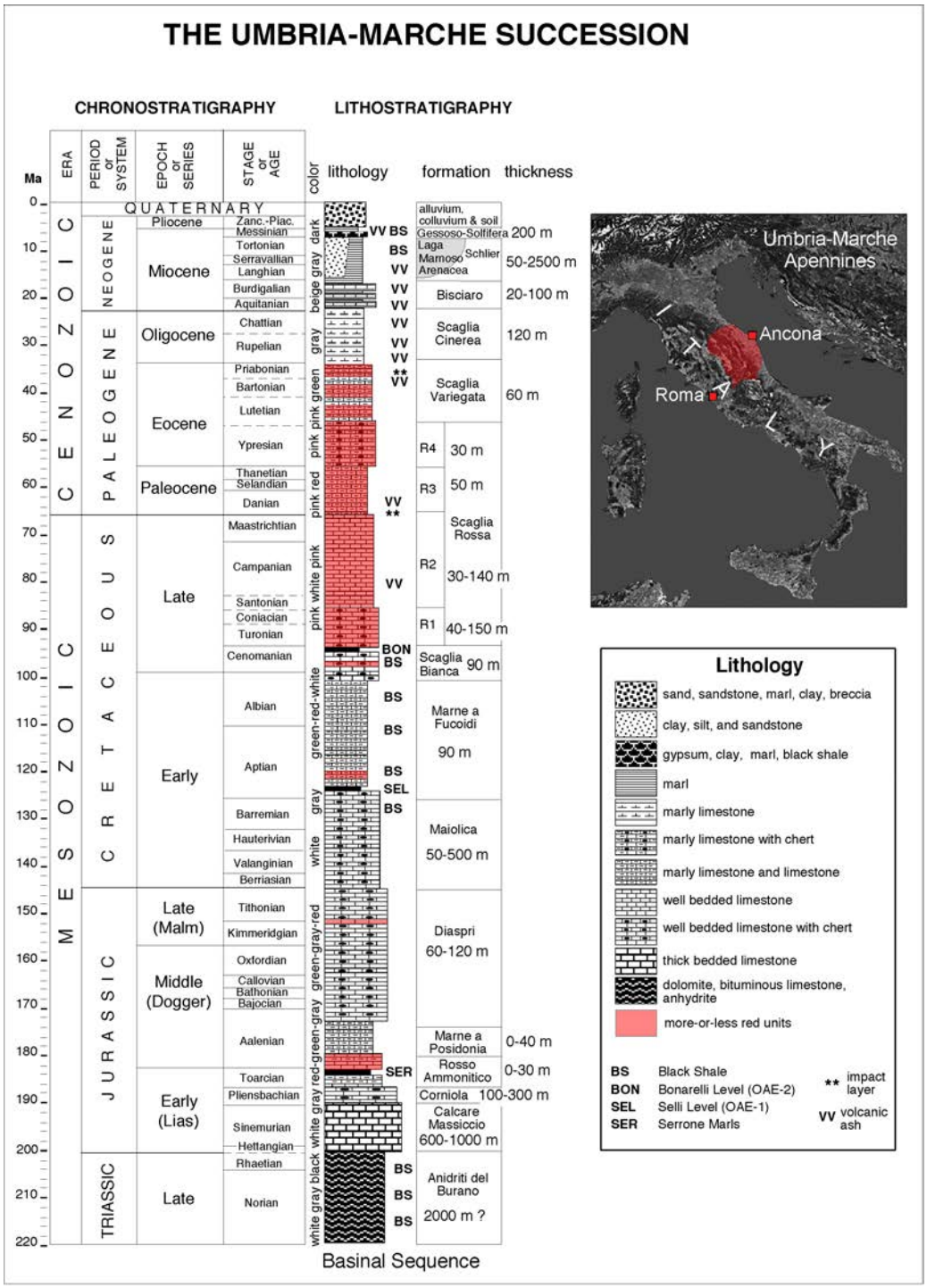

Figure 3: The lithostratigraphic succession of the Umbria-Marche Apennines.

ground. The left side of the painting is dominated by a large exposure of thinly bedded rocks exhibiting a peculiar pink color, and other naturalistic details such as a water spring, a thick forest, a water pool with two ducks in it, and various plants growing on a rocky floor disseminated with rounded pebbles. Gabriele Ferretti is not the only human figure in the painting. Hidden in the bushes in the center of the painting, one can notice the profile of a man wearing a white hood, a mysterious figure described as a generic monk of unknown identity by Peers (2005). By comparing the traits of this human figure with the three-quarter-profile in Crivelli's Saint Paul depicted in the Sant'Emidio polyptych altarpiece in Ascoli Piceno, which was recently identified as a self-portrait painted in 1473 by professional restorer Rossana Allegri (Dal Bello 2021), it emerges that the profile of this mysterious monk in Beato Gabriele is also a self-portrait of an older Carlo Crivelli (Figure 4 ABC). As a matter of fact, it was very common for Renaissance painters to insert, besides the likeness of saints, popes, or princes, their own portraits sometimes hidden in a corner of the painting or as representing a particular historical or mythological personage, *e.g.*, the self-portrait of Crivelli as Saint Paul in his polyptych of Sant'Emidio in Ascoli.

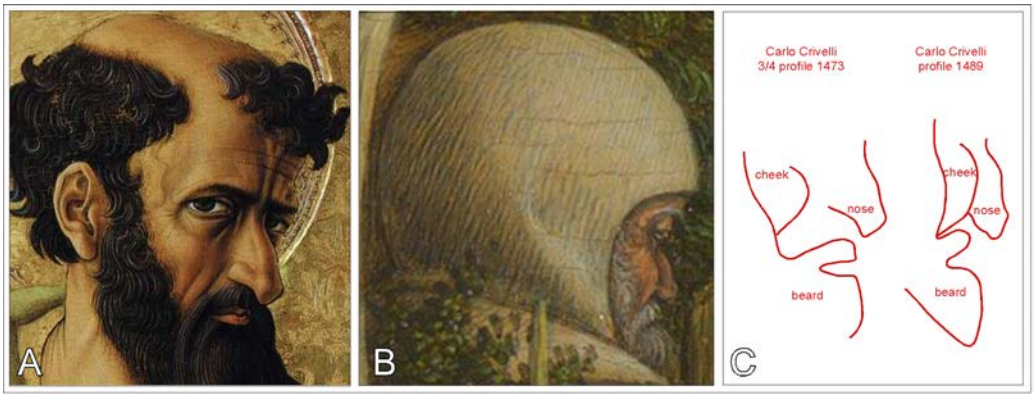

Figure 4: Self-portrait analysis of Carlo Crivelli. (A) Self-portrait impersonating Saint Paul in Crivelli's polyptych altarpiece of Sant'Emidio in the cathedral of Ascoli Piceno, 1473 (Casalini 2004). Note that the original image was flipped horizontally for correlating it with the profile in B; (B) Herein proposed self-portrait in Crivelli's Beato Gabriele Ferretti, 1489, National Gallery of London; C) Trait line profiling of cheek, beard, and nose comparing the profiles in A and B.

3.2 Architectural and landscape features

On the right half of Crivelli's 1489 painting, the main architectural feature is a partial view of the northeastern side of the San Francesco ad Alto church, which was restructured in 1480 by Friar Bernardino Ferretti, nephew of blessed Gabriele (Figure 5A). The church and the frontal (*i.e.*, northwestern) porch were built with red terracotta bricks, whereas the apse on the southeastern side of the church, as well as the typically Renaissance decorative moulding, were made with squared white limestone blocks. From there, a dirt road descends toward the no-longer-existing access, through the walls of medieval Ancona, of Porta del Calamo built in 1329 (Figure 5B). While the picture of Ancona by Crivelli is somewhat stylized, the crenellated walls can be recognized in a realistic painting by local artist Barnaba Mariotti (mid-19th century; Figure 5C). The church with its campanile visible in Mariotti's painting may represent the original 13th century San Domenico church, then rebuilt in 1771. Nevertheless, from this elevated position and therefore looking toward the northeast, Crivelli could see the city from above, including the medieval walls, the door of Porta del Calamo, and the church of San Domenico. However, in the far background of this view, he would see the Colle dei Cappuccini hill (at 106 m above sea level (asl); see Figure 2B for orientation), and not the gulf of Ancona surrounded by coastal hills, as seen in the far background of the painting (Figure 6A). In effect, from the top of the Colle Astagno hill (109 m asl) currently occupied by the 16th century fortress of La Cittadella, one can

enjoy a beautiful view of the gulf of Ancona with its hilly coast and, on a clear day looking toward the west-southwest, one can distinctly see the Marche Ridge of the Apennine mountains (Figure 6B) with its most prominent peak of Monte San Vicino (1480 m asl).

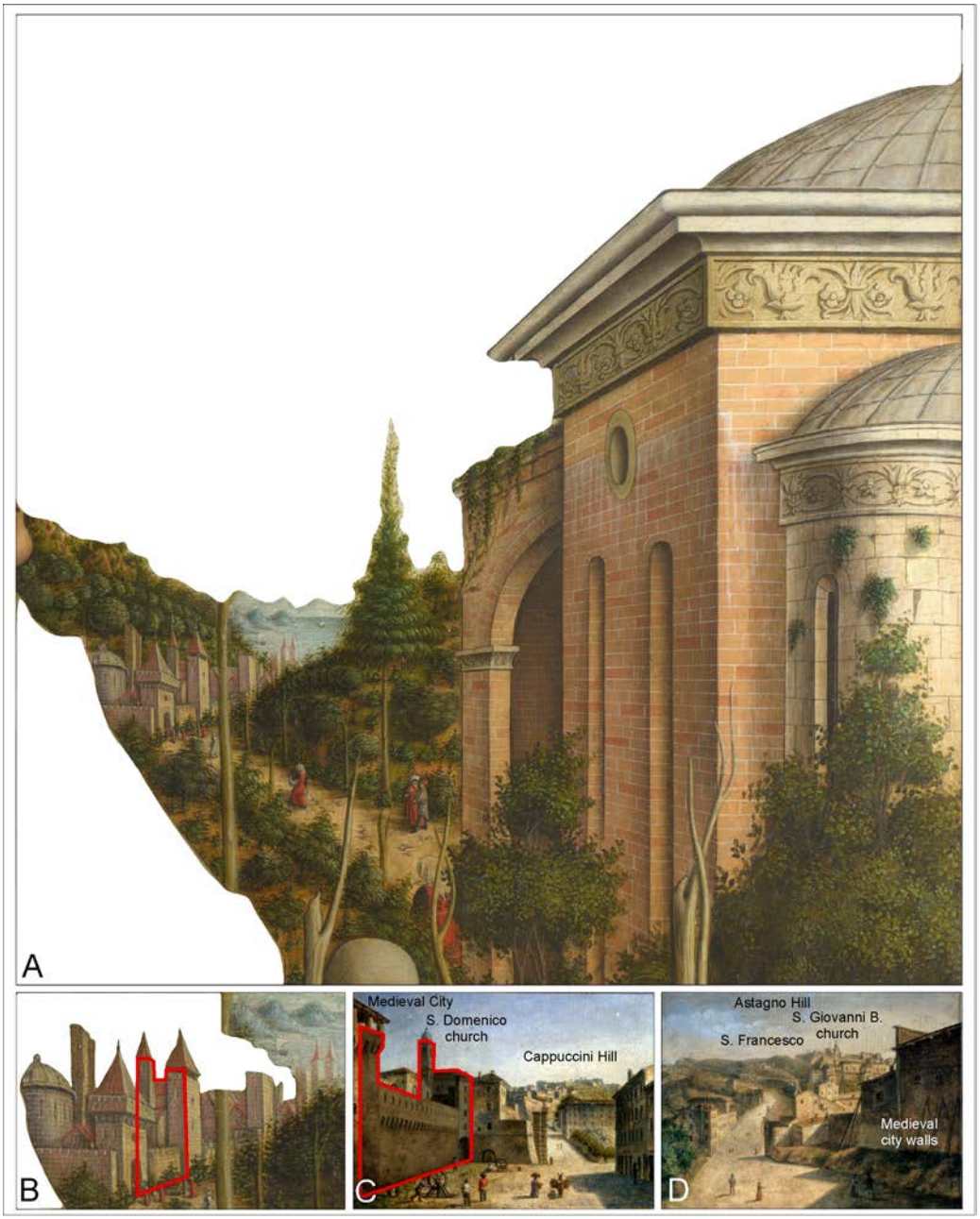

Figure 5: (A) Crop of the right side of Crivelli's painting depicting architectural and landscape details of the 15th century city of Ancona; (B) Detail of the fortified city of Ancona at the walls' eastern entrance of Porta del Calamo; (C) A realistic portrait of the no-longer existing Porta del Calamo by Barnaba Mariotti (second half of 19th century) with the Colle dei Cappuccini hill in the far distance (with permission from the Pinacoteca di Ancona); (D). Mariotti's portrait of the Colle Astagno hill as it used to be seen from the walls of Porta del Calamo.

3.3 Geological features

In order to test our hypothesis that the peculiarly pink rocks of Carlo Crivelli's painting represent the Scaglia Rossa Fm of the northeastern Apennines, we have collected and analyzed the RGB color of

polished hand samples from all the more-or-less red formations of the Umbria-Marche lithostratigraphic succession of Figure 3. The results of this analysis are shown in Table 1. Despite

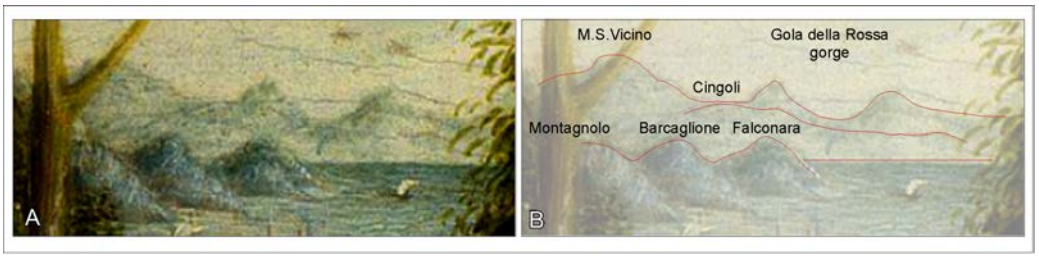

Figure 6: (A) Crop of the far background of Crivelli's painting of Beato Gabriele Ferretti; (B) Geomorphological interpretation of the hills and mountains visible from the top of the Colle Astagno hill looking WSW.

Table 1: Red rocks of the Umbria-Marche lithostratigraphic succession. Numbers in brackets in column headings refer to: [1] Adobe RGB (1998), [2] Adobe RGB (1998) to CIE L*a*b*, and [3] Adobe RGB (1998) to Munsell.

Photo (dry) (wet)	Sample	Formation	Locality	RGB [1] color value	RGB [1] color code	RGB [1] color sample	CIE L*a*b* color value [2]	Munsell color value [3]	Comparison of RGB sample with #BB7952
	LPR-RAM	Rosso Ammonitico	Scheggia	96 79 69 107 80 59	#604f45 #6b503b		35 9 11 37 14 21	4,4YR 3,5 / 2,2 5,2YR 3,6 / 3,9	
	GAT-DIA1	Diaspri	Gattuccio	112 105 89 72 64 46	#706959 #48402e		45 2 11 27 3 15	2,6Y 4,4 / 1,6 2,8Y 2,6 / 2,3	
	GAT-DIA2	Diaspri	Gattuccio	125 118 101 76 67 51	#7d7665 #4c4333		50 2 12 29 4 13	3,2Y 4,9 / 1,7 1,6Y 2,8 / 2,1	
	BTT-MAF	Marne a Fucoidi	Gubbio	39 35 34 33 25 24	#272322 #211918		12 3 2 7 6 3	4,3YR 1,1 / 0,5 1,2YR 0,7 / 1,0	
	AVA-SBW2	Scaglia Bianca	Avacelli	104 82 62 96 62 34	#68523e #603e22		37 11 19 31 19 29	6,4YR 3,7 / 3,4 5,3YR 3,0 / 5,7	
	BTT-SRR1	Scaglia Rossa	Gubbio	127 115 112 115 97 81	#7f7370 #736151		50 6 4 49 9 14	8,8R 4,9 / 1,5 6,8YR 4,2 / 2,4	
	BTT-SRR2	Scaglia Rossa	Gubbio	92 78 73 74 47 27	#5c4e49 #4a2f1b		35 8 7 22 16 23	1,6YR 3,4 / 1,6 5,8YR 2,2 / 4,7	
	BTT-SRR3	Scaglia Rossa	Gubbio	118 82 84 94 62 39	#765254 #5e3e27		40 21 8 30 18 25	3,3R 3,9 / 4,5 4,5YR 3,0 / 5,0	
	FORW-SRR3	Scaglia Rossa	Cònero	115 94 69 127 90 63	#735e45 #7f5a3f		42 9 21 43 19 26	8,4YR 4,1 / 3,4 4,3YR 4,2 / 5,2	
	BTT-SRR4	Scaglia Rossa	Gubbio	106 99 101 82 63 49	#6a6365 #523f31		43 4 0 28 11 15	7,6RP 4,2 / 0,8 5,9YR 2,8 / 2,9	
	FORW-SRR4	Scaglia Rossa	Cònero	115 103 89 124 87 61	#736759 #7c573d		45 5 11 42 19 26	9,1YR 4,4 / 1,8 4,1YR 4,1 / 5,5	
	BTT-SVA	Scaglia Variegata	Gubbio	109 101 98 57 43 27	#6d6562 #392b1b		44 4 4 18 8 17	2,5YR 4,3 / 0,8 8,5YR 1,7 / 3,0	

the very large variety of objective colors with a red component from these samples, whether as reflected from a dry or wet polished surface, once compared visually with the mean color of Crivelli's pink rocks (Figure 7), it seems that the pink color of the Paleogene R3 and R4 members of the Scaglia Rossa Fm of Monte Cònero (samples FORW-SRR3 and FORW-SRR4, respectively), provides the closest match. Nevertheless, it must be considered that with the color space CIE RGB, with 256 tonalities for each primary color, the display of a computer is able to reproduce ~16.7 million colors (*e.g.*, Peruggi 2020), each one of which is identified with a hexadecimal alphanumeric code preceded by the symbol '#' (*e.g.*, the HEX code for the color white is #ffffff). However, it must be said that Crivelli did not see and

photograph these pink rocks on polished hand samples with a digital camera but he must have seen them in natural exposures and, somewhat impressed by such an unusual pink color, he would have 'photographed' them mentally. Consequently, we toured the Umbria-Marche Apennines looking for exemplar outcrops of those more-or-less red formations, took panoramic photographs of them, and selected areas on those exposures that exhibited a reddish color typical of that formation.

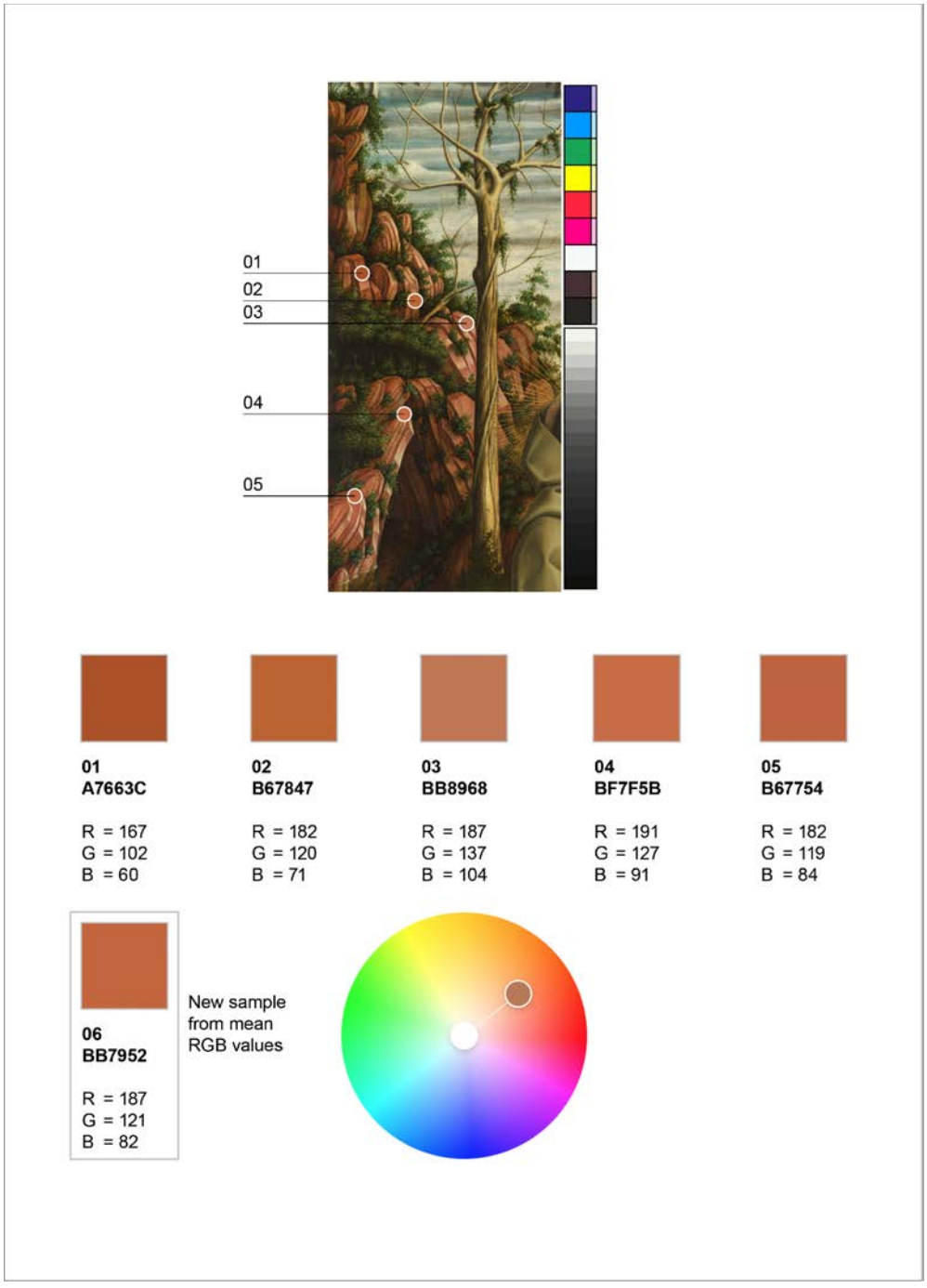

Figure 7: Synoptic figure of the RGB color values analysis of the outcrop of pink stratified rocks in Crivelli's Beato Gabriele Ferretti painting.

Starting from the oldest reddish formations of the Umbria-Marche succession, *i.e.*, Rosso Ammonitico and Diaspri, we have selected the outcrops of La Predella near Scheggia, on the right bank of the Sentino River at the foot of Monte Serrone (Baldanza *et al.* 2022), and the road outcrop of Gattuccio, near Genga (Montanari and Pignocchi 2022, p. 29), which are shown in Figures 8A and 8B, respectively. As for other Umbria-Marche formations that include reddish lithostratigraphic units, we have analyzed, using the same criterion, the spectacular exposure of the Vispi Quarry, near Gubbio (Alvarez 2019), with its thinly bedded pelagic limestones continuously covering some 50 million years of Earth's history (see Figure 3), from the Maiolica to the Scaglia Rossa formations. From this exceptional outcrop, we photo-sampled the Brown member of the Marne a Fucoidi Fm (Coccioni 2020), the W2 member of the Scaglia Bianca Fm (Coccioni and Galeotti 2003), and the basal member R1 of the Scaglia Rossa Fm (Montanari *et al.* 1989). The results are shown in synoptic Figure 9.

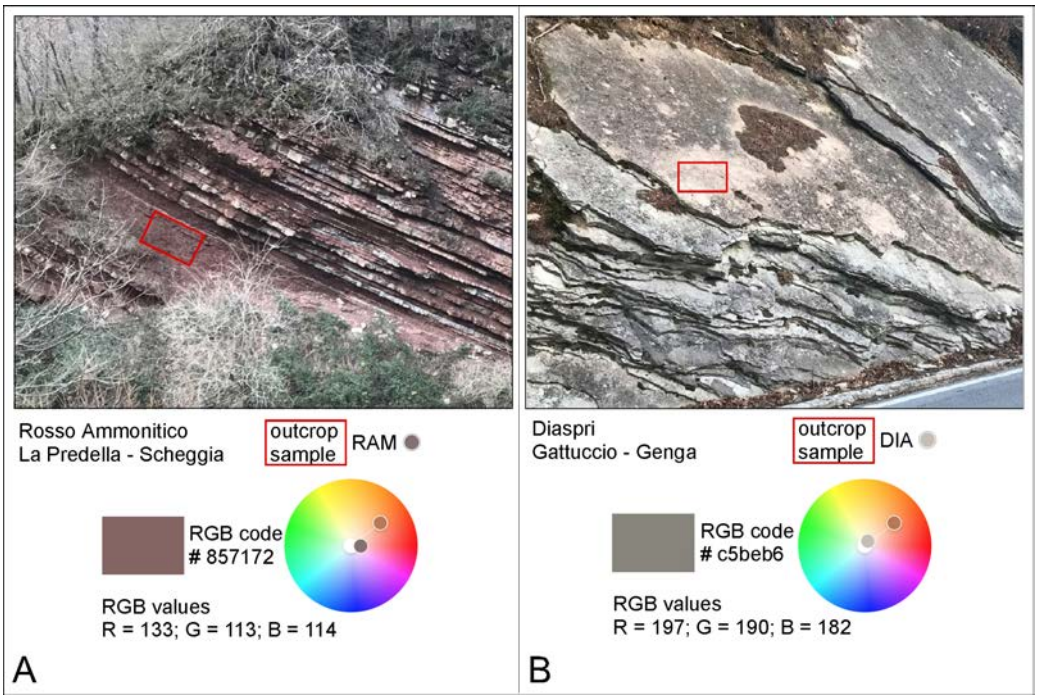

Figure 8 (A): Outcrop of the Rosso Ammonitico Fm. at La Predella, near Scheggia, exhibiting its classic Bordeaux red color identified with RGB code #857172. This lower Jurassic formation is widespread in the whole western Tethyan domain, including the pre-Alpine Venetian region where it is quarried and commercialized under the name of Marmo Rosso di Verona; (B) A layer of pinkish siliceous limestone in the otherwise greenish Diaspri Fm exposed in the Gattuccio quarries near Genga, identified with RGB code #c5beb6. These color codes are represented by a dot plotted on the wheel of colors, and therein compared with the dot that represents the mean color code #BB7952 of Crivelli's pink rocks shown in Figure 7.

As for the upper Cretaceous-lower Paleogene Scaglia Rossa Fm, which is the thickest and most widespread formation in the Umbria-Marche Apennines, we analyzed exemplar outcrops exposed along the old 340-km-long Via Flaminia, the modern state highway SS n.3. This Roman road crosses the Scheggia Pass in Umbria to enter in the Marche region, and continues northeastward across the whole NW-SE trending Umbria-Marche thrust-and-fold mountain belt eventually reaching the Adriatic coastal city of Fano, some 50 km south of the terminal city of Rimini. The first impressive exposure of the Scaglia Rossa Fm a traveler will see after the Scheggia Pass is at the Ponte a Botte bridge, which crosses the deep canyon of Fosso La Foce. There, the whole mountain on the eastern side of Via Flaminia is made up of Scaglia Rossa limestone, which contrasts with the low topography of gray

Miocene formations exposed on the hills to the west of the calcareous mountain slope (see panoramic view in Figure 10A). A photo sample of this outcrop yielded a RGB color code #62463b plotted on the respective color wheel in Figure 10A. From there, the Via Flaminia continues its northeastward route running along the Burano River, which, past the town of Cantiano, flows between hills and mountains that expose extensive outcrops of the Scaglia Rossa Fm exhibiting its most characteristic pink color. One of these exposures was sampled in the Smirra Quarry, located between the towns of Cagli and Acqualagna (Franceschi *et al.* 2015). The results of our RGB color analysis of this outcrop are reported in Figure 10B. Past Acqualagna, the Burano River merges into the Candigliano River and the Via Flaminia road is forced through the Furlo Gorge, which cuts the Monte Paganuccio Monte Pietralata anticline, the northernmost anticlinal structure of the Marche Ridge. At Furlo, the Via Flaminia is surrounded by large exposures of the Scaglia Rossa Fm (Alvarez and Lowrie 1983; Bice *et al.* 2007, Alvarez 2009, and references therein), exhibiting a facies that is characterized by white biocalcarenitic turbidites interbedded with the typically pink pelagic limestone (see panoramic view in Figure 10C). The results of our RGB color analysis of this outcrop are reported in Figure 10C.

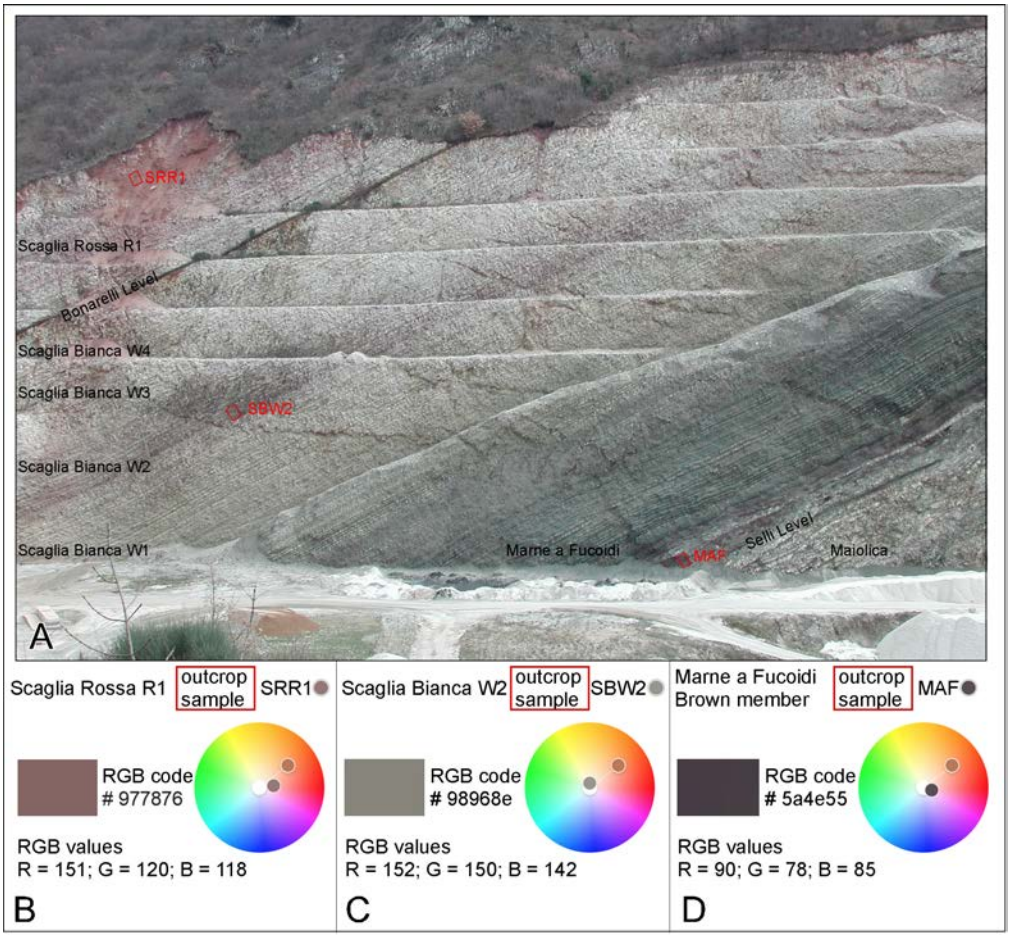

Figure 9: (A) Panoramic view of the Vispi Quarry near Gubbio with the various Umbria-Marche lithostratigraphic units from the Maiolica to the Scaglia Rossa formations; (B) RGB color values analysis results from the sampled area of the Scaglia Rossa R1 member, which yielded a #97776 color code represented by a dot plotted on the wheel of colors, and therein compared with the dot that represents the mean color code #BB7952 of Crivelli's pink rocks shown in Figure 7. (C) and D) are the RGB color values analysis from the W2 member of the Scaglia Bianca and the Brown member of the Marne a Fucoidi formations, respectively.

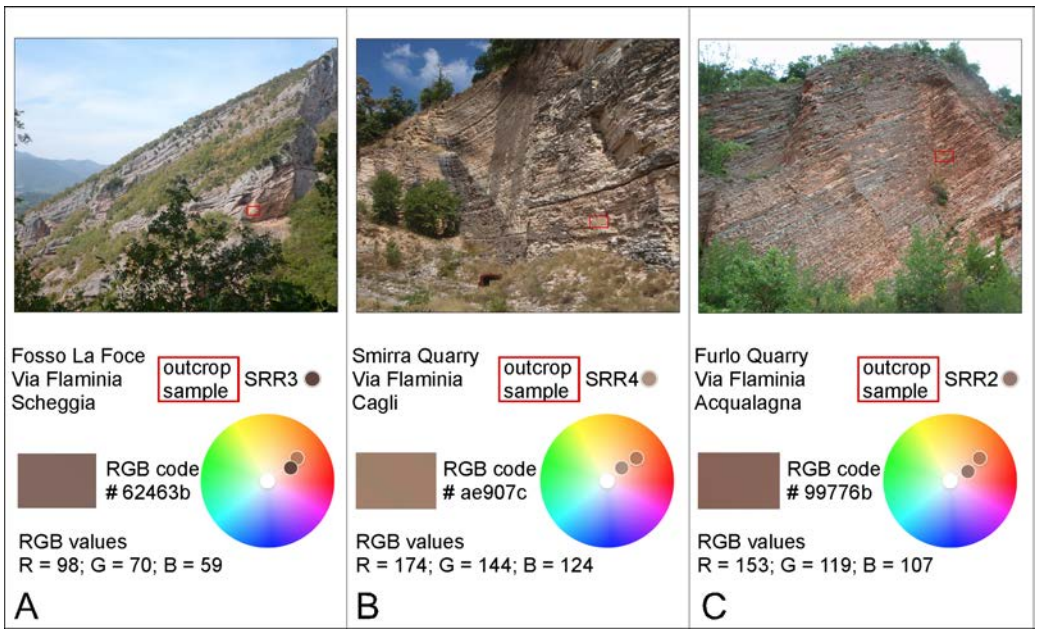

Figure 10: (A) Panoramic view of the Scaglia Rossa mountain slope as seen from the Via Flaminia near Scheggia (photo courtesy of Walter Alvarez), with the results of a RGB chromatic analysis of a sampled area indicated by a red rectangle; (B) Panoramic view of the Scaglia Rossa Fm exposed in the Smirra Quarry near Cagli, with the results of a RGB color values analysis of a sampled area indicated by a red rectangle; (C) Panoramic view of the Scaglia Rossa Fm exposed in a quarry along the Via Flaminia at Furlo, with the results of a RGB color values analysis of a sampled area indicated by a red rectangle.

During his restless young life, Carlo Crivelli never travelled across the Umbria-Marche Apennines. After leaving Venice where he served 6 months in jail following a trial for sexual abuse, he found refuge in Padua where he came in contact with the famous Paduan artist Andrea Mantegna, and other contemporary painters such as Cosmé Tura from Ferrara and, most importantly, with Giorgio Chulinovich aka 'Schiavone', a Dalmatian painter who became his best friend. In 1465, when he was 35, Crivelli migrated with his beloved friend Schiavone to Zara (today the Croatian city of Zadar; see Figure 2A for location), and eventually he crossed the Adriatic Sea to reach the Marche region where he spent the rest of his life until his death in Ascoli Piceno at age 65 (Dal Bello 2021). Therefore, Crivelli must have seen the Scaglia Rossa Fm somewhere else in the Marche region, certainly not in the Umbria-Marche anticlinorium, nor at Montagna dei Fiori, the closest Apennine mountain to Ascoli Piceno, where the Scaglia Rossa Fm actually exhibits a whitish color (Montanari *et al.* 1989; Montanari and Koeberl 2000, p. 247). The only place where Crivelli could have seen a large exposure of the typically pink Scaglia Rossa Fm is at Monte Cònero, some 8 km southeast of Ancona (Figure 11A).

One may ask: for what reason would Crivelli have gone to Monte Cònero during his stay in the convent of San Francesco ad Alto in Ancona? One plausible reason may be that at Portonovo, at the foot of Monte Cònero, which represents the easternmost blind thrust anticline of the Umbria-Marche foreland fold-and-thrust belt, there used to be an important Benedictine abbey with its 11th century Romanesque church dedicated to the Blessed Virgin Mary. The Benedictine enclave of Portonovo, despite being an isolated and difficult-to-reach coastal site with no practical communication with the hinterland, flourished for some three centuries thanks to a relatively large coastal lake of fresh water, which was fed by a copious perennial spring gushing out water from the foot of the mountain at a very short distance from the sea. In short, the coastal lake was used as a harbor (*i.e.* Novo Porto, today's Portonovo) where long distance commercial freighters and military ships could safely dock and get refurbished with uncontaminated drinking water (Montanari *et al.* 2016). And yet, in 1319 A.D., five

million cubic meters of rock catastrophically slumped down from the sheer northwestern side of Monte Cònero almost completely burying the fresh water lake and the small harbor with palisades open to the sea, but sparing the old Santa Maria church. Consequently, the surviving Benedictine monks immediately evacuated Portonovo and moved to the convent of Saint Martin in Ancona (Montanari *et al.* 2016, and references therein). After the catastrophic event, Portonovo was occasionally frequented by local fishermen, pirates, and pilgrims devoted to Saint Mary, just as Carlo Crivelli used to be. This may have motivated Crivelli's short pilgrimage to Monte Cònero, where he would have seen, for the first time, the peculiarly pink rocks of the Scaglia Rossa Fm (Figure 11A) exposed on the western mountain slope near Poggio di Ancona. From there, he could have descended down to Portonovo via a "nasty and steep little trail" (see figure 11 in Montanari *et al.* 2016). In summary, the results of our RGB chromatic analysis of the Scaglia Rossa Fm of Monte Cònero exposed at Poggio di Ancona are shown in Figures 11B, C, and D.

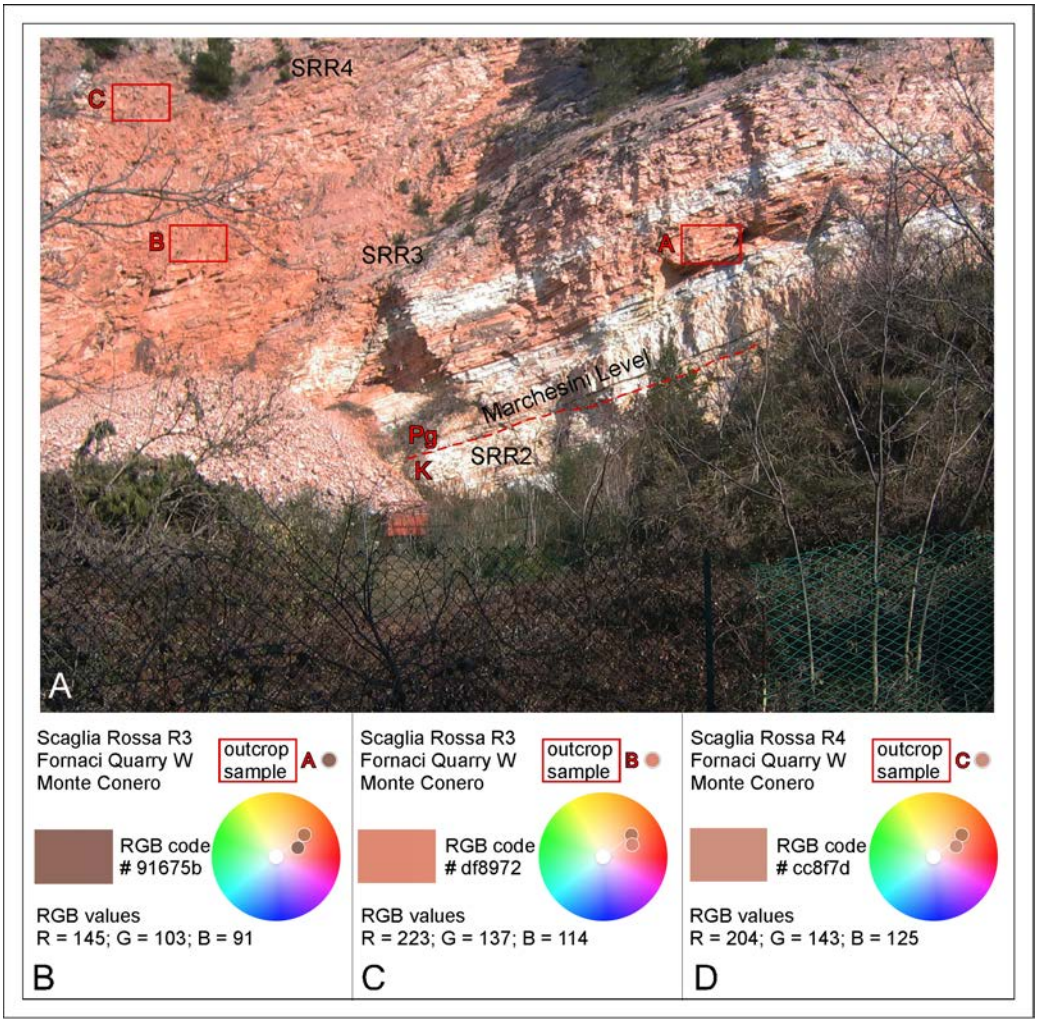

Figure 11: (A) Panoramic view of the Scaglia Rossa exposed in the disused quarry front of Fornaci, on the right side of the Betelico Creek valley near Poggio di Ancona of Monte Cònero (Burattini 2019). The results of RGB chromatic analyses of sampled areas indicated by red rectangles on the panoramic picture, are respectively reported in (B), (C), and (D). SRR2, SRR3, and SRR4 refer to the R2, R3, R4 members of the Scaglia Rossa Fm (see Figure 3). Note that the R2 member of the Scaglia Rossa at Monte Cònero exhibits a whitish color unlike in the rest of the Umbria-Marche Apennines (Montanari et al. 1989); K = Cretaceous; Pg = Paleogene. The Marchesini Level aka MegaT is a thick turbiditic calcarenite found about 80 cm above the K-Pg chronostratigraphic boundary (Montanari et al. 2016, fig. 5).

3.4. Naturalistic, Faunal, and Floral Features

Crivelli's painting of '*Blessed Gabriele Ferretti*', besides containing architectural and landscape features all referring to the city of Ancona as described above, is a collage of images that may refer to Monte Cònero (*i.e.*, the eye-catching pink rocks of the Scaglia Rossa Fm described above), and the natural environment of the outskirts of Ancona, including the nearby bay of Portonovo.

Here follows a description of the faunal and floral images of the painting. Birds: Up high roosting on a branch of a tall tree in front of the large outcrop of pink rocks, there is a European gold finch (*Carduelis carduelis*, cardellino in Italian) seen from the back, looking at the far horizon (*i.e.*, the Marche Apennine mountains as discussed above). The little bird is reproduced with formidable ornithological accuracy (Figures 12A and 12B), and was considered to have a profound symbolic significance by Renaissance painters (Anonymous 2024; Mortaruolo 2023) being a representation of the Passion of Christ. For instance, de Marchi and Mazzalupi (2008) interpreted Crivelli's gold finch roosting on a seemingly dead tree as wanting to regain life and ready to take flight toward the sky (*i.e.*, symbolic for the Resurrection of Christ). On the other hand, due to its colorful plumage (red, yellow, beige, black, and white), the gold finch was represented in naturalistic paintings and mosaics since Roman times (Figure 12C).

Figure 12: (A) The gold finch in Crivelli's painting of blessed Gabriele Ferretti; (B) A live European gold finch seen from the back; (C) A gold finch and 3 mallard ducks in a 1st century Roman floor mosaic.

In addition to the symbolic gold finch, Crivelli reproduced, with equal ornithological accuracy, a female mallard duck (*Anas platyrhinchos*) swimming with her duckling in a shallow pool of clear water (Figure 13A). In various cultures since antiquity, mallard ducks symbolized adaptability, grace, and emotional depth. The vibrant colors of the male mallard's plumage are certainly an aesthetic aspect that gratifies the birdwatcher's eye. Coincidentally, gold finch and mallards, both male and female, were pictured together in the 1st century mosaic of a Roman floor shown in Figure 12C, which was discovered in 1980 during road works under a main street in downtown Ancona. Moreover, In Christianity, the mallard duck's Spring return from migration represents spiritual renewal, rebirth, and the awakening of faith. Their annual homecoming reminds us of the resurrection and eternality of the soul (Oliver 2023).

This symbolism is interesting inasmuch as it may give significance to the flock of birds flying in formation toward the San Francesco ad Alto church in the background sky of Crivelli's painting (Figure 1). Furthermore, mallards are endemic species to the Portonovo lake (Figure 13B).

The mallard water pool in Crivelli's painting actually bears some additional geological features, which are worth mentioning. At the bottom of the pond, one can see well-rounded pebbles. Similar pebbles are also present scattered around on the rocky shore of the pond as well as on the dirt road that leads down to the medieval city of Ancona (see Figure 1). Rounded pebbles are the kind of sediment that

geologists expect to find in a fluvial deposit, certainly not at the bottom of a still water pool. And yet, there are no rivers flowing near Ancona. Therefore the pebbles in Crivelli's painting may well represent the well-rounded pebbles making up the beaches around Monte Cònero, including the popular beach of Portonovo Bay. Another geological feature visible in the left side of the painting, is a spring pouring water inside a flooded cave at the bottom of the large outcrop of pink rocks. At the bottom of the cave's lake, there are several rounded boulders, and more boulders can be seen at the bottom of a stream that disappears outside in a thicket of dark trees. If on the one hand the only important water spring we know of at Monte Cònero is the one at Portonovo (see Montanari *et al.*, 2016, figure 11, caption n. 27 "Fountain with a big Water Head which falls from above"), on the other hand there are no caves nor pink rocks over there. Nevertheless, there used to be a large, now legendary cavern open to the sea on the rocky coast a couple of kilometers to the south of the church of Santa Maria in Portonovo, known as Grotta degli Schiavi Cave (De Bosis 1861), which can only be reached from the sea. Crivelli may not have seen this sea cave but he may have heard about it, and he used his imaginary vision of it to insert it into his painting.

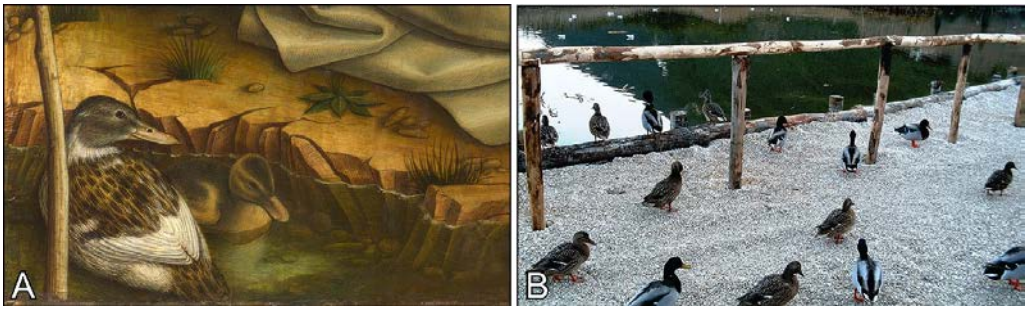

Figure 13: (A) A female mallard duck with her duckling swimming in a pond in Crivelli's painting of 'Blessed Gabriele Ferretti'; (B) Female and male mallard ducks hanging around the lake of Portonovo at the foot of Monte Cònero (Photo by Claudio Stanco, from Wikimedia Commons).

Trees: The tree that immediately gets noticed by the observer of Crivelli's painting, is a tall plant towering between the outcrop of pink rocks and the back of Blessed Gabriele (see Figure 1 for location). The long, straight trunk of the tree is wrapped by a climbing ivy, probably the common *Hedera helix*, with wisps of green leaves hanging from bare branches, (Figure 14A). The bark of the tree exhibits a gray-beige color and is scored by long furrows (see inset in Figure 14A). The branches extend radially and horizontally from a clump at the top of the trunk except for the central stalk, which extends vertically from there. These botanical features are consistent with a walnut tree (*Juglans regia*; see Figure 14B for comparison), which, in any case, is not a particularly common or characteristic plant of Ancona or Monte Cònero. On the other hand, Crivelli's walnut tree, as with the afore-discussed gold finch roosting on its branch, bears a profound symbolic meaning for the artist. In fact, this tree may recall the holy walnut tree of Saint Antony of Padua, painted by Lazzaro Bastiani around 1450 for the Franciscan church in Padua (*Catalogo Generale dei Beni Culturali* 1995), a city where Carlo Crivelli lived and worked in the Squarcione workshop until 1465 after his departure from Venice. A symbolic meaning may also be attributed to the dead, bone-dry trees, which line the dirt road that descends from the San Francesco church down to the medieval city of Ancona (see Figure 1). As suggested by Mariano (2017), they may represent common Mediterranean cypresses (*Cupressus sempervirens*) but, apart from upwards-pointing branches close to the straight trunk, there are no other botanical characteristics that can assure this classification. For certain they are all dead, whatever symbolic meaning Crivelli wanted to express. On the other hand, the tall green conifer tree on the right slope of the dirt road may represent a common white fir (*Abies alba*) whereas the roundish low trees around it, as well as the ones growing in rows on the hill slope behind the city, may represent olive trees (*Olea europea*), yet another environmental aspect of the outskirts of Ancona.

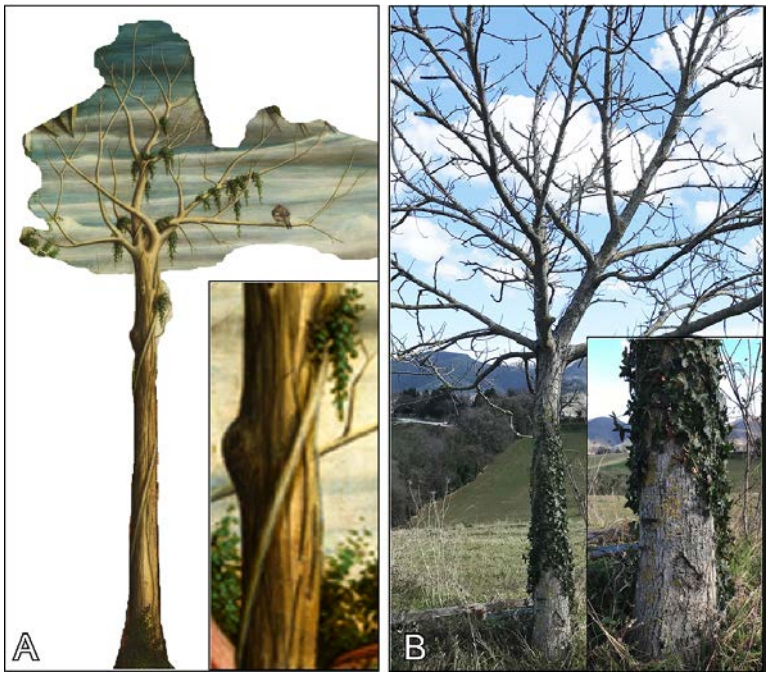

Figure 14: (A) The tall walnut tree in Crivelli's painting of Blessed Gabriele Ferretti. In the inset, a close-up image of the tree trunk wrapped by a climbing ivy; (B) A live walnut tree (Juglans regia) from a plantation in the village of Moscosi (Cingoli) with the trunk wrapped by a climbing ivy (Hedera helix).

In Crivelli's painting (Figure 1), between the outcrop of pink rocks and the shore of the pond with the ducks there is a thick forest, which separates the Cònero landscape on the left from the Ancona landscape on the right (Figure 15A). The trees may be holm oaks (*Quercus ilex*), an evergreen plant endemic to Monte Cònero (Figure 15B) and other Mediterranean forests. Finally, along the side of the San Francesco church, there are shrubs, which may represent strawberry trees (*Arbutus unedo*) (Figure 16A). This plant, called *corbezzolo* in Italian and a main component of the *macchia mediterranea* (Mediterranean scrub), is the one that gave the name to Monte Cònero. In fact, the word Cònero derives from the old Greek word κομαροσ (pronounced kòmaros). This evergreen plant, which produces bright red lychee-like fruits in late autumn, besides its symbolic significance of eternal life and hospitality, is still used today as a gardening decorative plant all over the world but grows spontaneously everywhere in the holm oak forests of Monte Cònero (Figure 16B).

Figure 15: (A) The dark thicket of trees at the foot of the pink rocks in Crivelli's painting of 'Blessed Gabriele Ferretti'; (B) A thicket of holm oaks (Quercus ilex) near the lake of Portonovo at the foot of Monte Cònero.

Grasses: Sparse on the rocky floor surrounding the pond in Crivelli's painting, there are numerous tufts of grass exhibiting different foliage. However, it must be said that in this case

Figure 16: (A) Shrubs along the side of the San Francesco ad Alto church in Clivelli's painting of 'Blessed Gabriele Ferretti'; (B) Strawberry tree shrubs (Arbutus nuedo) in the parking lot near the lake of Portonovo at the foot of Monte Cònero.

Crivelli did not manifest the same remarkable scientific accuracy he used in portraying the gold finch and the mallard ducks described above. Nevertheless, these botanical features may also refer to the environment surrounding the lake of Portonovo. This brackish lake is today surrounded by, and partially engulfed with, common swamp reeds (*e.g.*, *Phragmites cf. australis*) but also rare spiny rushes such as *Juncus acutus*, a plant particularly adapted to saline environments (*e.g.*, Montanari *et al.* 2021, p. 4 and references therein). Such a widespread profusion of swamp reeds is actually absent in Crivelli's painting. Instead, the sparse tufts of reed plants on the rocky surrounding of the pond (Figure 17A1) may represent *Calamagrotis cf. acutiflora*, a common plant growing in the holm oak and strawberry tree underbrush of Portonovo (Figure 17A2). Yet, this plant also grows on dry, soil-less rocky surfaces (Figure 17A3), such as the probable desolate landscape of Portonovo after the catastrophic landslide of 1319 A.D. (Montanari *et al.* 2016).

A small leafed grass growing on bare rock (Figure 17B1) in Crivelli's painting, may represent a typical plant of the rocky Riviera of Monte Cònero known locally as '*paccasassi*' (meaning rock splitter in local dialect), which represents the edible marine fennel (*Crithmum maritimum*; Figure 17B2). This species is the terrestrial plant that grows nearest to the sea in a rocky supralittoral zone (*e.g.*, figure 5 in Montanari *et al.* 2019). On the other hand, a grass resembling an edible sow-thistle in Crivelli's painting, which is characterized by pinnate leaves (Figure 17C1), probably represents the common and widespread *Sonchus oleraceus* locally known as '*crispigna*' (Figure 17C2). Finally, a star-shaped, flat-on-the-ground plant characterized by oblong-attenuated basal leaves, which Crivelli placed below his signature (Figure 17D1), may bear a symbolic significance. The same kind of basal rosetta-leafed plant in Crivelli's painting have sprouts of tiny purple flowers (Figure 17D2). This plant may represent an orchid similar to *Orchis cf. simian* (Figure 17D3), a common spontaneous orchid of Monte Cònero.

Figure 17: (A1) Turfs of reed grass in Crivelli's painting Beato Gabriele Ferretti; (A2) Turfs of reed grass Calamagrotis cf. acutiflora in the underbrush of the strawberry tree and holm oak forest at Portonovo of Monte Cònero; (A3) Turfs of reed grass growing on an outcrop of Scaglia Variegata marly limestone;(B1) Small leafed grass, probably Crithmum maritimum, aka sea fennel, in Crivelli's painting of 'Blessed Gabriele Ferretti'; (B2) Crithmum maritimum of Monte Cònero also known as 'paccasassi' in local dialect, which means rock splitter in English; (C1) A grass resembling a sow-thistle (Sonchus oleraceus) grass in Crivelli's painting of 'Blessed Gabriele Ferretti'; (C2) Sonchus oleraceus of Monte Cònero locally known as 'crispigna'; (D1) A star-shaped, flat-on-the-ground plant in Crivelli's painting of 'Blessed Gabriele Ferretti' characterized by oblong-attenuated basal leaves; (D2) The same kind of leafed plant in Crivelli's painting but with a sprout of tiny purple flowers; (D3) Orchis simian, a common spontaneous orchid of Monte Cònero.

IV. THE LANDSCAPE AND GEOLOGY IN 15TH CENTURY RENAISSANCE PAINTINGS

The landscape, as no longer a secondary element in pictorial art, starts to have a relevant role in 15th century Flemish paintings where it is often represented realistically with great attention but always as the background of human figures and architectural features. In Florence in the 1400s, concurrently with the study of, and great attention to the perspective, the landscape, while depicted with precision, still constituted the prospective plan of a painting in which figures, architecture, and events are the protagonists of the foreground in the center of the pictorial composition.

Absolutely innovative are the portraits of the Dukes of Urbino by Piero della Francesca (1473–1475), in which the landscape in the background, in addition to giving prominence to the imposing portraits of the Duke and Duchess, represented a precise territorial context. In this masterpiece, the landscape acquired an extraordinary uniqueness rich in details, with panoramic as well as naturalistic glimpses eventually touching topographic perfection. Borchia and Nesci (2012) were able to demonstrate the perfect resemblance with some specific features of the Montefeltro landscape (*i.e.*, the Apennine region in the northern Marche under the domain of the Duke of Urbino), today partially modified and reshaped after successive geomorphological events. Thus, it is no longer an ideal landscape put there as a symbolic or simple wing of a theater stage but a realistic landscape.

In the same way, in the paintings of Antonio del Pollaiolo (1433–1498) emerged an initial interest for the realistic representation of the Tuscan and the Arno River valley landscapes, which were observed and reproduced with Flemish expertise, and with evident references to the scientific naturalism from the canonical paintings of Leon Battista Alberti, particularly his architectural treatise *De re aedificatoria* (1443–1452), first printed in Florence in 1485.

Some Venetian artists between the end of the 1400s and the beginning of the 1500s also inserted realistic landscapes in their paintings but no longer relegated to the background or as a simple supporting actor of the protagonist human figure and the actions of mythological or Renaissance men but as an element gifted with autonomous life. In the Venetian region, this new spatiality is evident in the paintings of Andrea Mantegna, probably influenced by Leon Battista Alberti, and his brother-in-law Giovanni Bellini, as one can see in his two versions of *Orazione nell'Orto* (1455 and 1459, respectively), which are on display next to each other in the National Gallery of London.

This innovative pictorial process culminated with Leonardo da Vinci, who thanks to the combination of his extraordinary artistic talent and his immense scientific knowledge, instilled in the landscape a new dimension rightly admired for the meticulous depiction of reality and for the attention to the multiple and changing aspects of nature, including geological and hydrological phenomena.

Only these few painters, like Mantegna and above all Leonardo, had the ability to faithfully paint the geology of a territory, long before Ulisse Aldrovandi from Bologna coined the term *Geologia* in 1603, and Niccolò Stenone (aka Steno), enunciated the fundamental laws of stratigraphy in the second half of the 17th century, (Coccioni 2019; Sdao 2021; Vai 2003, 2021).

In his architectural treatise, Leon Battista Alberti mentioned the various lithologies normally used in building construction, which he simply called '*pietre*' (*i.e.*, stones) stating that he did not want to talk at length about these stones and take a position about the various theories proposed in the past on the '*origini delle pietre*' (the origins of the stones). Nevertheless, he briefly discussed the possible processes that could occur during the diagenesis of once loose sediments ". . . *que' principii viscosi per la commistione dell'acqua, e della terra, prima in fango, dipoi in pietra s'induriscono*" (. . . which at first viscous due to the mixing with water and dirt, first as mud and then in stone they become hard) (Romano 2019).

Leonardo's *Vergine delle Rocce* (1483–1486), amazes the viewer with the precision and accuracy with which the artist represents complex rock formations to be the setting of his pictorial composition. In the famous painting *Cristo Morto* by Mantegna (*circa* 1470–1483), art students tried to give a name to the unction stone, which is identified as two sedimentary carbonate rocks, *i.e.*, the pink stone from the Lessini Mountains (near Padua) or the pink 'marble' of Asiago (northern Venetian region), whereas in the painting *Madonna delle Cave*, Andrea Mantegna actually illustrated the quarrying operation of these building stones (Conti 2021; Vai 2009).

V. CONCLUSIONS

A close analysis of Carlo Crivelli's painting, which portrays the central subject of a blessed Friar Gabriele Ferretti praying in ecstasy at the miraculous apparition of the Virgin Mary on the Colle Astagno hill of Ancona (Marche region of central-eastern Italy), reveals to us that most of the various particular details making up the background of this painting, refer to architectural, scenic, and environmental features of the medieval city of Ancona, where the artist actually made this masterpiece around 1489, and the nearby Monte Cònero, also known as Il Monte di Ancona. The panoramic scenery

of the far background is undoubtedly that of the Adriatic gulf of Ancona surrounded by coastal hills, while a view of the Apennine Mountains in the distance would be the first iconographic representation of the central Marche Ridge. On the other hand, a large outcrop of thinly bedded rocks exhibiting an unusual pink color, is chromatically consistent with the upper Cretaceous-lower Paleogene pelagic limestone of the Scaglia Rossa Fm, the most widespread geological formation exposed throughout the Umbria-Marche Apennines. Considering the geographic and environmental context of Crivelli's painting, we deduce that Crivelli's pink rocks represent the Scaglia Rossa Fm exposed on the western slope of Monte Cònero, whereas various faunal and floral details surrounding these rocks refer to the Portonovo Bay, at the northern foot of the northwest-facing slope of Monte Cònero. This would be the first iconographic representation of the Scaglia Rossa Formation.

In conclusion, the pink rocks of Carlo Crivelli represent the Scaglia Rossa pelagic limestone, which today is famous worldwide in the Earth sciences community for the innumerable pioneering studies dealing with major events that punctuated the history of Earth leading to sensational discoveries and discontinuities in scientific thinking. In fact, it is the Scaglia Rossa Fm that provided the basis for the first direct correlation of the upper Cretaceous-lower Paleogene magnetostratigraphy with the biostratigraphic time scale, thereby permitting a precise estimate of the age of the Marine Magnetic Anomalies and oceanic seafloor spreading rates (Alvarez *et al.* 1977; Lowrie 2016). Moreover, the Scaglia Rossa Fm bears the record of a major Cretaceous anoxic event expressed by the Bonarelli Level (see Alvarez and Sannipoli 2016; Batenburg *et al.* 2016, and references therein), which represents the much-debated global Oceanic Anoxic Event 2 (OAE-2). The Scaglia Rossa Fm also contains the striking Cretaceous-Paleogene (K-Pg) boundary event including the first evidence for a global mass extinction caused by a catastrophic extraterrestrial impact (Alvarez *et al.* 1980; Montanari *et al.* 1983; Montanari and Coccioni 2019, and references therein), and the hyperthermal events of the Eocene Epoch (*e.g.*, Coccioni *et al.* 2016). Ultimately, this amazing formation allowed the calibration of portions of the astrochronological time scale via multiproxy cyclostratigraphic analysis (Franceschi *et al.* 2015; Sinnesael *et al.* 2016; Coccioni *et al.* 2022; Gale *et al.* 2023). And Carlo Crivelli was the first to notice such an attractive pink rock, which was destined to become a major protagonist in Earth Sciences history.

ACKNOWLEDGEMENTS

This research was financially supported by the non-profit Association "Le Montagne di San Francesco" (www.coldigioco.org). We would like to thank Dr Nathan Church (Norwegian University of Science and Technology) who first brought to our attention Crivelli's painting that he serendipitously saw in the National Gallery of London, and for proof-reading the first draft of this paper. A special thanks goes to Ten. Col. Emanuele Vergine, Infrastructure Manager of the military presidium of Ancona, for kindly having accompanied us in a surveying tour of the former San Francesco ad Alto convent. We would like to thank artist and art historian Paula Metallo (www.paulametallo.com) for helping us in the study of Crivelli's self portraits. A special thank goes to Editor John Diemer, for accepting our manuscript for publication in *Earth Sciences History*, pending minor revisions, Prof Gian Battista Vai (University of Bologna) for his constructive yet positive review of the original manuscript, and an anonymous second reviewer for interesting comments about some Renaissance humanistic aspects of our scientific research work. Last but not least, we would like to thank Dr Viviana Caravaggi Vivian and Dr Roberto Barbini from the civic gallery Pinacoteca of Ancona for granting us the permission to reproduce images of Barnaba Mariotti's paintings of Porta del Calamo, and the National Gallery of London for granting us the permission to reproduce the image of Crivelli's painting '*The Vision of the Blessed Gabriele*'.

REFERENCES

1. Albertini, Camillo. 1824. Storia d'Ancona dal 1400 al 1480. Luciano Benincasa, Municipal library of Ancona, 22 libri mss.
2. Alvarez, Walter. 2009. *The Mountains of Saint Francis*. New York: W. W. Norton, 304 pp. Alvarez, Walter. 2019. A review of the Earth history record in the Cretaceous, Paleogene, and Neogene pelagic carbonates of the Umbria-Marche Apennines (Italy): Twenty years of the Geological Observatory of Coldigioco. In: *250 Million Years of Earth History in Central Italy: Celebrating 25 years of the Geological Observatory of Coldigioco*, edited by C. Koeberl, and D. M. Bice, 1–58. Geological Society of America Special Paper 542.
3. Alvarez, Walter, and Sannipoli, Ettore. 2016. Guido Bonarelli and the geological discovery of the Bottaccione Gorge at Gubbio. In: *The Stratigraphic Record of Gubbio*, edited by M. Menichetti, R. Coccioni, and A. Montanari, 1–11. Geological Society of America Special Paper 524.
4. Alvarez, Walter, *et al.* 1977. Upper Cretaceous–Paleocene magnetic stratigraphy at Gubbio, Italy; V. Type section for the Late Cretaceous– Paleocene geomagnetic reversal time scale. *Geological Society of America Bulletin* 88: 383–389.
5. Alvarez, Luis Walter, Alvarez, Walter, Asaro, Frank, and Michel, Helen. 1980. Extraterrestrial cause for the Cretaceous-Tertiary extinction. *Science* 208: 1095–1108.
6. Anonymous. 2024. Uccelluzzi o cardellini? digilander.libero.it/cardellini1/Ita/cardellino2.htm. Alvarez, Walter, and Lowrie, William. 1984. Magnetic stratigraphy applied to synsedimentary slumps, turbidites, and basin analysis: The Scaglia limestone at Furlo (Italy). *Geological Society of America Bulletin* 95: 324–336.
7. Baldanza, Angela, *et al.* 2022. The Jurassic structural high of Sasso di Pale (Umbria-Marche Basin, Italy): How a small Apennine structure recorded Early to Middle Jurassic global perturbations. In: *From the Guajira Desert to the Apennines, and from Mediterranean Microplates to the Mexican Killer Asteroid: Honoring the Career of Walter Alvarez*, edited by C. Koeberl, P. Claeys, and A. Montanari, 267–309. Geological Society of America Special Paper 557.
8. Battenburg, Sietske, J. *et al.* 2016, Orbital control on the timing of oceanic anoxia in the Late Cretaceous. *Climate of the Past* 12: 1995–2009.
9. Beni Culturali. 1995. Sant'Antonio da Padova sulnoce e Santi. http://catalogo.beniculturali.it/detail/HistoricOrArtisticProperty/0500402380.
10. Bernabei, Lazzaro. 1497. Croniche Anconitane transcription et insieme reducte per me Lazzaro. de'Bernabei Anconitano, Manuscript in Luciano Benincasa municipal library of Ancona, n. 235, ff.102v 103r.
11. Bice, David M., Montanari, Alessandro, and Rusciadelli, Giovanni. 2007. Earthquake-induced turbidites triggered by sea level oscillations in the Upper Cretaceous of Italy. *Terra Nova* 18: 387–392. Borchia, Rosetta, and Nesci, Olivia. 2012. *The Invisible Landscape*. Ancona: Il Lavoro Editoriale Ed. Burattini, Francesco. 2019. I sentieri del lavoro e del piacere. Guida escursionistica al Parco del Conero con carta escursionistica e carta panoramica allegate. Author published, Grafiche Ricciarelli di Monsano (AN). 437 pp.
12. Casalini, Primo. 2004. Il polittico di Sant'Emidio. Arengario. http://arengario.net/momenti/momenti51.html Coccioni, Rodolfo. 2019. *Leonardo da Vinci: Rocce, fossili e altre simili cose*. Aras Edizioni, 241 pp. Coccioni, Rodolfo. 2020. Revised upper-Barremian-upper Aptian planktonic foraminiferal biostratigraphy of the Gorgo a Cerbara section (central Italy). *Newsletter on Stratigraphy* 53/3: 275–295. DOI: 10.1127/nos/2019/0539.
13. Coccioni, Rodolfo, and Galeotti, Simone. 2003. The mid-Cenomanian event; prelude to OAE 2. *Palaeogeography, Palaeoclimatology, Palaeoecology* 190: 427–440.
14. Coccioni, Rodolfo, *et al.* 2016. An integrated stratigraphic record of the Palaeocene–lower Eocene at Gubbio (Italy): New insights into the early Palaeogene hyperthermals and carbon isotope excursions. *Terra Nova* 24: 380–386.

15. Coccioni, Rodolfo, *et al.* 2022. Integrated stratigraphy of the Lutetian-Priabonian pelagic section at Bottaccione (Gubbio, central Italy): A proposal for defining and positioning the Global Stratotype Section and Point (GSSP) for the base of the Bartonian Stage (Paleogene System, Eocene Series). In: *From the Guajira Desert to the Apennines, and from Mediterranean Microplates to the Mexican Killer Asteroid: Honoring the Career of Walter Alvarez*, edited by C. Koeberl, P. Claeys, and A. Montanari, A., 311–346. Geological Society of America Special Paper 557.
16. Cogliandro, Fabiola, and Tittarelli, Marco. 2019. Insiedamenti Francescani ad Ancona. La chiesa di San Francesco ad Alto. In: *Atti del Convegno Internazionale (10-11 may 2021)*. Roma: Sapienza Università Editrice.
17. Conti, Silvia. 2021. Quella passione del Mantegna per la geologia. Artribune https://www.artribune.com/arti-visive/archeologia-arte-antica/2021/05/andrea-mantegna-geologia/ Dal Bello, Mario. 2021. Crivelli torna a splendere. Città Nuova. Cultura e informazione, October 12, 2021. Città Nuova (cittanuova.it).
18. De Bosis, Francesco. 1861. La Grotta degli Schiavi. *Società Italiana di Scienze Naturali* 3: 1–6. De Marchi, Andrea, and Mazzalupi, Matteo. 2008. *Pittori ad Ancona nel Quattrocento*. Federico Motta editore. ISBN 978-88-7179607-9 (p. 304).
19. Ferretti, Lando. 1580. Historia d'Ancona. Manuscript, Luciano Benincasa municipal library of Ancona.
20. Franceschi, Marco, *et al.* 2015. Terrestrial Laser Scanner imaging for the cyclostratigraphy and astronomical tuning of the Ypresian–Lutetian pelagic section of Smirra (Umbria–Marche Basin, Italy). *Palaeogeography, Palaeoclimatology, Palaeoecology* 440: 33–46.
21. Gale, Andy, *et al.* 2023. The Global Boundary Stratotype Section and Point (GSSP) of the Campanian Stage at Bottaccione (Gubbio, Italy) and its auxiliary sections: Seaford Head (UK), Bocieniec (Poland), Postalm (Austria), Smoky Hill, Kansas (U.S.A), Tepayac (Mexico). *Episodes* 46: 451–490.
22. Gasparini, Carlo. 1648. Le Glorie Francescane nell'Ill.ma Provincia del Piceno, In variati Capitoli distinte, e poste, da Me fra Carlo Gasparini, uno dei suoi Figli. Manuscript, Biblioteca Comunale, Ancona. Gonzaga, Francesco. 1587. De origine seraphicae religionis Franciscanae, eiusque progressibus, de regularis observantiae institutione, forma administration, ac legibus, admirabilique eius propagazione. Ex Typographia Dominici Basae, Roma.
23. Lowrie, William. 2016. A history of paleomagnetic investigations in the Umbria-Marche Apennines. In: *The Stratigraphic Record of Gubbio*, edited by M. Menichetti, R. Coccioni, and A. Montanari, 19–33. Geological Society of America Special Paper 524.
24. Mariano, Fabio. 2017. *Il complesso di San Francesco ad Alto a Capodimonte. Storia, architettura, restauri del primo insediamento francescano in Ancona*. Fermo: Andrea Livi Ed. 64 pp.
25. Montanari, Alessandro, Chan, Lung San, and Alvarez, Walter. 1989. Synsedimentary tectonics in the Late Cretaceous-Early Tertiary pelagic basin of the Northern Apennines. In: *Controls on Carbonate Platforms and Basin Development*, edited by P. Crevello, J. L. Wilson, R. Sarg, and F. Reed, 379–399. SEPM Special Publication 44.
26. Montanari, Alessandro, and Coccioni, Rodolfo. 2019. The serendipitous discovery of an extraterrestrial iridium anomaly at the Cretaceous-Palaeogene boundary in Gubbio and the rise of a far-reaching theory. *Bollettino della Società Paleontologica Italiana* 58: 77–83.
27. Montanari, Alessandro, *et al.* 1983. Spheroids at the Cretaceous-Tertiary boundary are altered impact droplets of basaltic composition. *Geology*: 11 668–671.
28. Montanari, Alessandro, *et al.* 2019. Pelagosite revisited: The origin and significance of a laminated aragonitic encrustation of Mediterranean supralittoral rocks. In: *250 Million Years of Earth History in Central Italy: Celebrating 25 Years of the Geological Observatory of Coldigioco*, edited by C. Koeberl, and D. M. Bice, 501–532. Geological Society of America Special Paper 542.

29. Montanari, Alessandro, *et al*. 2021. Stygobitic crustaceans in an anchialine cave with an archeological heritage at Vodeni Rat (Island of Sveti Klement, Hvar, Croatia). *International Journal of Speleology* 50: 1–14.
30. Montanari, Alessandro, and Koeberl, Christian. 2000. *Impact Stratigraphy: The Italian Record. Lecture Notes in Earth Sciences*. Springer, 364 pp.
31. Montanari, Alessandro, Mainiero, Maurizio, Coccioni, Rodolfo, and Pignocchi, Gaia. 2016. Catastrophic landslide of Medieval Portonovo (Ancona, Italy). *Geological Society of America Bulletin* 118: 1660– 1678.
32. Montanari, Alessandro, and Pignocchi, Gaia. 2022. *Frasassi: La Piccola Grande Storia delle Grotte*. E Book, Federazione Speleologica Marchigiana Ed. www.speleomarche.it.
33. Mortaruolo, Ivano. 2023. La rondine, il cardellino e il rigogolo nelle opere del pittore Carlo Crivelli (1430/35-1494/95). *Italia Ornitologica, F.O.I. Onlus* 3: 23–28.
34. Oliver. 2023. *The Spiritual Symbolism and Meaning of Mallard Ducks. Sacred Symbo*. https://sacredsymbo.com/spiritual-meaning/mallard-ducks
35. Peers, C. R. 2005. *The Early Italian Painters*. White Fish, USA: Kessinger Publishing, 272 pp. Peruggi, Fulvio. 2020. Fisica della Visione, Lezione 17. Università degli Studi di Napoli Federico II. http://www.docenti.unina.it/webdocenti-be/allegati/materiale-didattico/34241541. Regione Marche. 2003. Carta Geologica Progetto "Unico Territoriale Geologico" 1:10,000: Centro Cartografico Regione Marche, scale 1:10,000, http://www.ambiente.marche.it/ <territorio> (accessed 2023).
36. Romano, Marco. 2019. "L'uomo universale del primo Rinascimento": la geologia nel De re aedificatoria di Leon Battista Alberti. *Rendiconti Online della Società Geolologica Italiana* 47: 185–201. https://doi.org/10.3301/ROL.2018.72
37. Sdao, Francesco. 2021. Leonardo da Vinci nel V centenario della morte. https//iris.unibas.it/retrieve/dd9e0b51-79a5-1e84-e053-3a05fe0aa940/Leonardo_Geologia.pdf Sinnesael, Matthias, *et al*. 2016. High-resolution multiproxy cyclostratigraphic analysis of environmental and climatic events across the Cretaceous-Paleogene boundary in the classic pelagic succession of Gubbio (Italy). In: *The Stratigraphic Record of Gubbio: Integrated Stratigraphy of the Late Cretaceous–Paleogene Umbria-Marche Pelagic Basin*, edited by M. Menichetti, R. Coccioni, and A. Montanari, 115– 137. Geological Society of America Special Paper 524.
38. Talamonti, Antonio. 1936. Cronistoria dei frati Minori della Provincia Lauretana delle Marche, II, Sassoferrato 1939, pp. 27–108.
39. Vai, Gian Battista. 2009. The Scientific Revolution and Nicholas Steno's twofold conversion. In: *The Revolution in Geology from the Renaissance to the Enlightenment*, edited by G. D. Rosenberg, 187– 208. Geological Society of America Memoir 203.
40. Vai, Gian Battista. 2021. Leonardo da Vinci's and Nicolaus Steno's geology. *Earth Sciences History* 40(2): 293–331.
41. Vai, Gian Battista. 2003. Aldrovandi's will introducing the term 'Geology' in 1603. In: *Four Centuries of the Word Geology: Ulisse Aldrovandi 1603 in Bologna*, edited by G. B. Vai and W. Cavazza, 65– 111. Bologna: Minerva Edizioni.

Does SuperKamiokande Observe Levy Flights of Solar Neutrinos?

Arak M. Mathai & Hans J. Haubold

McGill University

ABSTRACT

The paper is utilizing data from the SuperKamiokande solar neutrino detection experiment and analyses them by diffusion entropy analysis and standard deviation analysis to evaluate the scaling exponent of the probability density function. The result of the analysis indicates that solar neutrinos are subject to Levy flights. The paper derives the probability density function and the governing fractional dif fusion equation for solar neutrino Levy flights in terms of Fox's H-function. The conclusion of the paper is the question: Does Super Kamiokande Observe Levy Flights of Solar Neutrinos?.

Keywords: solar neutrinos, SuperKamiokande experiment data, diffusion entropy analysis, standard deviation analysis, scaling exponent, neutrino probability density function, Fox H-function, fractional diffusion equation, Levy flights.

Classification: LCC Code: QC793.5.N42, QC806, QA273

Language: English

Great Britain Journals Press

LJP Copyright ID: 925604
Print ISSN: 2631-8490
Online ISSN: 2631-8504

London Journal of Research in Science: Natural & Formal

Volume 26 | Issue 1 | Compilation 1.0

Does SuperKamiokande Observe Levy Flights of Solar Neutrinos?

Arak M. Mathai & Hans J. Haubold

ABSTRACT

The paper is utilizing data from the SuperKamiokande solar neutrino detection experiment and analyses them by diffusion entropy analysis and standard deviation analysis to evaluate the scaling exponent of the probability density function. The result of the analysis indicates that solar neutrinos are subject to Levy flights. The paper derives the probability density function and the governing fractional dif fusion equation for solar neutrino Levy flights in terms of Fox's H-function. The conclusion of the paper is the question: Does Super Kamiokande Observe Levy Flights of Solar Neutrinos?

Keywords: solar neutrinos, SuperKamiokande experiment data, diffusion entropy analysis, standard deviation analysis, scaling exponent, neutrino probability density function, Fox H-function, fractional diffusion equation, Levy flights.

Author: Department of Mathematics and Statistics McGill University, Montreal, Canada.
Office for Outer Space Affairs, United Nations, Vienna International Centre, Vienna, Austria.

I. SOLAR NEUTRINOS: SUPERKAMIOKANDE DATA

Over the past 50 years, radio-chemical and real-time solar neutrino experiments have proven to be sensitive tools to test both astrophysical and elementary particle physics models and principles (Sakurai, 2018; Orebi Gann et al., 2021). Solar neutrino detectors (radio-chemical: Homestake, GALLEX + GNO, SAGE, real-time: SuperKamiokande, SNO, Borexino) have demonstrated that the Sun is powered by thermonuclear fusion reactions. Today fluxes, particularly from the pp-chain have been measured: pp. ^7Be, pep, ^8B, and, hep. Experiments with solar neutrinos and reactor anti-neutrinos (KamLAND) have confirmed that solar neutrinos undergo flavor oscillations (Mikheyev-Smirnov-Wolfenstein (MSW) model). Results from solar neutrino experiments are consistent with the Mikheyev-Smirnov-Wolfenstein Large Mixing Angle (MSW-LMA) model, which predicts a transition from vacuum-dominated to matter-enhanced oscillations, resulting in an energy dependent electron neutrino survival probability.

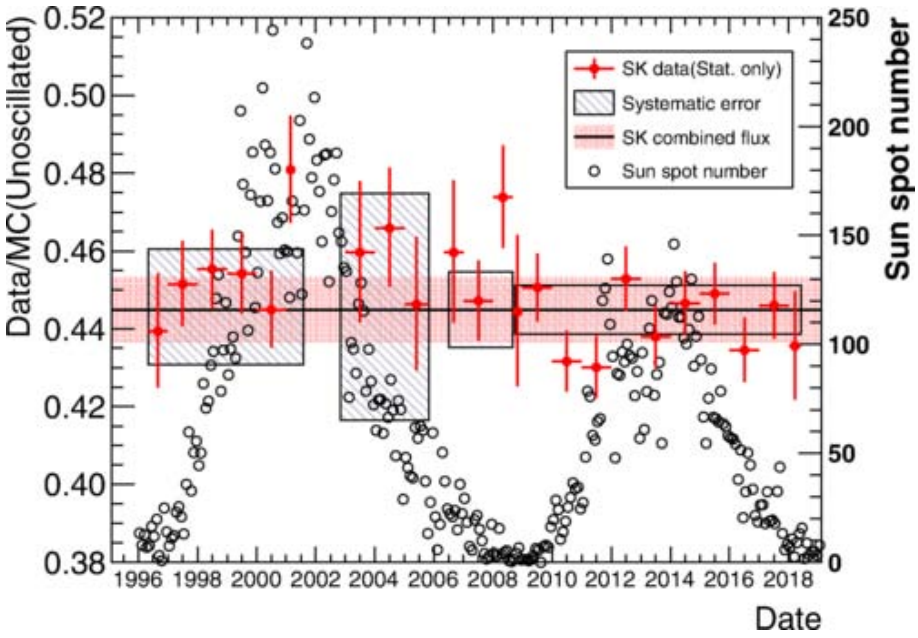

Figure 1: Yearly solar neutrino fux measured by SuperKamiokande. The redflled circle points show the SuperKamiokande data with statistical uncertainty and the gray striped area show the systematic uncertainty for each phase. The horizontal black solid line (red shaded area) shows the combined value of measured flux (its combined uncertainty). The black-blank circle points show the sunspot numbers from 1996 to 2018 (Abe et al., 2024)

II. DIFFUSION ENTROPY AND STANDARD DEVIATION: ANALYSIS

For all radio-chemical and real-time solar neutrino experiments, periodic variation in the detected solar neutrino fluxes have been reported, based mainly on Fourier and wavelet analysis methods (standard deviation analysis). Other attempts to analyze the same data sets, particularly undertaken by the experimental collaborations of real-time solar neutrino experiments themselves, have failed to find evidence for such variations of the solar neutrino flux over time (Abe et al., 2023). Periodicities in the solar neutrino fluxes, if confirmed, could provide evidence for new solar, nuclear, or neutrino physics beyond the commonly accepted physics of vacuum-dominated and matter-enhanced oscillations of massive neutrinos (MSW model) that is, after 50 years of solar neutrino experiment and theory, considered to be the ultimate solution to the solar neutrino problem (Figure 1).

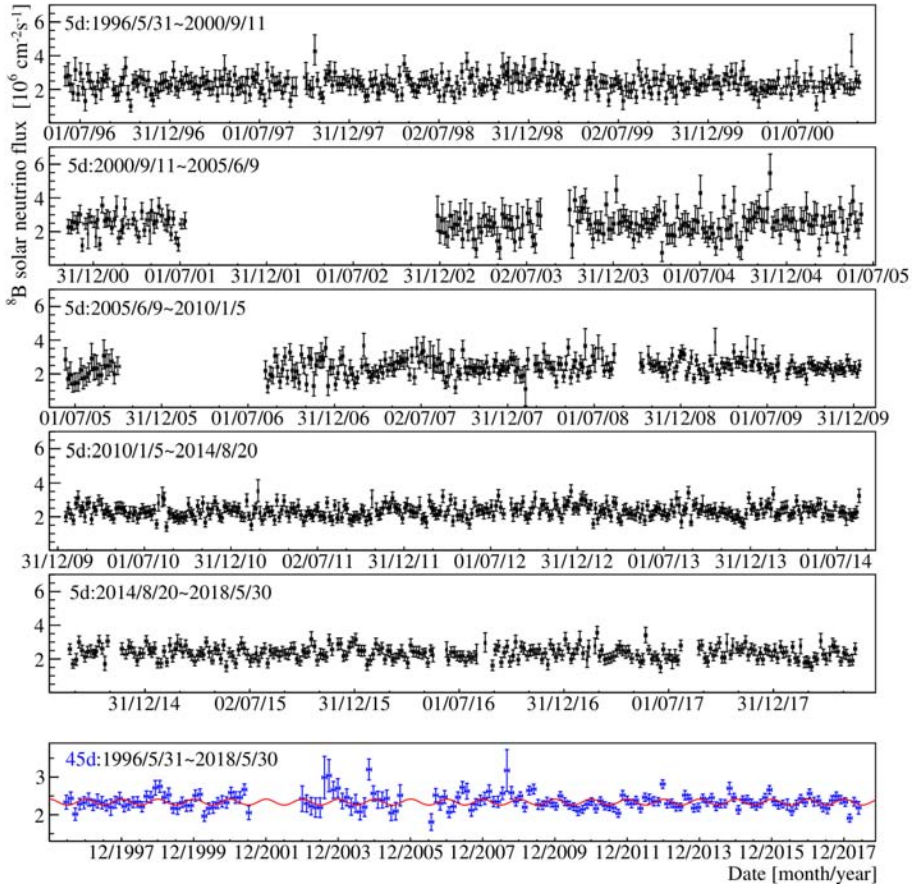

Figure 2: Measured ^8B solar neutrino fuxes for 5-day (top five panels, black data points) and 45-day (bottom panel, blue data points) intervals without $1/R^2$ correction. The errors in the 5-day (the 45-day) plot are asymmetric (symmetric) errors of the average fluxes. The solid-red curve in the 45-day plot is the expected sinusoidal solar neutrino flux based on the elliptical orbit of the Earth Abe et al., 2023.

Specifically, subsequent to the analysis made by the SuperKamiokande collaboration, the SNO experiment collaboration has painstakingly searched for evidence of time variability at periods ranging from 10 *years* down to 10 *minutes*. SNO has found no indications for any time variability of the ^8B flux at any timescale, including in the frequency window in which g-mode oscillations of the solar core might be expected to occur. Despite large efforts to utilize helio-seismology and helio-neutrinospectroscopy, at present time there is no conclusive evidence in terms of physics for time variability of the solar neutrino fluxes from any solar neutrino experiment. If such a variability over time would be discovered, a mechanism for a chronometer for solar variability could be proposed based on relations between properties of thermonuclear fusion and g-modes (Buldgen et al., 2024; Sturrock et al., 2021).

All above findings encouraged the conclusion that Fourier and wavelet analysis, which are based upon the analysis of the variance of the respective time series (standard deviation analysis: SDA) should be complemented by the utilization of diffusion entropy analysis (DEA), which measures the scaling of the probability density function (pdf) of the diffusion process generated by the time series thought of as the physical source of fluctuations (Scafetta, 2010). For this analysis, we have used the publicly available data of SuperKamiokande-I (1996-05-31 - 2001-07-15) and SuperKamiokande-II (2002-12-10 - 2005-10-06) (see Figure 2) (Yoo et al., 2003: Cravens et al., 2008; Abe et al., 2024). Such an analysis does not reveal periodic variations of the solar neutrino fluxes but shows how the pdf scaling exponent departs in the non-Gaussian case from the Hurst exponent. Figures 3 and 4 show the scaling exponents (DEA) for the SuperKamiokande I and II data. The respective Hurst exponents for SDA are visible in Figures 5 and 6 (Haubold and Mathai, 2018, 2025). SuperKamiokande is sensitive mostly to neutrinos from the ^8B and *hep* branch of the *pp* nuclear fusion chain in solar burning. Above approximately 4 MeV the detector can pick-out the scattering of solar neutrinos off atomic electrons which produces Cherenkov radiation in the detector. The ^8B and rarer *hep* neutrinos have a spectrum which ends near 20 MeV.

Assuming that the solar neutrino signal is governed by a probability density function with scaling given by the asymptotic time evolution of a pdf of x, obeying the property (Scafetta, 2010; Culbreth et al, 2023; Beghin et al. 2025)

$$p(x,t) = \frac{1}{t^\delta} f(\frac{x}{t^\delta}), \tag{1}$$

where δ denotes the scaling exponent of the pdf. In the variance based methods, scaling is studied by direct evaluation of the time behavior of the variance of the diffusion process. If the variance scales, one would have

$$\sigma_x^2(t) \sim t^{2H}, \tag{2}$$

where $\sigma_x^2(t)$ is the variance of the diffusion process and where H is the Hurst exponent. To evaluate the Shannon entropy of the diffusion process at time t, defined $S(t)$ as

$$S(t) = -\int_{-\infty}^{+\infty} dx\ p(x,t) \ln\ p(x,t) \tag{3}$$

and with the previous $p(x,t)$ one has

$$S(t) = A + \delta \ln(t), \quad A = -\int_{-\infty}^{+\infty} dy f(y) \ln f(y). \tag{4}$$

The scaling exponent δ is the slope of the entropy against the logarithmic time scale. The slope is visible in Figures 3 and 4 for the SuperKamiokande data measured for ^8B and *hep*. The Hurst exponents (SDA) are $H = 0.66$ and $H = 0.36$ for ^8B and *hep*, respectively, see Figures 5 and 6 (Mathai and Haubold, 2018). The *pdf* scaling

exponents (DEA) are $\delta = 0.88$ and $\delta = 0.80$ for ^8B and *hep*, respectively, as shown in Figures 3 and 4. The values for both SDA and DEA indicate a deviation from Gaussian behavior which would require that $H = \delta = 0.5$.

A test computation for the application of SDA and DEA to data that are known to exhibit non-Gaussian behavior have been published by Haubold et al. (2012) and Tsallis (2024). In this test computation, SDA and DEA, applied to the magnetic field strength fluctuations recorded by the Voyager-I spacecraft in the heliosphere clearly revealed the scaling behavior of such fluctuations as previously already discovered by non-extensive statistical mechanics considerations that lead to the determination of the non-extensivity q-triplet.

2.1 The Principle of Scaling Model

Let x be a real scalar random variable having the density $f(x)$. Then $f(x) > 0$ on the support of x, that is, whenever $f(x) \neq 0$. Let $a > 0$ be a real scalar constant. Suppose that we wish to determine the density of the scaled x, namely ax. Let

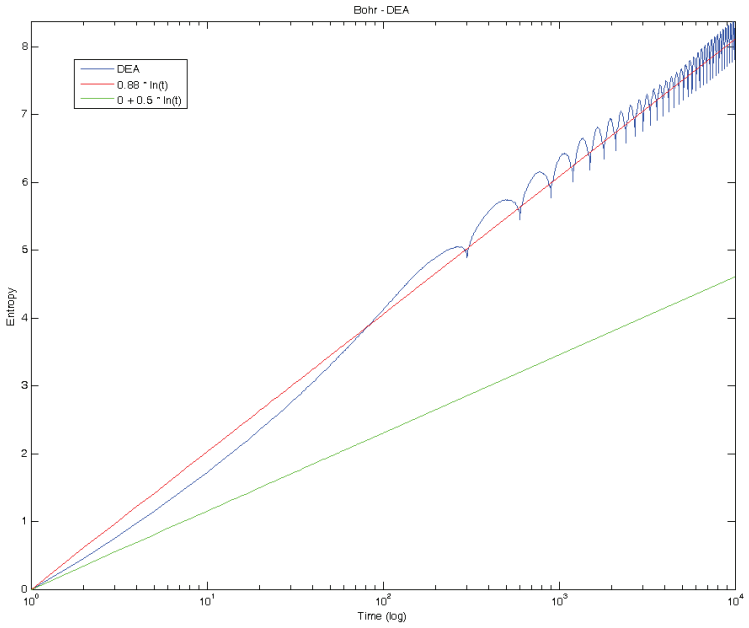

Figure 3: The Difusion Entropy Analysis (DEA) of the ^8B solar neutrino data from the SuperKamiokande I and II experiment.

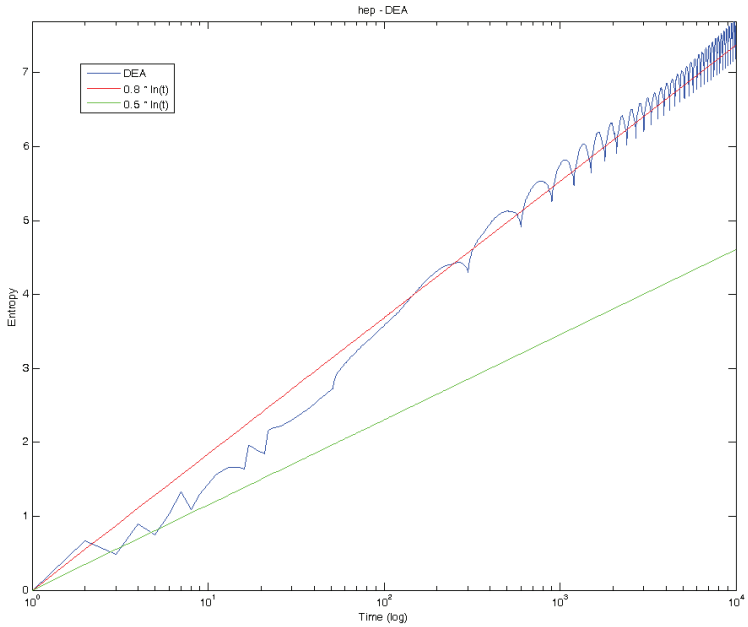

Figure 4: The Difusion Entropy Analysis (DEA) of the *hep* solar neutrino data from the SuperKamiokande I and II experiment.

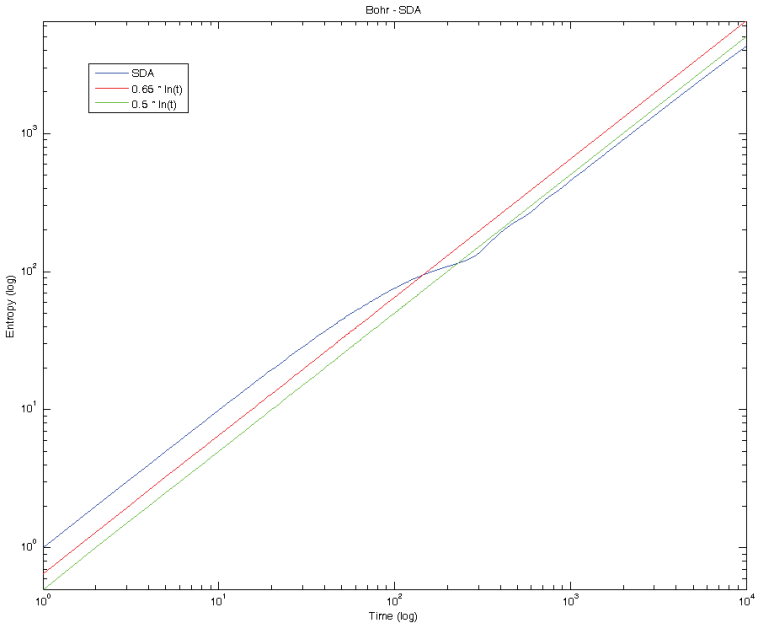

Figure 5: The Standard Deviation Analysis (SDA) of the ^8B solar neutrino data from the SuperKamiokande I and II experiment.

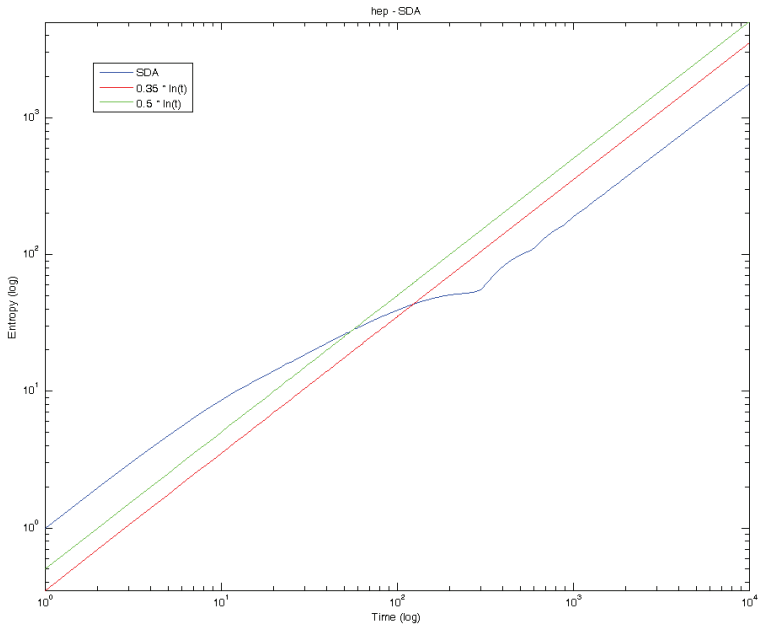

Figure 6: The Standard Deviation Analysis (SDA) of the *hep* solar neutrino data from the SuperKamiokande I and II experiment.

$y = ax, a > 0$ where a is a positive constant. Let $g(y)$ be the density of y. Then

$$g(y)\mathrm{d}y = f(x)\mathrm{d}x = f(\frac{y}{a})\frac{\mathrm{d}y}{a} = \frac{1}{a}f(\frac{y}{a})\mathrm{d}y \Rightarrow$$
$$g(y) = \frac{1}{a}f(\frac{y}{a}). \tag{i}$$

What is the mean value and variance of the scaled x? Let $E[\cdot]$ denote the expected value or mean value of $[\cdot]$ and let $\mathrm{Var}(\cdot)$ = variance of $(\cdot)$. Then,

$$E[y] = E[ax] = aE[x], \mathrm{Var}(y) = \mathrm{Var}(ax) = a^2\mathrm{Var}(x)$$

which means that the mean value is scaled a and the variance is scaled by a^2. Suppose that $a = t^\delta, t > 0, \delta > 0$. Then, the mean value of x is scaled by t^δ and the variance is scaled by $t^{2\delta}$. What happens to Shannon entropy? Shannon entropy for a discrete distribution $P = (p_1, ..., p_k), p_j > 0, j = 1, ..., k, p_1 + ... + p_k = 1$, denoted by $S(P)$, is given by

$$S(P) = -c\sum_{j=1}^{k} p_j \ln p_j \tag{ii}$$

where $c > 0$ is a constant. This negative sign is taken because $0 < p_j < 1 \Rightarrow \ln p_j < 0$ and hence, in order to make $S(P) > 0$ a minus sign is taken. The corresponding continuous case is the following:

$$S(f) = -c\int_x f(x)\ln f(x)\mathrm{d}x, c > 0. \tag{iii}$$

Even though $f(x)$ is the density of x, it need not remain less than one, still a minus sign is taken because the probability over the interval $\mathrm{d}x$ is $f(x)\mathrm{d}x$ which is always less than one, there by $\ln[f(x)\mathrm{d}x] < 0$ and such sums are there in the integral. Hence the notation $S(f)$ corresponds to that in the discrete case $S(P)$. What happened to Shannon entropy in the scaled case? Note that in the scaled case the density $g(y)$ of the scaled x, namely $y = ax$, is given by $g(y) = \frac{1}{a}f(\frac{y}{a})$. Hence

$$\begin{aligned} S(g) &= -c\int_y g(y)\ln g(y)\mathrm{d}y = -c[\int_y \frac{1}{a}f(\frac{y}{a})\ln(\frac{1}{a}f(\frac{y}{a}))\mathrm{d}y] \\ &= -c[\ln(\frac{1}{a})]\int_y f(\frac{y}{a})\frac{\mathrm{d}y}{a} - c\int_y f(\frac{y}{a})\ln f(\frac{y}{a})\frac{\mathrm{d}y}{a} \\ &= [c\ln a]\int_z f(z)\mathrm{d}z - c\int_z f(z)\ln f(z)\mathrm{d}z, z = \frac{y}{a} \\ &= B + S(f), B = c\ln a. \end{aligned}$$

This is the change where $S(f)$ and $S(g)$ are Shannon entropy on f and g respectively. If $a = t^\delta, t > 0, \delta > 0$, then $B = c\delta \ln t$.

If the staring variable is a $p \times 1$ vector or a $p \times q$ matrix X, then the scaling constant can be a real scalar quantity $a > 0$ or a real $p \times p$ positive definite matrix A so that $Y = aX$ or $Y = AX$ will be the scaled model. When matrices are involved, we can have scaling matrices $A^{\frac{1}{2}}$ and $B^{\frac{1}{2}}$ so that we may take $Y = A^{\frac{1}{2}}XB^{\frac{1}{2}}$ where B is another $q \times q$ real positive definite matrix. In the case of matrices or sequence of matrices we can incorporate scaling in many different ways.

In a practical situation, usually the scaling constant $a > 0$ may have its own prior distribution. For example, if $a = t^\delta$ where if t is the time parameter then the behavior of $y = ax = t^\delta x$ may change for different t values or at different epochs of time, which means t has its own distribution.

2.2 Prior Distribution for the Scaling Parameter

Suppose that the scalar variable x be positive and has a gamma density of the form

$$f(x) = \frac{b^\gamma}{\Gamma(\gamma)}x^{\gamma-1}\mathrm{e}^{-bx}, x > 0, b > 0, \gamma > 0$$

and $f(x) = 0$ elsewhere. Consider a scaled x, namely $y = ax, a > 0$. Then, the density of y, $g(y)$, is the following:

$$\begin{aligned} g(y) &= \frac{1}{a}f(\frac{y}{a}) = \frac{1}{a}\frac{b^\gamma}{\Gamma(\gamma)}(\frac{y}{a})^{\gamma-1}\mathrm{e}^{-\frac{by}{a}} \\ &= a^{-\gamma}\frac{b^\gamma}{\Gamma(\gamma)}y^{\gamma-1}\mathrm{e}^{-\frac{b}{a}y}. \end{aligned}$$

Suppose that $-\infty < x < \infty, a > 0$ and suppose that $a = t^{\delta}, t > 0, \delta > 0$, then for $y = t^{\delta}x$ the density of y is the following:

$$g(y) = t^{-\gamma\delta}\frac{b^{\gamma}}{\Gamma(\gamma)}y^{\gamma-1}\mathrm{e}^{-bta^{-\delta}y}.$$

Suppose that $-\infty < x < \infty$ and x has a Gaussian density

$$f(x) = \frac{1}{\sigma\sqrt{2\pi}}\mathrm{e}^{-\frac{1}{2\sigma^2}(x-\mu)^2}.$$

Then, $y = ax$ has the density

$$g(y) = \frac{1}{a}\frac{1}{\sigma\sqrt{2\pi}}\mathrm{e}^{-\frac{1}{2\sigma^2a^2}(y-a\mu)^2}.$$

Suppose that the scaling constant a has a prior density. In this case we may write $g(y)$ as $g(y|a) =$ density of y at a given a. If $h(a)$ is a prior density for a, then the joint density of a and y is $g(y|a)h(a) = \frac{1}{a}f(\frac{y}{a})h(a)$. Then the unconditional density of y or the density of y for all values of a, is given by the following and denoted by $g_y(y)$:

$$g_y(y) = \int_a \frac{1}{a}f(\frac{y}{a})h(a)\mathrm{d}a.$$

Suppose that $h(a)$ is the density

$$h(a) = \frac{1}{\Gamma(\gamma_1)}a^{\gamma_1-1}\mathrm{e}^{-a}, a > 0, \gamma_1 > 0$$

and zero elsewhere. Suppose that $f(x)$ is Gaussian with $\mu = 0$. Then,

$$\begin{aligned} g_y(y) &= \int_a \frac{1}{a}f(\frac{y}{a})h(a)\mathrm{d}a \\ &= \int_{a=0}^{\infty}\frac{1}{a}\frac{1}{\sigma\sqrt{2\pi}}\mathrm{e}^{-\frac{y^2}{2\sigma^2a^2}}\frac{1}{\Gamma(\gamma_1)}a^{\gamma_1-1}\mathrm{d}^{-a}\mathrm{d}a \\ &= \frac{1}{\sigma\sqrt{2\pi}}\frac{1}{\Gamma(\gamma_1)}\int_{a=0}^{\infty}a^{(\gamma_1-1)-1}\mathrm{e}^{-a-\frac{y^2}{2\sigma^2a^2}}\mathrm{d}a. \end{aligned} \tag{iv}$$

This is Bessel type integral which was evaluated earlier. This integral has the structure of the Mellin convolution of a product, namely

This is Bessel type integral which was evaluated earlier. This integral has the structure of the Mellin convolution of a product, namely

$$\int_{v=0}^{\infty}\frac{1}{v}f_1(\frac{u}{v})f_2(v)\mathrm{d}v$$

where

$$f_1(x_1) = \mathrm{e}^{-x_1^2} \Rightarrow f_1(\frac{u}{v}) = \mathrm{e}^{-\frac{u^2}{v^2}}, v = a, u^2 = \frac{y^2}{2\sigma^2}$$
$$f_2(x_2) = x_2^{\gamma_1 - 1}\mathrm{e}^{-x_2}, x_j > 0, j = 1, 2.$$

Then the Mellin transforms of f_1 and f_2, denoted by $M_{f_j}(s), j = 1, 2$, with the Mellin parameter s, are the following:

$$M_{f_2}(s) = \int_0^\infty x_2^{s-1} f_2(x_2)\mathrm{d}x_2 = \Gamma(\gamma_1 - 1 + s), \Re(s) > -\Re(\gamma_1) + 1.$$
$$M_{f_1}(s) = \int_{x_1=0}^\infty x_1^{s-1}\mathrm{e}^{-x_1^2}\mathrm{d}x_1 = \frac{1}{2}\Gamma(\frac{s}{2}), \Re(s) > 0,$$
$$M_{f_1}(s)M_{f_2}(s) = \frac{1}{2}\Gamma(\frac{s}{2})\Gamma(\gamma_1 - 1 + s).$$

Hence, for $u = +\sqrt{\frac{y^2}{2\sigma^2}}$,

$$\begin{aligned} g_y(y) &= \frac{1}{\sigma\sqrt{2\pi}}\frac{1}{\Gamma(\gamma_1)}\frac{1}{2} \\ &\quad \times \frac{1}{2\pi i}\int_{c-i\infty}^{c+i\infty}\Gamma(\frac{s}{2})\Gamma(\gamma_1 - 1 + s)u^{-s}\mathrm{d}s \\ &= \frac{1}{2\sigma\sqrt{2\pi}\Gamma(\gamma_1)}H_{0,2}^{2,0}\left[u|_{(0,\frac{1}{2}),(\gamma_1-1,1)}\right] \end{aligned}$$

This H-function, denoted by H_1, is the following after writing $\frac{s}{2} = s_1$:

$$H_1 = \frac{1}{2\pi i}\int_{c_1-i\infty}^{c_1+i\infty}\Gamma(s_1)\Gamma(\gamma_1 - 1 + 2s_1)(u^2)^{-s_1}\mathrm{d}s_1.$$

By using the duplication formula for gamma functions, $\Gamma(2z) = \pi^{-\frac{1}{2}}2^{2z-1}\Gamma(z)\Gamma(z+\frac{1}{2})$ we can write

$$\Gamma(\gamma_1 - 1 + 2s_1) = \frac{2^{\gamma_1-2}}{\pi^{\frac{1}{2}}}(\frac{1}{4})^{-s_1}\Gamma(s_1 + \frac{\gamma_1 - 1}{2})\Gamma(s_1 + \frac{\gamma_1}{2}).$$

Then

$$H_1 = \frac{2^{\gamma_1-2}}{\pi^{\frac{1}{2}}}G_{0,3}^{3,0}\left[\frac{u^2}{4}|_{0,\frac{\gamma_1-1}{2},\frac{\gamma_1}{2}}\right], \frac{u^2}{4} = \frac{y^2}{8\sigma^2}.$$

When γ_1 is not an odd positive integer, then the poles of the integrand are simple and one can evaluate the above G-function as a linear function of three ${}_0F_2$ hypergeometric functions by using residue calculus as illustrated below for one such series. Consider the poles of $\Gamma(s_1)$. They are at $s_1 = -\nu, \nu = 0, 1, \ldots$. Let the sum of the residues be denoted by S_1. Then

$$S_1 = \sum_{\nu=0}^{\infty} \frac{(-1)^\nu}{\nu!}(\frac{y^2}{2\sigma^2})^\nu \Gamma(-\nu + \frac{\Gamma_1 - 1}{2})\Gamma(-\nu + \frac{\gamma_1}{2}).$$

But for $b \neq \pm 0, 1, 2, ...$

$$\Gamma(b-\nu) = (-1)^\nu \frac{\Gamma(b)}{(-b+1)_\nu}, (d)_\nu = d(d+1)...(d+\nu-1), (d)_0 = 1, d \neq 0.$$

Then,

$$\Gamma(-\nu + \frac{\gamma_1 - 1}{2}) = (-1)^\nu \Gamma(\frac{\gamma_1 - 1}{2}) \frac{1}{(\frac{3}{2} - \frac{\Gamma_1}{2})_\nu}$$

$$\Gamma(-\nu + \frac{\gamma_1}{2}) = (-1)^\nu \Gamma(\frac{\gamma_1}{2}) \frac{1}{(1 - \frac{\gamma_1}{2})_\nu}.$$

Hence,

$$S_1 = \Gamma(\frac{\gamma_1}{2})\Gamma(\frac{\gamma_1 - 1}{2}) {}_0F_2(-; \frac{3}{2} - \frac{\gamma_1}{2}, 1 - \frac{\gamma_1}{2}; -\frac{y^2}{8\sigma^2}).$$

III. PROBABILITY DENSITY FUNCTION AND DIFFERENTIAL EQUATION: LEVY FLIGHTS

We consider a diffusion process generated by a waiting time pdf with a finite characteristic time T that can be modeled with a Poissonian distribution, and a jump length pdf $\lambda(x)$ given by a Lévy distribution with index $0 < \alpha < 2$ (Metzler and Klafter, 2000). The Fourier transform of $\lambda(x)$ is

$$\hat{\lambda}(k) = exp(-\sigma^\alpha |k|^\alpha) \sim 1 - \sigma^\alpha |k|^\alpha. \tag{5}$$

Then $\lambda(x)$ has the asymptotic behavior given by

$$\lambda(x) \sim A_\alpha \sigma^\alpha |x|^{-1-\alpha} = A_\alpha \sigma^{1-\mu} |x|^{-\mu} \tag{6}$$

for $|x| \gg \sigma$ and $\mu = 1 + \alpha$. Substituting the asymptotic expansion of the jump length pdf $\hat{\lambda}(k)$ in the Fourier space and the waiting time pdf of

$$\Phi(t) = \frac{1}{\tau} exp(-\frac{t}{\tau}) \tag{7}$$

where $\tau = T < \infty$ is the characteristic waiting time in the Laplace space into

$$\hat{p}(k,s) = \frac{1 - \hat{\Phi}(s)}{s} \frac{\hat{p_0}(k)}{1 - \hat{\Phi}(s)\hat{\lambda}(k)}, \tag{8}$$

where $\hat{p_0}(k)$ is the Fourier transform of the initial condition $p(x,0)$, we obtain the following jump pdf in the Fourier-Laplace space

$$\hat{p}(k,s) = \frac{1}{s + K^\alpha |k|^\alpha}, \tag{9}$$

where $K^\alpha = \sigma^\alpha/\tau$ is the generalized diffusion constant. Eq.(9) is the solution of the generalized diffusion equation (Hilfer, 2018)

$$\frac{\partial p(x,t)}{\partial t} = K^\alpha \, {}_{-\infty}D_x^\alpha p(x,t), \tag{10}$$

where ${}_{-\infty}D_x^\alpha$ is the fractional Weyl operator. Upon Laplace inversion of Eq. (9), we get the characteristic function of the jump pdf

$$\hat{p}(k,t) = exp(-K^\alpha t|k|^\alpha). \tag{11}$$

Eq.(11) is the characteristic function of a centered and symmetric Lévy distribution. The Fourier inversion of (7) can be analytically obtained by making use of the Fox function (Mathai et al., 2010; Mathai and Haubold, 2018)

$$\begin{aligned} p(x,t) &= \frac{1}{\alpha}\frac{1}{t^{1/\alpha}}\frac{t^{1/\alpha}}{|x|} H_{2,2}^{1,1}\left[\frac{|x|}{Kt^{1/\alpha}}\Big|_{(1,1),(1,\frac{1}{2})}^{(1,\frac{1}{\alpha}),(1,\frac{1}{2})}\right] \\ &= \frac{1}{\alpha|x|}\frac{1}{2\pi i}\int_{c-i\infty}^{c+i\infty} \frac{\Gamma(1+\frac{s}{\alpha})\Gamma(-\frac{s}{2})}{\Gamma(-s)\Gamma(1+\frac{s}{2})}\left(\frac{|x|}{Kt^{1/\alpha}}\right)^{-s} \mathrm{d}s \end{aligned}$$

, where c in the contour is such that $-\alpha < c < 0$. Replacing $\frac{s}{\alpha}$ by s, observing that α coming from s ds is canceled with α sitting outside, we have the following:

$$p(x,t) = \frac{1}{|x|}\frac{1}{2\pi i}\int_{c'-i\infty}^{c'+i\infty} \frac{\Gamma(1+s)\Gamma(-\frac{\alpha}{2}s)}{\Gamma(-\alpha s)\Gamma(1+\frac{\alpha}{2}s)}\left(\frac{|x|}{Kt^{1/\alpha}}\right)^{-\alpha s} \mathrm{d}s, -1 < c' < 0.$$

By using the duplication formula for gamma functions, we have

$$\Gamma(-\alpha s) = \Gamma(2(-\frac{\alpha}{2}s)) = 2^{-\alpha s-1}\pi^{-\frac{1}{2}}\Gamma(-\frac{\alpha}{2}s)\Gamma(\frac{1}{2}-\frac{\alpha}{2}s)$$

so that one $\Gamma(-\frac{\alpha}{2}s)$ is canceled. Then,

$$p(x,t) = \frac{2\pi^{\frac{1}{2}}}{|x|}\frac{1}{2\pi i}\int_{c'-i\infty}^{c'+i\infty} \frac{\Gamma(1+s)}{\Gamma(\frac{1}{2}-\frac{\alpha}{2}s)\Gamma(1+\frac{\alpha}{2}s)}\left(\frac{|x|}{2Kt^{1/\alpha}}\right)^{-\alpha s} \mathrm{d}s.$$

Evaluating the H-function as the sum of the residues at the poles of $\Gamma(1+s)$, which are at $s = -1-\nu, \nu = 0, 1, ...$, we have the following series:

$$\begin{aligned} p(x,t) &= \frac{2\pi^{\frac{1}{2}}}{|x|}\left(\frac{|x|^\alpha}{(2K)^\alpha t}\right) \\ &\times \sum_{\nu=0}^{\infty}\frac{(-1)^\nu}{\nu!}\frac{1}{\Gamma(\frac{1+\alpha}{2}+\frac{\alpha}{2}\nu)\Gamma(1-\frac{\alpha}{2}(1+\nu))}\left(\frac{|x|^\alpha}{(2K)^\alpha t}\right)^\nu, \alpha \neq 1, \alpha \neq 2. \end{aligned}$$

IV. DISCUSSION

The first solar neutrino experiment led by Raymond Davis Jr. showed a deficit of neutrinos relative to the solar model prediction, referred to as the solar neutrino problem since the 1970s. The Kamiokande experiment led by Masatoshi Koshiba successfully observed solar neutrinos, as first reported in 1980s. The solar neutrino problem was solved due to neutrino oscillations by comparing the SuperKamiokande and Sudbury Neutrino Observatory results. While recent decades have offered tremendous advances in solar neutrinos across the fields of solar physics (Buldgen et al., 2024; Yang and Tian, 2024), nuclear physics (Bertulani et al., 2022; Hwang et al., 2023), and neutrino physics (Sturrock et al., 2021; Slad, 2024), many lingering mysteries remain.

This chapter takes advantage of publicly available solar neutrino SuperKamiokande data and analyses them by applying diffusion entropy analysis and standard deviation analysis. The result is a scaling exponent $\delta < 1$ indicating anomalous diffusion of solar neutrinos in terms of Lévy flights. Based on this result the chapter developes the probability density function for neutrino flights and derives the respective differential equation in terms of a fractional Fokker-Planck equation. Accordingly, the closed form analytic representation of the neutrino power density function is given as a Fox H-function that can be used for further numerical exercises for the benefit of solar neutrino physics.

The authors have grateful for the support in the diffusion entropy analysis and standard deviation analysis by Dr. Alexander Haubold while he was doing his research at the Department of Computer Science, Columbia University, New York (USA). The results of diffusion entropy analysis were independently confirmed by the research of Dr. Nicy Sebastian, Department of Statistics, St Thomas College, Thrissur, University of Calicut, Kerala (India).

REFERENCES

1. Abe, K. et al. 2023. Search for periodic time variations of the solar 8B neutrino flux between 1996 and 2018 in SuperKamiokande. https://arxiv.org/pdf/2311.01159.
2. Abe, K. et al. 2024. Solar neutrino measurements using the full data period ofSuperKamiokande-IV. https://doi.org/10.1103/PhysRevD.109.092001.
3. Beghin, L., Cristofaro, L., and da Silva, J.L. 2025. Fox-H densities and completely monotone generalized Wright functions. Journal of Theoretical Probability 38: 18. https://doi.org/10.1007/s10959-024-01391-9.
4. Bertulani, C.A., Hall, F.W., and Santoyo, B.I. 2022. Big Bang nucleosynthesis as a probe of new physics. https://arxiv.org/abs/2210.04071.
5. Buldgen, G., Noels, A., Scuflaire, R., Amarsi, A.M., Grevesse, N., Eggenberger,P.,Colgan, J., Fontes, C.J., Baturin, V.A., Oreshina, A.V., Ayukov, S.V., Hakel, P., and Kil-crease, D.P. In-depth analysis of solar models with high-metallicity abundances and updated opacity tables. https://arxiv.org/abs/2404.10478.
6. Cravens, J.P. et al. 2008. Solar neutrino measurements in SuperKamiokande-II.

7. Culbreth, G., Baxley, J., and Lambert, D. 2023. Detecting temporal scaling with modified diffusion entropy analysis. https://arxiv.org/abs/2311.11453. Haubold, A., Haubold, H.J., and Kumar, D. 2012. Heliosheath: Diffusion entropy analysis and nonextensivity q-triplet. https://arxiv.org/abs/1202.3417v1.
8. Hilfer, R. 2018. Mathematical and physical interpretation of fractional derivatives and integrals. In Handbook of Fractional Calculus with Applications, Volume 1:
9. Basic Theory, Edited by A. Kochubei and Yu. Luchko. Berlin: de Gruyter, pp. 47-85.
10. Hwang, E., Ko, H., Heo, K., Cheoun, M.-K., and Jang, D. 2023. Revisiting the Gamow factor reactions on light nuclei. https://arxiv.org/abs/2302.10102.
11. Mathai, A.M., and Haubold, H.J. 2018. Erd ´elyi-Kober Fractional Calculus: From a Statistical Perspective, Inspired by Solar Neutrino Physics. Singapore: Springer.
12. Mathai, A.M., Saxena, R.K., and Haubold, H.J. 2010. The H-Function: Theory and Applications. New York: Springer.
13. Mathai, A.M., and Haubold, H.J. 2025. Modified models for neutrino masses and mixings. Journal of Mathematical Physics 66, 083506. doi: 10.1063/5.0266171.
14. Metzler, R., and Klafter, J. 2000. The Random Walk's Guide to Anomalous Diffu-sion: A Fractional Dynamics Approach. Physics Reports 339: 1-77.
15. Orebi Gann, G.D., Zuber, K., Bemmerer, D., and Serenelli, A. 2021. The Future of Solar Neutrinos. Annual Review of Nuclear and Particle Science 71: 491-528.
16. Sakurai, K. 2018. Solar Neutrino Problems - How They Were Solved. Tokyo: TER- RAPUB.
17. Scafetta, N. 2010. Fractal and Diffusion Entropy Analysis of Time Series: Theory, concepts, applications and computer codes for studying fractal noises and L ´evy walk signals. Saarbruecken: VDM Verlag Dr. Mueller.

Digital Transformation and Competitiveness in the Metallurgical Industry of Rafaela: A Self-Diagnostic Approach

Fornari Javier, Karchesky Darío, Gentinetta Romina, Liberatori Héctor, Zenobi Román, Boglione Sebastián & Pittácolo Juan Manuel

Universidad Católica de Santiago del Estero

ABSTRACT

The metallurgical industry in Rafaela faces significant challenges related to competitiveness and the integration of digital technologies into its production processes. This study addresses the problem of how small and medium-sized enterprises (SMEs) in the sector can improve their efficiency and adapt to a globalised market environment through digital transformation. To address this problem, an exploratory-descriptive self-diagnosis methodology was applied, using structured questionnaires to assess the levels of knowledge, integration, systematisation, and innovation in key areas such as design, procurement, manufacturing, administration, and sales. The results reveal an uneven adoption of digital technologies within these companies, with a notable reliance on manual systems in critical areas and low information integration between departments. The proposed solution is based on implementing a digital transformation framework that enables companies to improve their processes and foster a culture of technological advancement and continuous training. In conclusion, comprehensive digital transformation emerges as a necessary step for Rafaela's metallurgical SMEs to enhance their competitiveness, efficiency, and adaptability in a dynamic market context.

Keywords: digital transformation, metallurgical industry, competitiveness, SMEs, technological innovation.

Classification: LCC Code: HD45, TS155, HD2346

Language: English

Great Britain Journals Press

LJP Copyright ID: 925605
Print ISSN: 2631-8490
Online ISSN: 2631-8504

London Journal of Research in Science: Natural & Formal

Volume 26 | Issue 1 | Compilation 1.0

Digital Transformation and Competitiveness in the Metallurgical Industry of Rafaela: A Self-Diagnostic Approach

Fornari Javier[α], Karchesky Darío[σ], Gentinetta Romina[ρ], Liberatori Héctor[Ↄ], Zenobi Román[¥], Boglione Sebastián[χ] & Pittácolo Juan Manuel[v]

ABSTRACT

The metallurgical industry in Rafaela faces significant challenges related to competitiveness and the integration of digital technologies into its production processes. This study addresses the problem of how small and medium-sized enterprises (SMEs) in the sector can improve their efficiency and adapt to a globalised market environment through digital transformation. To address this problem, an exploratory-descriptive self-diagnosis methodology was applied, using structured questionnaires to assess the levels of knowledge, integration, systematisation, and innovation in key areas such as design, procurement, manufacturing, administration, and sales. The results reveal an uneven adoption of digital technologies within these companies, with a notable reliance on manual systems in critical areas and low information integration between departments. The proposed solution is based on implementing a digital transformation framework that enables companies to improve their processes and foster a culture of technological advancement and continuous training. In conclusion, comprehensive digital transformation emerges as a necessary step for Rafaela's metallurgical SMEs to enhance their competitiveness, efficiency, and adaptability in a dynamic market context. The adoption of advanced technologies and improved organisational integration are key factors for the success of this process and for ensuring sustainable long-term growth.

Keywords: digital transformation, metallurgical industry, competitiveness, SMEs, technological innovation.

Author α σρ Ↄ ¥ χ v: Universidad Católica de Santiago del Estero.

I. INTRODUCTION

The economy of the city of Rafaela is characterised by robust industrial production and significant agricultural activity, which have driven the growth of manufacturing in various ways. Currently, Rafaela is a regional centre for industrial development and the main dairy hub of Argentina and South America. The industrialisation process in the city has been dynamic, favoured by the establishment of industries dedicated to processing raw materials from the region. In general terms, industrial development in Rafaela has followed a pattern similar to that experienced by the Argentine economy as a whole. Additionally, the city's industrial structure, composed of diverse sectors, has allowed it to maintain some stability in the face of various economic and social crises in the country. Despite this diversification, the food and beverage sectors, along with the manufacture of auto parts, machinery, and equipment, account for 69% of total employment in the region.

London Journal of Research in Science: Natural & Formal

II. METHODOLOGY

To establish the characterisation of the level of digitalisation of a group of industries in Rafaela, a series of exploratory-descriptive questionnaires were developed, as the topic has not been addressed with this methodology in this region, and existing precedents generally have a different focus. Initially, information will be obtained from the companies, including their mission, vision, and values, corporate strategy, economic data, corporate reputation actions, history of risks and opportunities, strategic publics, along with the definition and characteristics and value in the company, competition, market share, etc. The analysis of the information will allow the extraction of variables of industrial behaviour online and the behaviour of strategic publics online, ultimately variables that affect the digital transformation of the company.

III. RESULTS AND DISCUSSIONS

The results of the self-diagnosis reveal that, although there is a good level of knowledge in some functions, integration and systematisation still require significant improvements. The adoption of digital technologies is key to improving efficiency and competitiveness in a globalised market.

IV. CONCLUSION

The functional analysis based on self-diagnosis provides a valuable tool for companies seeking to identify areas for improvement in their organisational structure. The results indicate that, while there is a good level of knowledge in some functions, integration and systematisation still require significant effort to reach a level of excellence. The adoption of digital technologies is key to improving efficiency and competitiveness in a globalised market.

ACKNOWLEDGEMENTS

This article was developed under the research project "Characterisation of the Level of Digitalisation of Industries in Rafaela through the Study and Analysis of their Business Processes using Ontologies and BPMN" and funded by the Universidad Católica de Santiago del Estero.

REFERENCES

1. ALBURQUERQUE, F. Cluster, Territory and Business Development: Different Models of Productive Organisation. BID/FOMIN. Available at: http://www.iadb.org/mif/v2/ fourthwork shoppipCR.htm. Accessed: May 2015.
2. ASCÚA, Rubén. Rafaela 125 Years Confounding Adam Smith. Evolution of its Industry and Commerce. Commission of Industries of the Commercial and Industrial Centre of Rafaela, 2007.
3. BONDAR, Y.; BORYSOV, V.; HRYTSENKO, O. Innovative Management of Knowledge in the Context of the Development of the Information Society. INNOVA Research Journal, v. 2, n. 4, p. 30-37, 2017.
4. BRIANO, C. A. The Digital Transformation of Business: Conceptual Notes (Volume 1). Buenos Aires: Cesar Ariel Briano, 2024.
5. Industrial Census Rafaela. Industrial Census Rafaela 2006. Available at: http://www.rafaela.gov.ar/nuevo/Files/Archivos/arc_93.pdf. Accessed: Feb. 2015.
6. Industrial Census Rafaela. Industrial Census Rafaela 2012. Available at: https://www.rafaela.gov.ar/File.aspx?n=jQ7YxAsBkg2jTYtov**dNqVO6XE22AMhj6WVQQRUmndRloTvVbk6Mm403PjquvQf9&t=Informe_Final__Censo_Industrial_de_Rafaela_2012. Accessed: Mar. 2015.
7. DAVENPORT, T. H.; PRUSAK, L. Working Knowledge: How Organisations Manage What They Know. Boston: Harvard Business Press, 1998.

8. GALBRAITH, J. R. Designing Complex Organisations. Reading: Addison-Wesley, 1973.
9. GOERZIG, D.; BAUERNHANSL, T. Enterprise Architectures for the Digital Transformation in Small and Medium-Sized Enterprises. Procedia CIRP, v. 67, p. 540-545, 2018. Available at: https://doi.org/10.1016/j.procir.2017.12.257.
10. HININGS, B.; GEGENHUBER, T.; GREENWOOD, R. Digital Innovation and Transformation: An Institutional Perspective. Information and Organisation, v. 28, n. 1, p. 52-61, 2018. Available at: https://doi.org/10.1016/j.infoandorg.2018.01.002.
11. MINTZBERG, H. The Structuring of Organisations: A Synthesis of the Research. Prentice-Hall, 1979.
12. MÜLLER, H.; HOPF, M. Competence Centre for the Digital Transformation in Small and Medium-Sized Enterprises. In: HORN, G. (Ed.). Cyber-Physical Systems in Maintenance: Challenges and Opportunities. Elsevier, 2017. p. 1-10.
13. NONAKA, I.; TAKEUCHI, H. The Knowledge-Creating Company: How Japanese Companies Create the Dynamics of Innovation. Madrid: McGraw-Hill, 1995.
14. ORGANISATION FOR ECONOMIC COOPERATION AND DEVELOPMENT (OECD). Proposed Guidelines for Collecting and Interpreting Technological Innovation Data. 2nd ed. Paris: OECD, 1997.
15. PORTER, M. E. Competitive Advantage: Creating and Sustaining Superior Performance. New York: Free Press, 1985.
16. PORTER, M. Clusters and Competitiveness. In: ELGUE, M.C. (Ed.). Globalisation, Local Development and Associative Networks. Buenos Aires: Corregidor, 1999.
17. ZACHMAN, J. A. A Framework for Information Systems Architecture. IBM Systems Journal, v. 26, n. 3, p. 276-292, 1987.